Properties of advanced (reduced) graphene oxide-alginate biopolymer films

Vilcinskas, Karolis

DOI
10.4233/uuid:f317d84b-3a30-4991-a6c1-861b06c781cc

Publication date
2016

Document Version
Final published version

Citation (APA)
Vilcinskas, K. (2016). *Properties of advanced (reduced) graphene oxide-alginate biopolymer films*. [Dissertation (TU Delft), Delft University of Technology]. https://doi.org/10.4233/uuid:f317d84b-3a30-4991-a6c1-861b06c781cc

PROPERTIES OF ADVANCED (REDUCED) GRAPHENE OXIDE-ALGINATE BIOPOLYMER FILMS

Proefschrift

ter verkrijging van de graad van doctor
aan de Technische Universiteit Delft,
op gezag van de Rector Magnificus prof.ir. K.C.A.M. Luyben,
voorzitter van het College voor Promoties,
in het openbaar te verdedigen op
dinsdag 25 oktober 2016 om 10:00 uur

door

Karolis VILCINSKAS
Master of Science in Chemical Engineering,
Kaunas University of Technology
Geboren te Kaunas, Litouwen

This dissertation has been approved by the

promotors: Prof.dr. S. J. Picken and Prof.dr. F. M. Mulder

copromotor: Dr.ing. G. J. M. Koper

Composition of the doctoral committee:

Rector Magnificus	chairman
Prof.dr. S. J. Picken	Delft University of Technology (promotor)
Prof.dr. F. M. Mulder	Delft University of Technology (promotor)
Dr.ing. G. J. M. Koper	Delft University of Technology (copromotor)

Independent members:

Prof.dr.ir. D. C. Nijmeijer	Eindhoven University of Technology
Prof.dr.ir. S. A. F. Bon	The University of Warwick
Prof.dr. J. N. Coleman	Trinity College Dublin
Prof.dr. J. J. Smit	Delft University of Technology
Prof.dr. E. J. R. Sudhölter	Delft University of Technology (reserve list)

The work described in this thesis was carried out in the Advanced Soft Matter (ASM) group at Delft University of Technology, the Faculty of Applied Sciences, the Department of Chemical Engineering. This thesis is part of NanoNextNL, a micro and nanotechnology innovation consortium of the Government of the Netherlands and 130 partners from academia and industry. More information on www.nanonextnl.nl.

ISBN 978-94-6295-491-5
Cover design: Karolis Vilcinskas/Ruben Stoel
Printed by Uitgeverij BOXPress, Vianen

TABLE OF CONTENTS

CHAPTER 1

INTRODUCTION

1.1. Introduction to polymer composites

Polymer composites are multicomponent systems that consist of a polymeric matrix and one or more non-polymeric materials embedded in it. Such combination of two or more phases of different identities and properties yields products of enhanced properties that neither of the components can provide individually [1]. As a result, composite materials possess improved properties such as increased stiffness, improved toughness, wear-resistance, reduced gas permeability, modified electrically conductivity [2].

The use of man-made polymer composites dates back to as early as 5 000 BC when people had used pitch as a binder for reeds in boat-building, however the mass production of polymer composites did not take up until the beginning of the 20th century [3]. Since then, polymer composites have been applied in variety of industries [3-4], as shown in Figure 1.1-1.2. The use of composite materials has had a great impact on society. For example, exploitation of vibration and noise insulating composite materials in construction industry has improved our comfort, whereas implementation of lightweight composite materials in aircraft and automotive industries has enabled to reduce fuel consumption and cost of production [4b].

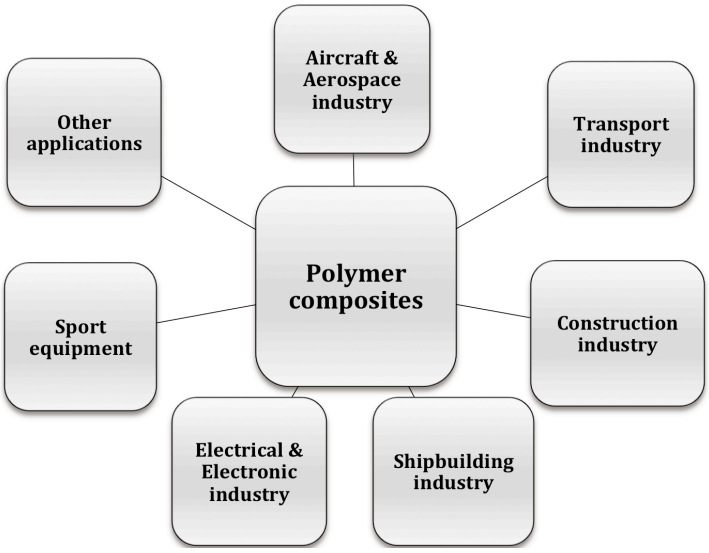

FIGURE 1.1. Uses of polymer composites

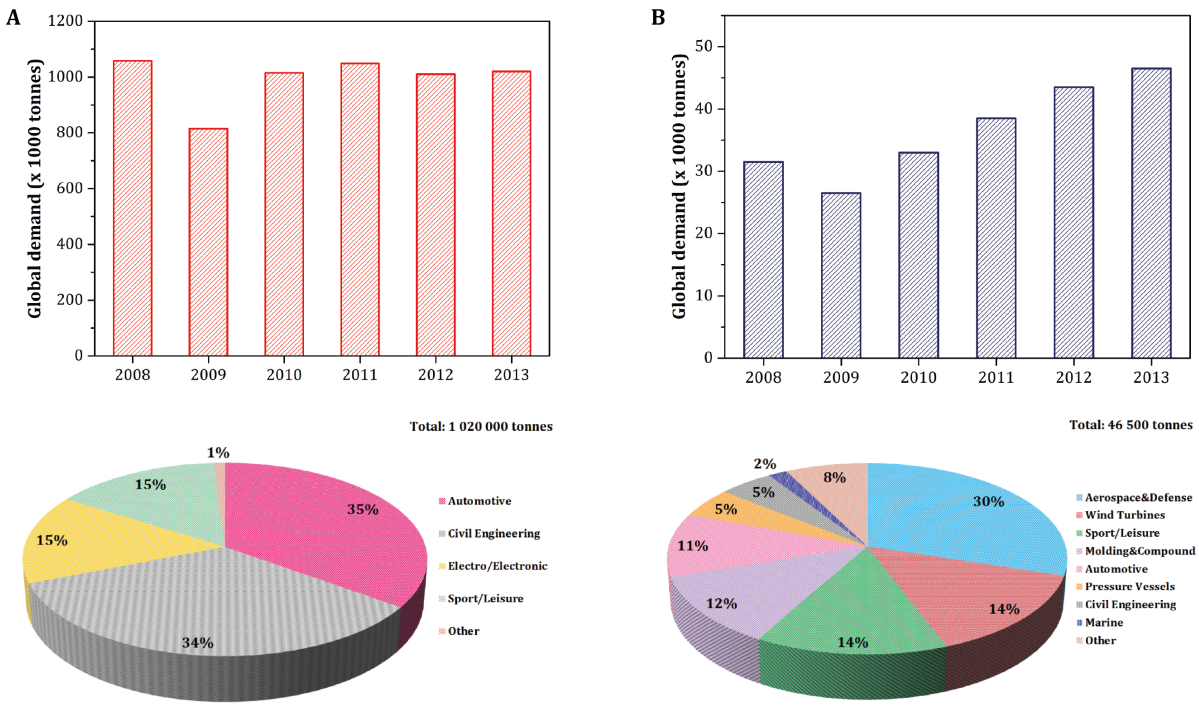

FIGURE 1.2. Comparison of global demand in 2008-2013, and application industries in 2013 for glass fiber-reinforced composites (A) and carbon fiber-reinforced composites (B). Note different ordinate scales of columnar graphs. Adapted from [5].

There are several different classifications of polymer composite materials, two of which are based on the type of used polymer matrix or the type of filler dispersed in the polymer matrix [4b, 6]. In the former classification, depending on the flow properties when heated, polymers can be classified into two categories: *thermoplastics* and *thermosets* [7]. This class consists of linear/branched macromolecules that are not chemically linked, and when heated, macromolecules of such polymers have translational freedom, and therefore can flow. In addition, thermoplastics can undergo repeated cycles of heating-cooling without chemical changes. Thermosets, on the other hand, are comprised of molecules possessing reactive groups that, usually when heated, undergo a chemical reaction resulting in the formation of cross-links that prevent molecules from flowing upon subsequent heating-cooling cycles. Examples of thermoplastic polymers used today include polyethylene, polypropylene, polyvinyl chloride, polystyrene and polyethylene terephthalate [8]. As for thermoset polymers, urethane, urea, phenolic, unsaturated polyester and epoxy are often used

at present [8]. Altogether, both classes of polymers are extensively used for preparation of polymer composites, albeit thermoset composites constitute about 60 % of the total polymer composites market [9].

Alternatively, polymer composites can also be classified according to the nature of filler [3-4, 6], as presented in Table 1.1

TABLE 1.1. Classification, examples and properties of the most abundantly used polymer composites

Class	***Examples of fillers***	***Characteristics of fillers***	***Primary function***
Particulate – reinforced composites	Silica	High hardness	Reinforcement, improvement of dimensional stability of polymer composites
	Calcium carbonate	Cheap, non-toxic, colorant	Increase impact resistance, aging resistance, color of polymer composites
	Mica	Plate-shaped microparticle	Increase stiffness, dimensional stability, improve dielectric, barrier properties of polymer composites
	Glass spheres		Improvement of dimensional stability, abrasion resistance, strength, creep resistance of polymer composites
	Wood flour		Improves surface gloss of polymer composites
	Carbon black	Electrically conductive, colorant	Abrasion resistance, improvement of electrical conductivity, reinforcement, color of polymer composites
Fiber – reinforced composites	Glass fibers	High tensile strength; High chemical resistance; Excellent insulating properties	Improvement of tensile strength, stiffness, insulating, weathering properties of polymer composites
	Carbon fibers	Very high tensile modulus and strength; High electrical conductivity	Improvement of tensile strength, stiffness, electrical conductivity of polymer composites
	Ceramic fibers	High temperature resistance	Improvement of thermal resistance properties of polymer composites

As illustrated in Table 1.1, fiber-polymer composites are primarily designed to yield products of improved mechanical properties such as strength, modulus, fatigue, creep resistance. The reinforcement (the increase in modulus) effect, however, is hugely influenced by the length of fibers, their length to diameter ratio (aspect ratio), degree of orientation inside the polymer matrix and good adhesion to polymer chains. For instance, continuous and aligned fibers that have high affinity to the polymer phase provide a significant reinforcing effect parallel to their direction of orientation [10]. It is worth mentioning that there is an increasing interest in the use of naturally occurring fibers – cellulose, for instance – as well as their polymer composites that, as some suggest, could replace some of high performance fibers [11]. As for the particulate-polymer composites, in addition to enhanced mechanical properties, the composites may also possess improved gas barrier properties, improved dimensional stability, aesthetics and similar properties [12]. Among other particulate filler characteristics (hardness, for instance), for this class of the polymer composite materials, it is essential to consider the shape and size (distribution) of particulate fillers as they strongly influence preparation and properties of polymer composites. In particular, due to much higher specific surface area, nanoscale fillers (size range of 1-100 nm [13]; see Figure 1.3 for classification of nano-sized fillers) can significantly improve polymer composite properties, such as thermal resistance, gas barrier, mechanical properties, at relatively low weight fraction (up to a few weight percent) compared to conventional fillers. Some of these aspects will be further discussed in the following paragraph. Whatever the classification, polymer composites can be considered as comprised of a ductile polymer phase (continuous phase) with a dispersed fibrous and/or particulate phase (discontinuous phase) in it.

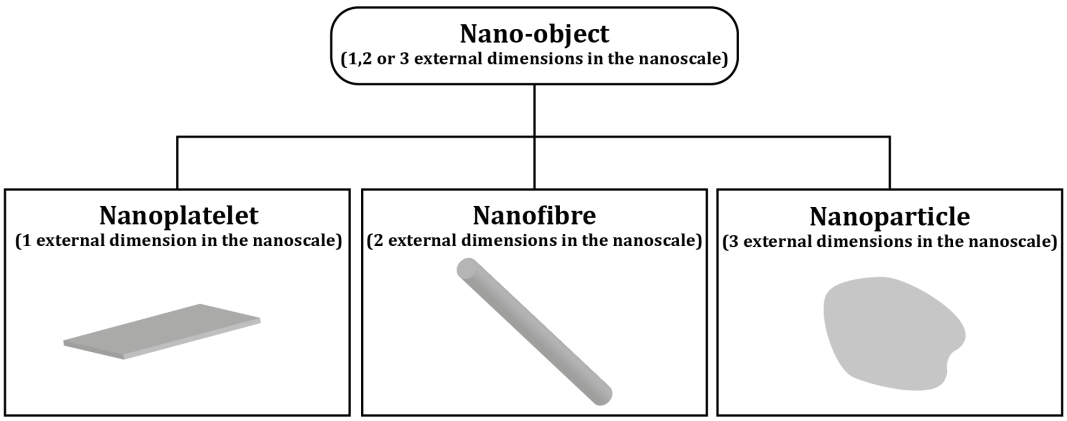

FIGURE 1.3. Classification of nano-objects and schematic illustration of three basic shapes, as defined by ISO/80004-2:2015 [14].

As suggested by Moczo and Pukanszky [15], in order to achieve desirable properties of polymer composites, it is crucial to consider the properties of the components, the composition, the structure, and interfacial interactions that occur between the constituents.

1.2. Important factors influencing the properties of particulate-polymer composites

1.2.1. Properties of the components

The physical properties, such as stiffness, both of the polymer matrix and filler, size and shape of filler particles strongly influence the properties (especially mechanical) of polymer composites. Since the stiffness of filler is usually several orders of magnitude higher than that of the polymer matrix, inclusion of such filler provides improved load-bearing capacity of the composite. However, in order to maximize stiffness of polymer composites, a large contact area between the polymer matrix and filler has to be ensured for the effective stress transfer from the polymer phase to the discontinuous phase. Accordingly, smaller filler particles provide increased specific surface area, however this increases filler surface energy, that prompts agglomeration of filler particles, and, hence, inferior stress distribution [16] and, for instance, worse gas barrier properties [17]. In addition to filler particle size, the shape of filler particles has proven to be important as well, since anisotropically shaped

particles, such as platelets, offer higher specific area, therefore improving mechanical properties as well as other properties even at low weight fractions of the filler [2a, 2b, 18].

1.2.2. Composition

Composition, namely the ratio of the filler mass to the total mass of the composite material, has a big impact on properties of polymer composites. In general, upon increasing weight fraction of the filler, the property of interest, such as stiffness [19], electrical conductivity [20], gas barrier properties [21], improves. However, adverse effects on composite properties of interest are sometimes observed [22] due the onset of aggregation of the filler at higher weight fractions and/or poor adhesion to the continuous phase. Therefore, it is important to determine the optimal filler weight fraction in the polymer matrix to produce polymer composites with the desired improved properties.

1.2.3. Structure

The structural phenomena such as homogeneity, aggregation and orientation of filler particles greatly affect the properties of polymer composites.

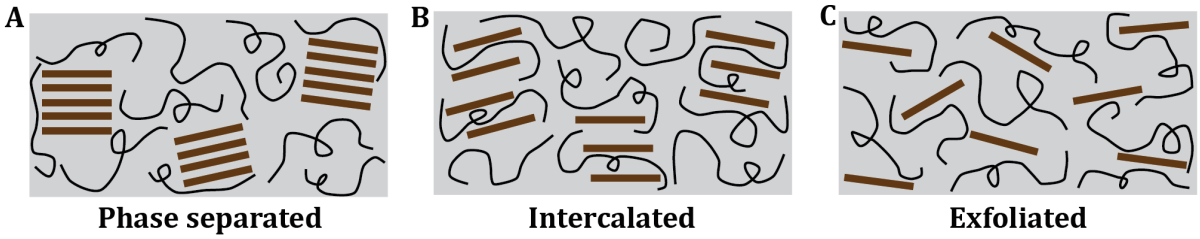

FIGURE 1.4. Structures of polymer nanocomposites: (A) phase separated (micro)composites; (B) intercalated (nano)composites, (C) exfoliated (nano)composites.

Based on experimental evidence of platelet nanocomposites and their preparation method, Alexander and Dubois have proposed the following classification of polymer nanocomposites: phase separated, intercalated and exfoliated [23] (see Figure 1.4). When, due to low affinity to the dispersed phase and/or strong interaction between platelets, polymer chains are not able to intercalate in between the layered structure of dispersed platelets, phase-separated composites of mediocre

properties are obtained. On the other hand, partial (intercalated) or extensive (exfoliated) infiltration of polymer chains into the spacing between filler platelets yields composites with optimum properties. In particular, the exfoliated structure in platelet nanocomposites, where interactions between filler particles are minimized due to the significantly increased separation between them, is desired since it results in dramatic improvements in composite properties at low weight fractions of filler [24]. However, as has been pointed out by Ganesan V. [25], there is still lack of detailed structural information and a clear understanding of the structural evolution of filler particles in the preparation of polymer composites. Such lack of knowledge more often than not yields composites with properties that are difficult to predict using the standard models for estimating the reinforcement effect [26] and/or gas barrier properties [27]. In our analysis on reports on nanocomposites that were prepared by layer-by-layer deposition, we observed unpredictable effects of the number of layers, and thus of the film thickness, on the barrier properties [17]. On close examination of transmission electron micrographs of a variety of nanocomposite systems, we found that the filler distribution was largely inhomogeneous accompanied by significant clustering of filler particles leading to difficult-to-predict gas barrier properties using any of the available models. In addition to inhomogeneity, aggregation of filler particles, as discussed earlier, is also disadvantageous. There has been put a considerable effort into understanding the cohesive forces between particles and the potential use of forces to prevent agglomeration [15] by implementing principles widely employed in colloid science [28]. Knowledge of the interplay between the viscous forces, capillary forces and particle wetting by a polymer (usually in the melt state), or effective use of shear forces, are prime examples of the strategies being pursued. Lastly, orientation (random, perfectly aligned or intermediate) of the filler inside the polymer matrix greatly affects the properties, most notably the mechanical and gas barrier properties of polymer composites. It has been demonstrated both experimentally and theoretically, that the highest reinforcement is achieved along the axial direction of oriented particulate fillers [29]. In addition to the reinforcement effect, the in-plane aligned fillers can dramatically reduce gas permeation along the layer normal of

the composites samples [2d, 30]. As has been noted earlier, in order to be able to estimate polymer composite properties of interest, it is crucial to possess extensive knowledge of structural aspects and ability to control them.

1.2.4. Interfacial aspects

The interphase between polymer and filler is vital in determining polymer composite properties. It is viewed as the finite size transition area between the polymer matrix and dispersed phase, which are of different properties [3, 31]. The thickness of the interphase shows strong composition dependence, and often becomes an issue of debate, nevertheless values ranging from a few angstroms to several microns have been frequently reported [32]. Although different phases exhibit dissimilar properties, there are a variety of interactions between them, of which the most important ones are listed in Table 1.2.

TABLE 1.2. Intermolecular interactions, adapted from [33].

Interaction	*Strength (kJ mol^{-1})*	*Effective range (Å)*
Ionic	600-1 200	2-4
Covalent	60-800	1-3
Van der Waals	20-40	2-8
Hydrogen bonding	4-20	2-4

The presence of the intermolecular interactions at the interphase results in the adhesion force, which plays a crucial role. For instance, the stress transfer in polymer composite materials occurs at the interphase where the acting force on the polymer phase is transmitted to the reinforcing material. Thus, in order to ensure the optimal stress distribution, the interphase has to provide smooth transfer of the acting force from the polymer phase to that of the filler. The importance of understanding the adhesion forces has been manifested by the number of proposed models, mainly based on wettability and free surface energy considerations [34]. In the simplest approach, the

intimate contact between to molecularly rough surfaces may result in a good adhesive contact provided that the polymer phase is able to wet the filler phase sufficiently and there is no air trapped in between the two phases. More complex theories regard electrostatic interactions originating from separating two surfaces, inter-diffusion of molecules between different phases as well as other factors [3]. In an effort to promote adhesion between two phases, modification of filler surface is usually carried out. This can be achieved by using surfactants, coupling agents, functionalization of the filler surface with a polymer layer capable of inter-diffusing in the polymer matrix, or addition of hard particles that initiate formation of 'soft' spots in the polymer matrix able to encase the filler [15]. In effect, favorable interactions between dissimilar phases are of primary importance, especially in optimizing the stress distribution under load, and therefore it is critical to understand the interfacial interactions in order to be able to predict the properties of interest of polymer composites.

In summary, embedment of filler with superior properties inside a polymer matrix does not always yield polymer composites with improved properties. Due to the subtle interplay and multiple interactions between the continuous and dispersed phases, it is often very difficult to control and, therefore, accurately predict the properties of polymer composites.

1.3. Graphene-polymer composites

1.3.1. Preparation of graphene and its derivatives

Since isolation of graphene using Scotch tape in 2004 [35], there has been a considerable effort put into improving its method of production, and exploring its properties and applications, including graphene-polymer composites [36]. Graphene is a flat monolayer of Carbon atoms that are tightly packed in a two-dimensional (single-atom thick) honeycomb lattice [37].

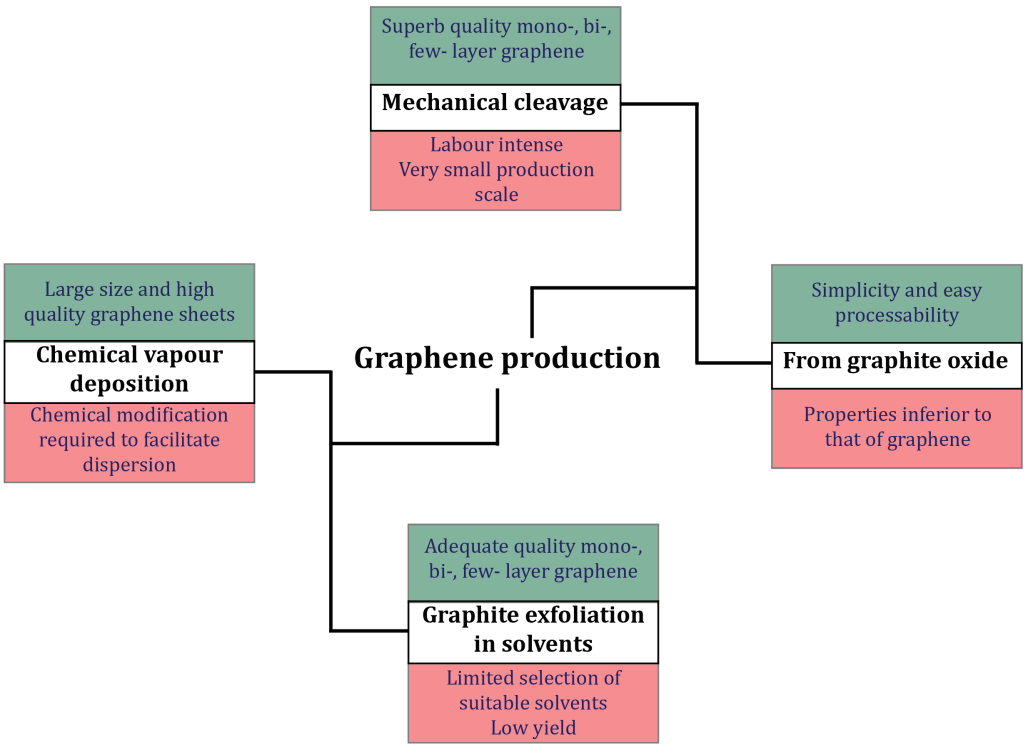

FIGURE 1.5. Summary of the key production methods of graphene.

Figure 1.5 lists the most widely used methods to produce graphene. In the simplest one, mono-, bi-layer, and defect-free graphene sheets can be obtained by unpeeling commercially available highly oriented pyrolytic graphite using Scotch tape [36]. However, this method is laborious and limited to low production yield, and is thus not feasible for the preparation of polymer-graphene composites. Alternatively, graphene production by chemical vapor deposition on metal substrates yields large size, high quality, few-layer graphene sheets. However, in order to obtain isolated graphene sheets, etching of the metal substrate by mineral acids is required. In this method graphene is obtained by thermally assisted catalytic decomposition of a carbon source gas, methane, for instance, whereupon Carbon dissolves in a transition metal substrate (such as copper or nickel) and precipitates forming graphene sheets when rapidly cooled [38]. However, both of the discussed methods are not well-suited for the preparation of polymer graphene composites. When dispersed in a polymer phase, graphene sheets more often than not tend to aggregate, thus in order to

facilitate their homogenous dispersion and increase the affinity between the filler and polymer phases, chemical functionalization of graphene sheets is often carried out [39].

Liquid exfoliation of graphite in solvents [40a] by ultrasound allows obtaining adequate quality, few-layer graphene sheets, however prolonged ultrasonication inevitably reduces the size of graphene sheets [40b], and this can have an adverse effect upon the properties of polymer-graphene composites. In addition, the method is limited by the availability of suitable solvents and low final graphene concentration, nonetheless it enables easier preparation of graphene-based polymer composites. On the other hand, addition of surfactant or polymer, allows obtaining more concentrated graphene dispersions [41]. Although, graphene prepared via this method facilitates preparation of polymer composites, the relatively low concentrations of graphene, the compromised size of graphene sheets, the limited number of suitable solvents, and the presence of surfactants limit the application to only a few polymer systems, often yielding polymer composites with mediocre properties.

Alternatively, much large amounts of graphene-like-material can be obtained by chemical oxidation of graphite [42] following its reduction [43]. However, harsh reaction conditions and introduction of oxygenated groups to graphene sheets induce the formation of lattice defects [44] and eliminate some properties, such as the excellent electrical conductivity. Furthermore, it is difficult to achieve full reduction of the oxygenated groups [45], therefore the properties of graphene derived via this method is inferior to that prepared by mechanical cleavage and chemical vapor deposition. On the other hand, the abundance of oxygenated groups on graphene sheets facilitates dispersion in a variety of solvents, including water, offers reaction sites for chemical modification, and reduces the propensity to aggregate, thus making it very attractive for the preparation of polymer-graphene composites [39].

1.3.2. Preparation of graphene-polymer composites

Due to its remarkable properties, such as immense intrinsic stiffness (see Table 1.3), graphene has been increasingly used in preparation of graphene-polymer composites (Figure 1.6). Solution

blending, melting mixing, *in situ* polymerization [37b, 46] and layer-by-layer deposition are the most often used methods in preparation of graphene-polymer composites.

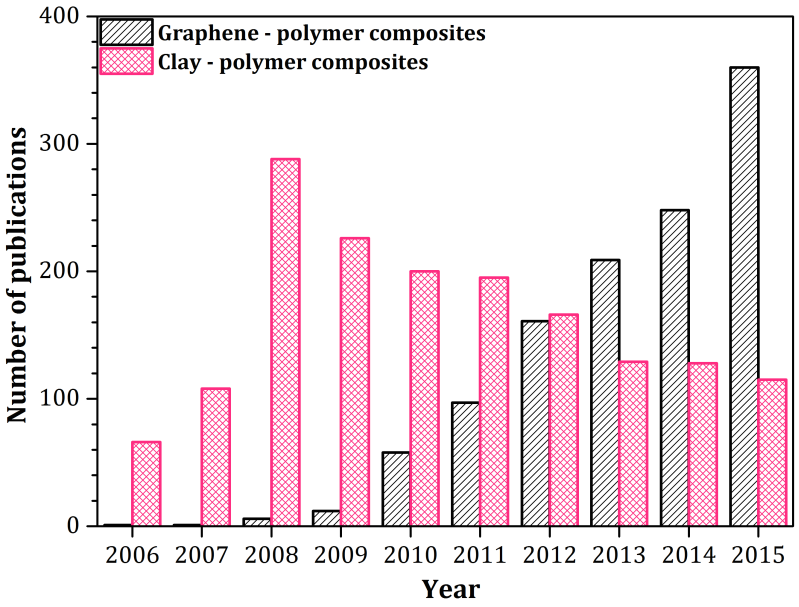

FIGURE 1.6. Evolution of publications using the characteristic keywords (see the legend) in the past 10 years. Retrieved from Scopus.

TABLE 1.3. Physical properties of some filler materials [47].

Material	*Mechanical properties*		*Thermal conductivity* ($W\ m^{-1}\ K^{-1}$)	*Electrical conductivity* ($S\ m^{-1}$)
	Stiffness (GPa)	*Strength (GPa)*		
Carbon fibers	300-700	5-7	1 000	About 10^6
Carbon nanotubes	1 000	30-100	> 3 000	10^6-10^7
Graphene	**1 000**	**130**	**5 000**	**6×10^5**
Graphene oxide	**250**	**25**	**9**	**–**
Copper	110-130	–	400	6×10^7

1.3.2.1. Solution blending

Solution blending is the most straightforward method to obtain graphene-polymer composites with intercalated/exfoliated structure by dispersion of graphene (oxide) in a solvent, addition of a

polymer and removal of the solvent by evaporation or distillation. Due to the improved dispersibility, graphene oxide (GO) is often used as a precursor material. However, in order to achieve a homogenous dispersion and avoid GO aggregation, it is vital to ensure good compatibility between the polymer and the filler, therefore occasionally further functionalization of GO is carried out, depending on the polymer used [39]. In addition, in order to restore some of the unique graphene properties, such as electrical conductivity, subsequent reduction of GO is necessary. Graphene (oxide) composites with poly methyl methacrylate [48], polystyrene [49], polycarbonate [50], polyurethane [51], polyvinyl alcohol [52], chitosan [53], sodium alginate [54] have been prepared via this method.

1.3.2.2. Melt mixing

Melt mixing is an industrially attractive process to prepare graphene-polymer composites where graphene (oxide) sheets and the polymer are mixed together by high shear forces at elevated temperatures. However, due to low thermal stability, this method is less suitable for the preparation of GO-polymer composites. Furthermore, it is difficult to achieve a homogenous dispersion of graphene (oxide) sheets inside the polymer matrix and usually a phase-separated composite structure is the result. Nonetheless, graphene composites with polycarbonate [55], polyamide 6 [56] and polyurethane [51] have been prepared via this method.

1.3.2.3. *In situ* polymerization

Graphene (oxide) sheets can be mixed with a monomer/oligomer solution and subsequently polymerized. *In situ* polymerization provides strong interaction between the dispersed and continuous phases as well as good dispersion of the filler particles thus allowing to obtain the exfoliated composite structure. However, the increased solution viscosity at higher weight fractions of the filler complicates mixing and impedes the homogenous dispersion of graphene (oxide) sheets. Nevertheless, graphene (oxide) composites with epoxy [57], polyaniline [58], silicone [59], polystyrene [60], polypropylene [61] have been reported.

1.3.2.4. Layer-by-layer deposition

Layered graphene-polymer composites can be readily produced by the layer-by-layer deposition technique [62], a technique involving alternate dipping of a glass or plastic substrate into graphene (oxide) dispersion and polyelectrolyte solution. This method allows achieving composite films possessing brick-wall-like structure, and as a result such films demonstrate excellent gas barrier properties. Since the preparation method is mainly based on the electrostatic interaction between the constituents, GO instead of graphene is mostly used. Furthermore, the number of positively charged polyelectrolytes is limited, thus making it another constraint. Nonetheless, the composite films with poly(ethylenimine) [63], chitosan [64] and poly(diallyldimethylammonium) chloride [65] have been obtained.

Overall, the outstanding properties of graphene make it very attractive filler for polymer composites. However, in order to promote favorable interactions between graphene sheets and polymer matrix, chemical functionalization is usually required. The use of GO enables one to overcome the dispersibility issues, but subsequent reduction is necessary in order to restore the unique properties of graphene. However, the properties of chemically derived graphene are inferior to those of graphene produced by other methods.

1.4. Scientific gap

As suggested by the Department of Energy (DOE) of the United States of America, composite materials can be listed into sixteen primary types [66a] (Figure 7 A). One type in particular, namely carbon-based polymer composites, has been prioritized by the DOE because of its potential positive impact on clean energy goals [66b] (Figure 7 B).

A

Matrix \ Filler	Ceramic	Carbon	Polymer	Metal
Ceramic	High	Medium		Medium
Carbon			Low	
Polymer	Medium	Priority	Medium	Low
Metal	High	Medium	Medium	High

B

Material	*Density (g/cc)*	*Stiffness (GPa)*	*Strength (MPa)*	*Mass savings (% relative to steel)*	
				Stiffness application	*Strength application*
Steel (common grade)	7.9	205	350	-	-
Glass fiber-polymer composites	2.0	25	300	28-49	71-73
Carbon fiber-polymer composites	1.6	80	1300	48-72	90-95

FIGURE 1.7. (A) Prioritization of different classes of composite materials by the Department of Energy of the United States. (B) Mass saving potentials of various polymer composite materials.

Concurrently, the environmental pollution by synthetic plastics has become a leading threat to wildlife and humanity in multiple ways [67], so a significant effort has been put into the development of biodegradable plastics [68]. However, the use of biodegradable plastics has not yet gained widespread acceptance due to insufficient biodegradability, environmental effects arising from their production methods [69] as well high cost and manufacturing difficulties [70]. Nonetheless, the investigation into properties and applications of biodegradable polymers, especially those occurring naturally (such as starch, cellulose, or alginates), as well as their composites, continues [71].

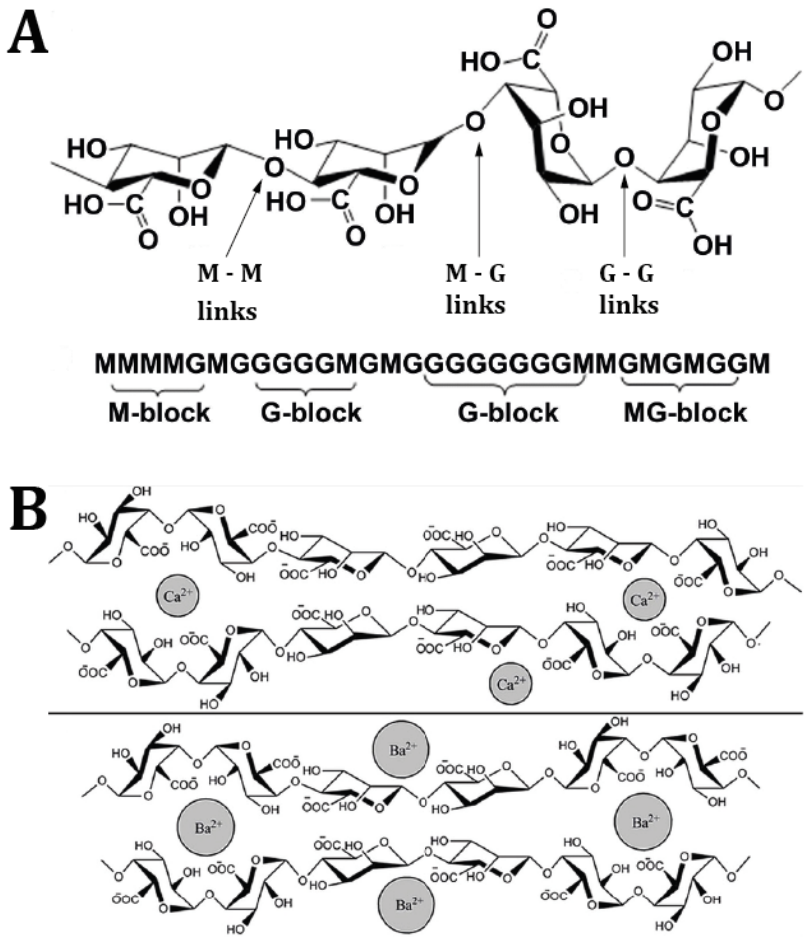

FIGURE 1.8. (A) Representative alginate structure: chain conformation and block distribution. Adapted from [72]. (B) Ion binding sites of different divalent metal ions and alginate chain conformation. Adapted from [73].

Alginate is a naturally occurring copolymer that is found in brown algae or produced by bacteria [74]. As illustrated in Figure 1.8 (A), it is comprised of randomly arranged sequences of β-D-mannuronic acid (M) and α-L-guluronic acid (G) blocks. Since mannuronic acid units form β (1-4) linkages, they are more flexible and assume linear conformations, whereas guluronic acid units are linked together via α (1-4) linkages that introduce a steric hindrance around the carboxylic group, resulting in folded and more rigid structural conformations [11a]. Alginate readily reacts with divalent metal ions to form cross-linked junctions [75], however, the binding of ions appears to be highly selective: for instance, Barium ions bind to G-G and M-M blocks specifically, whereas Calcium – to G-G and M-G blocks [73], see Figure 1.8 (B). Due its biocompatibility, biodegradability, non-toxicity and gelling capability,

alginate and alginate-based compounds are extensively used in pharmaceuticals, medicine, food industry, fuel production, and filtration membranes [11a, 72]. Furthermore, good thermal stability [76] and remarkable innate stiffness [76b, 77] of Sodium alginate and Calcium alginate make them attractive for the use as a polymer matrix in composite materials. In addition, the good solubility of alginic acid Sodium salt in water provides an advantage in the preparation of polymer composites without the use of hazardous organic solvents, provided the filler is also hydrophilic. As introduced earlier, graphene oxide can be readily dispersed in water, hence preparation of Sodium alginate-graphene oxide (Na-Alg/GO) composites by solution blending becomes a viable method. Indeed, a couple of groups have investigated the thermal [54], mechanical [54, 78] and water permeation [79] properties of Na-Alg/GO composites prepared by solution blending. However, the properties of divalent metal ion cross-linked alginate-graphene composites remain unexplored so far. Cross-linking alginate with divalent metal ions yield water insoluble alginates of different properties, which are proper for the use in polymer composites. Furthermore, based on the clean energy goals, organic origin and versatility of the polymer, propitious properties (such as stiffness) of unfilled alginates as well as Na-Alg/GO composites, (reduced) graphene oxide-alginate biopolymer nanocomposites could show potential for coating, separation, proton conductive membrane applications.

1.5. Scope and outline of this thesis

Research described in this thesis aims to investigate the unexplored properties of Calcium alginate-reduced graphene oxide and Barium alginate-reduced graphene oxide films of various compositions. In addition, the properties of the divalent metal ion cross-linked alginates and their composites are compared to the analogous properties of Sodium alginate-graphene oxide composites of the corresponding compositions. Since the filler, graphene oxide, is obtained by the chemical oxidation of graphite, the poorly understood mechanism of chemical graphite oxidation is also explored. The results of *in situ* X-ray diffraction investigation of the samples prepared by the most often-used graphite oxidation protocol are discussed in Chapter 2. In Chapter 3, the origin of the formation of

highly ordered graphene oxide sheets in the Sodium alginate matrix is discussed. Besides, an explanation of the decreased order of reduced graphene oxide sheets in the divalent metal ions cross-linked alginate matrix is provided. Water sorption and water vapor barrier properties of the alginate composites are discussed in Chapter 4. Furthermore, a model that takes into account the orientational order and effective aspect ratio of graphene oxide sheets in the Sodium alginate matrix is employed to accurately predict water vapor barrier properties of the composites at ambient conditions. Complex interactions between the divalent metal ions, polymer and filler sheets that result in difficult-to-predict mechanical properties are discussed in Chapter 5. In addition, the thermal and electrical conductivity properties of the alginate-based (reduced) graphene oxide nanocomposites are also presented. The summary of this thesis and recommendations for future work are outlined in Chapter 6.

1.6. References

1. (a) *Polymer Composites*. Wiley-VCH Verlag GmbH & Co: 2012; Vol. 1; p.814; (b) Sperling, L. H., *Introduction to Physical Polymer Science*. 4th ed.; 2006; p 880.

2. (a) Luo, J. J.; Daniel, I. M. *Compos Sci Technol* **2003,** *63* (11), 1607-1616; (b) Sandler, J. K. W.; Kirk, J. E.; Kinloch, I. A.; Shaffer, M. S. P.; Windle, A. H. *Polymer* **2003,** *44* (19), 5893-5899; (c) Zuiderduin, W. C. J.; Westzaan, C.; Huetink, J.; Gaymans, R. J. *Polymer* **2003,** *44* (1), 261-275; (d) Sorrentino, A.; Tortora, M.; Vittoria, V. *J Polym Sci Pol Phys* **2006,** *44* (2), 265-274.

3. *Handbook of Polymer Blends and Composites*. Smithers Rapra Technology: 2002; Vol. 1-4, p 2420.

4. (a) Pethrick, R. A., *Polymer Science and Technology for Engineers and Scientists*. 1st ed.; Wiley: 2010; (b) Wang, R.; Zheng, S.; Zheng, Y. G., *Polymer Matrix Composites and Technology* 1st ed.; Woodhead Publishing: 2011.

5. Witten, E.; Kraus, T.; Kühnel, M. *Composites Market Report 2014: Market developments, trends, challenges and opportunities*; Federation of Reinforced Plastics: Germany, October 2014; p 44.

6. *Functional Fillers for Plastics*. Wiley-VCH Verlag GmbH & Co. KGaA: 2005.

7. Manas, C.; Salil, K. R., *Plastics Technology Handbook*. 4th ed.; CRC Press 2006; p 672.

8. Osswald, T.; Menges, G., *Materials Science of Polymers for Engineers*. Hanser: 2012.

9. Hamerton, I., Thermosetting and Thermoplastic Polymer Matrices for Composites. PowerPoint slides ed.

10. Murr, L. E., *Handbook of Materials Structures, Properties, Processing and Performance*. Springer International Publishing: 2015; p 1152.

11. (a) *Advances in Natural Polymers: Composites and Nanocomposites*. Springer Science & Business Media: 2012; Vol. 18, p 426; (b) Thakur, V. K.; Thakur, M. K.; Gupta, R. K. *Int J Polym Anal Ch* **2014,** *19* (3), 256-271.

12. Rothon, R. N., *Particulate-Filled Polymer Composites*. 2nd ed.; Smithers Rapra Press: 2003; p 556.

13. Paul, D. R.; Robeson, L. M. *Polymer* **2008,** *49* (15), 3187-3204.

14. ISO/TS 80004-2:2015. In *Nanotechnologies -- Vocabulary -- Part 2: Nano-objects*, The International Organization for Standardization: 2015.

15. Moczo, J.; Pukanszky, B. *J Ind Eng Chem* **2008,** *14* (5), 535-563.

16. Gopakumar, T. G.; Lee, J. A.; Kontopoulou, M.; Parent, J. S. *Polymer* **2002,** *43* (20), 5483-5491.

17. Koper, G. J. M.; Vilcinskas, K. *Colloid Surface A* **2014,** *442*, 2-5.

18. Yousefi, N.; Gudarzi, M. M.; Zheng, Q. B.; Aboutalebi, S. H.; Sharif, F.; Kim, J. K. *J Mater Chem* **2012,** *22* (25), 12709-12717.

19. (a) Gojny, F. H.; Wichmann, M. H. G.; Fiedler, B.; Schulte, K. *Compos Sci Technol* **2005,** *65* (15-16), 2300-2313; (b) Zuiderduin, W. C. J.; Gaymans, R. J. *Abstr Pap Am Chem S* **2005,** *230*, U3522-U3522.

20. (a) Chen, G. H.; Wu, C. L.; Weng, W. G.; Wu, D. J.; Yan, W. L. *Polymer* **2003,** *44* (6), 1781-1784; (b) Huang, J. C. *Adv Polym Tech* **2002,** *21* (4), 299-313.

21. (a) Priolo, M. A.; Gamboa, D.; Grunlan, J. C. *Acs Appl Mater Inter* **2010,** *2* (1), 312-320; (b) Scherillo, G.; Lavorgna, M.; Buonocore, G. G.; Zhan, Y. H. H.; Xia, H. S. S.; Mensitieri, G.; Ambrosio, L. *Acs Appl Mater Inter* **2014,** *6* (4), 2230-2234.

22. (a) Bleach, N. C.; Nazhat, S. N.; Tanner, K. E.; Kellomaki, M.; Tormala, P. *Biomaterials* **2002,** *23* (7), 1579-1585; (b) Berean, K. J.; Ou, J. Z.; Nour, M.; Field, M. R.; Alsaif, M. M. Y. A.; Wang, Y. C.; Ramanathan, R.; Bansal, V.; Kentish, S.; Doherty, C. M.; Hill, A. J.; McSweeney, C.; Kaner, R. B.; Kalantar-zadeh, K. *J Phys Chem C* **2015,** *119* (24), 13700-13712.

23. Alexandre, M.; Dubois, P. *Mat Sci Eng R* **2000,** *28* (1-2), 1-63.

24. Liu, J.; Boo, W. J.; Clearfield, A.; Sue, H. J. *Mater Manuf Process* **2006,** *21* (2), 143-151.

25. Ganesan, V. *J Polym Sci Pol Phys* **2008,** *46* (24), 2666-2671.

26. (a) Hill, R. *J Mech Phys Solids* **1964,** *12*, 119; (b) Hermans, J. J. *Proc Kon Ned Akad v Wetensch B* **1967,** *65* (1), 1-9; (c) Halpin, J. C.; Tsai, S. W. *Effects on factors on composite materials*; AFML-TR-67-423; Air Force Materials Laboratory, Wright Patterson Air Force Base Dayton, Ohio, The United States, 1969; p 61; (d) Mori, T.; Tanaka, K. *Acta Metall Mater* **1973,** *21* (5), 571-574.

27. (a) Rayleigh, L. *Philos. Mag.* **1892,** *34*, 481-502; (b) Barrer, R. M. *T Faraday Soc* **1939,** *35* (1), 0628-0643; (c) Nielsen, L. E. *Journal of Macromolecular Science: Part A - Chemistry* **1967,** *1* (5), 929-942; (d) Cussler, E. L.; Hughes, S. E.; Ward, W. J.; Aris, R. *J Membrane Sci* **1988,** *38* (2), 161-174; (e) Lape, N. K.; Nuxoll, E. E.; Cussler, E. L. *J Membrane Sci* **2004,** *236* (1), 29-37.

28. (a) Hiemenz, P. C.; Rajagopalan, R., *Principles of Colloid and Surface Chemistry, Third Edition, Revised and Expanded*. 3rd ed.; CRC Press 1997; p 672; (b) Israelachvili, J.N., *Intermolecular and Surface Forces*. 3rd ed. 2011: Academic Press. p 704.

29. (a) Uddin, A. J.; Araki, J.; Gotoh, Y. *Biomacromolecules* **2011,** *12* (3), 617-624; (b) Halpin, J. C.; Kardos, J. L. *Polymer Engineering And Science* **1976,** *16* (344), 344-352.

30. Bharadwaj, R. K. *Macromolecules* **2001,** *34* (26), 9189-9192.

31. Chawla, K. K., *Composite Materials: Science and Engineering*. 3rd ed.; Springer Science & Business Media: 2012; p 542.

32. Pukanszky, B. *Eur Polym J* **2005,** *41* (4), 645-662.

33. Allen, K. W. *Physics in Technology* **1988,** *19* (5-6), 234-240.

34. Allen, K. W. *J Adhesion* **1987,** *21* (3-4), 261-277.

35. Novoselov, K. S.; Geim, A. K.; Morozov, S. V.; Jiang, D.; Zhang, Y.; Dubonos, S. V.; Grigorieva, I. V.; Firsov, A. A. *Science* **2004,** *306* (5696), 666-669.

36. (a) Novoselov, K. S.; Fal'ko, V. I.; Colombo, L.; Gellert, P. R.; Schwab, M. G.; Kim, K. *Nature* **2012,** *490* (7419), 192-200; (b) Singh, V.; Joung, D.; Zhai, L.; Das, S.; Khondaker, S. I.; Seal, S. *Prog Mater Sci* **2011,** *56* (8), 1178-1271.

37. Geim, A. K.; Novoselov, K. S. *Nat Mater* **2007,** *6* (3), 183-191.

38. Seah, C. M.; Chai, S. P.; Mohamed, A. R. *Carbon* **2014,** *70*, 1-21.

39. Kuila, T.; Bose, S.; Mishra, A. K.; Khanra, P.; Kim, N. H.; Lee, J. H. *Prog Mater Sci* **2012,** *57* (7), 1061-1105.

40. (a) Hernandez, Y.; Nicolosi, V.; Lotya, M.; Blighe, F. M.; Sun, Z. Y.; De, S.; McGovern, I. T.; Holland, B.; Byrne, M.; Gun'ko, Y. K.; Boland, J. J.; Niraj, P.; Duesberg, G.; Krishnamurthy, S.; Goodhue, R.; Hutchison, J.; Scardaci, V.; Ferrari, A. C.; Coleman, J. N. *Nat Nanotechnol* **2008,** *3* (9), 563-568; (b) Khan, U.; O'Neill, A.; Lotya, M.; De, S.; Coleman, J. N. *Small* **2010,** *6* (7), 864-871.

41. Ciesielski, A.; Samori, P. *Chem Soc Rev* **2014,** *43* (1), 381-398.

42. (a) Brodie, B. C. *Phil. Trans. R. Soc. Lond.* **1859,** (149), 249-259; (b) Staudenmaier, L. *Berichte der deutschen chemischen Gesellschaft* **1898,** (31), 1481–1487; (c) Hofmann, U.; Konig, E. *Zeitschrift Fur Anorganische Und Allgemeine Chemie* **1937,** *234* (1), 311-336; (d) Hummers, W. S.; Offeman, R. E. *J Am Chem Soc* **1958,** *80* (6), 1339-1339.

43. Li, D.; Muller, M. B.; Gilje, S.; Kaner, R. B.; Wallace, G. G. *Nat Nanotechnol* **2008,** *3* (2), 101-105.

44. Mao, S.; Pu, H. H.; Chen, J. H. *Rsc Adv* **2012,** *2* (7), 2643-2662.

45. Pei, S. F.; Cheng, H. M. *Carbon* **2012,** *50* (9), 3210-3228.

46. (a) Kim, H.; Abdala, A. A.; Macosko, C. W. *Macromolecules* **2010,** *43* (16), 6515–6530; (b) Potts, J. R.; Dreyer, D. R.; Bielawski, C. W.; Ruoff, R. S. *Polymer* **2011,** *52* (1), 5-25; (c) Verdejo, R.; Bernal, M. M.; Romasanta, L. J.; Lopez-Manchado, M. A. *J Mater Chem* **2011,** *21* (10), 3301-3310; (d) Huang, X.; Qi, X. Y.; Boey, F.; Zhang, H. *Chem Soc Rev* **2012,** *41* (2), 666-686.

47. (a) *Springer Handbook of Nanomaterials*. 1 ed.; Springer-Verlag Berlin Heidelberg: 2013; (b) Balandin, A. A.; Ghosh, S.; Bao, W. Z.; Calizo, I.; Teweldebrhan, D.; Miao, F.; Lau, C. N. *Nano Lett* **2008,** *8* (3), 902-907; (c) Cao, C. H.; Daly, M.; Singh, C. V.; Sun, Y.; Filleter, T. *Carbon* **2015,** *81*, 497-504; (d) Du, X.; Skachko, I.; Barker, A.; Andrei, E. Y. *Nat Nanotechnol* **2008,** *3* (8), 491-495; (e) Gomez-Navarro, C.; Burghard, M.; Kern, K. *Nano Lett* **2008,** *8* (7), 2045-2049; (f) Lee, C.; Wei, X. D.; Kysar, J.

W.; Hone, J. *Science* **2008,** *321* (5887), 385-388; (g) Shen, X.; Lin, X. Y.; Jia, J. J.; Wang, Z. Y.; Li, Z. G.; Kim, J. K. *Carbon* **2014,** *80*, 235-245.

48. Ramanathan, T.; Stankovich, S.; Dikin, D. A.; Liu, H.; Shen, H.; Nguyen, S. T.; Brinson, L. C. *J Polym Sci Pol Phys* **2007,** *45* (15), 2097-2112.

49. Stankovich, S.; Dikin, D. A.; Dommett, G. H. B.; Kohlhaas, K. M.; Zimney, E. J.; Stach, E. A.; Piner, R. D.; Nguyen, S. T.; Ruoff, R. S. *Nature* **2006,** *442* (7100), 282-286.

50. Higginbotham, A. L.; Lomeda, J. R.; Morgan, A. B.; Tour, J. M. *Acs Appl Mater Inter* **2009,** *1* (10), 2256-2261.

51. Kim, H.; Miura, Y.; Macosko, C. W. *Chem Mater* **2010,** *22* (11), 3441-3450.

52. Liang, J. J.; Huang, Y.; Zhang, L.; Wang, Y.; Ma, Y. F.; Guo, T. Y.; Chen, Y. S. *Adv Funct Mater* **2009,** *19* (14), 2297-2302.

53. Wang, X. L.; Bai, H.; Yao, Z. Y.; Liu, A. R.; Shi, G. Q. *J Mater Chem* **2010,** *20* (41), 9032-9036.

54. Ionita, M.; Pandele, M. A.; Iovu, H. *Carbohyd Polym* **2013,** *94* (1), 339-344.

55. Kim, H.; Macosko, C. W. *Polymer* **2009,** *50* (15), 3797-3809.

56. Steurer, P.; Wissert, R.; Thomann, R.; Mulhaupt, R. *Macromol Rapid Comm* **2009,** *30* (4-5), 316-327.

57. Rafiee, M. A.; Rafiee, J.; Wang, Z.; Song, H. H.; Yu, Z. Z.; Koratkar, N. *Acs Nano* **2009,** *3* (12), 3884-3890.

58. Zhang, K.; Zhang, L. L.; Zhao, X. S.; Wu, J. *Chem Mater* **2010,** *22* (4), 1392–1401.

59. Verdejo, R.; Barroso-Bujans, F.; Rodriguez-Perez, M. A.; de Saja, J. A.; Lopez-Manchado, M. A. *J Mater Chem* **2008,** *18* (19), 2221-2226.

60. Fang, M.; Wang, K. G.; Lu, H. B.; Yang, Y. L.; Nutt, S. *J Mater Chem* **2009,** *19* (38), 7098-7105.

61. Huang, Y. J.; Qin, Y. W.; Zhou, Y.; Niu, H.; Yu, Z. Z.; Dong, J. Y. *Chem Mater* **2010,** *22* (13), 4096-4102.

62. *Multilayer Thin Films: Sequential Assembly of Nanocomposite Materials*. Wiley-VCH Verlag&Co: Germany, 2012; Vol. 1.

63. (a) Yu, L.; Lim, Y. S.; Han, J. H.; Kim, K.; Kim, J. Y.; Choi, S. Y.; Shin, K. *Synthetic Met* **2012,** *162* (7-8), 710-714; (b) Gokhale, A. A.; Lu, J.; Parker, N. J.; Izbicki, A. P.; Sanyal, O.; Lee, I. *J Colloid Interf Sci* **2013,** *409*, 219-226; (c) Yang, Y. H.; Bolling, L.; Priolo, M. A.; Grunlan, J. C. *Adv Mater* **2013,** *25* (4), 503-508.

64. Tzeng, P.; Stevens, B.; Devlaming, I.; Grunlan, J. C. *Langmuir* **2015,** *31* (21), 5919–5927.

65. Rajasekar, R.; Kim, N. H.; Jung, D.; Kuila, T.; Lim, J. K.; Park, M. J.; Lee, J. H. *Compos Sci Technol* **2013,** *89*, 167-174.

66. (a) *Advanced Composites Materials and their Manufacture Technology Assessment*; U.S. Department of Energy: United States, p 37; (b) *Innovating Clean Energy Technologies In Advanced Manufacturing*; Quadrennial Technology Review 2015; U.S. Department of Energy: United States, p 40.

67. Thompson, R. C.; Moore, C. J.; vom Saal, F. S.; Swan, S. H. *Philos T R Soc B* **2009,** *364* (1526), 2153-2166.

68. Gross, R. A.; Kalra, B. *Science* **2002,** *297* (5582), 803-807.

69. Shah, A. A.; Hasan, F.; Hameed, A.; Ahmed, S. *Biotechnol Adv* **2008,** *26* (3), 246-265.

70. Ghanbarzadeh, B.; Almasi, H., Biodegradable Polymers. In *Biodegradation-Life of Science*, Chamy, R.; Rosenkranz, F., Eds. InTech: 2013; pp 141-185.

71. *Eco-friendly Polymer Nanocomposites: Chemistry and Applications*. 1 ed.; Springer India: 2015; Vol. 74.

72. Pawar, S. N.; Edgar, K. J. *Biomaterials* **2012,** *33* (11), 3279-3305.

73. Juárez, G. A. P.; Spasojevic, M.; Faas, M. M.; de Vos, P. *Frontiers in Bioengineering and Biotechnology* **2014,** *2* (26).

74. Rinaudo, M. *Polym Int* **2008,** *57* (3), 397-430.

75. Smidsrød, O.; Haug, A. *Acta Chemica Scandinavica* **1965,** (19), 341-351.

76. (a) Soares, J. P.; Santos, J. E.; Chierice, G. O.; Cavalheiro, E. T. G. *Eclética Química* **2004,** (29), 57-63; (b) Russo, R.; Malinconico, M.; Santagata, G. *Biomacromolecules* **2007,** *8* (10), 3193-3197.

77. Avella, M.; Di Pace, E.; Immirzi, B.; Impallomeni, G.; Malinconico, M.; Santagata, G. *Carbohyd Polym* **2007,** *69* (3), 503-511.

78. Chen, K.; Shi, B.; Yue, Y. H.; Qi, J. J.; Guo, L. *Acs Nano* **2015,** *9* (8), 8165-8175.

79. Cao, K. T.; Jiang, Z. Y.; Zhao, J.; Zhao, C. H.; Gao, C. Y.; Pan, F. S.; Wang, B. Y.; Cao, X. Z.; Yang, J. *J Membrane Sci* **2014,** *469*, 272-283.

CHAPTER 2

IN SITU X-RAY DIFFRACTION STUDIES OF GRAPHITE OXIDATION REACTION

Parts of this Chapter have been submitted for publication:

Vilcinskas, K., Mulder, F. M., Picken, S. J., Koper, G. J. M. *In situ X-ray diffraction of the graphite oxidation reaction indicating different exfoliation mechanism than ex situ studies*. Submitted to Nanoscale, 2016.

ABSTRACT

This Chapter summarizes state-of-the-art solvent-based production methods of graphene, outlines the chemical oxidation methods to produce chemically derived graphene precursor material – graphite oxide, and the current knowledge of the formation mechanism of graphite oxide. In addition, the results of *in situ* X-ray diffraction investigation of this process are presented, discussed and contrasted to the findings by other authors, who examined the same process by employing *ex situ* X-ray diffraction.

During sonication or shearing of graphite powder in solvents, high shear forces and cavitation bubbles provide enough energy to separate graphene sheets and to produce stable graphene dispersions in organic solvents provided that the surface energy of the solvent of choice matches to that of graphene. The concentration of graphene in such dispersions can be further increased by the use of surfactants, polymers or pyrene derivatives, as the stabilizers provide the sustaining effect to exfoliated graphene sheets. Although promising, these methods yield only moderate amounts of graphene, so graphene-like material production via graphite oxide remains the most popular method. Nevertheless, solvent-based production of graphene offers a basis of understanding of the stability of mechanisms of graphene dispersions.

On the other hand, despite some efforts, the exact mechanism of graphite oxide formation by the chemical oxidation of graphite remains uncertain, although it has been proposed that it follows graphite-sulfuric acid/graphite intercalation compound-graphite oxide route. Our results suggest that, in contrast to the reports by other authors, no strong crystalline order, unique to these compounds, develops if they remain in concentrated acid. Furthermore, it also appears that, depending on the concentration, sulfuric acid molecules significantly weaken graphene-graphene interactions in graphite. Consequently, concentrated sulfuric acid may be a good solvent for graphene dispersions, if only there is sufficient energy input to separate the layers of graphene.

2.1. General introduction

The interest in graphene, the basic structural element of graphite, and its applications has not withered but has rather been steadily increasing ever since its isolation, for the first time in 2004 [1] (Figure 2.1 A). Due to its unique properties, such as exceptional inherent stiffness [2], impermeability to gases [3] and excellent electrical [4] and thermal conductivity [5], graphene has been the subject of investigation in a variety of scientific areas (Figure 2.1 B). Indeed, graphene and its derivatives have found applications in polymer composites [6], inorganic composites [7], sensors [8], photocatalysis [9], electrodes [10], catalysts [11], biomedicine [12] and electronic devices [13]. However, the properties and hence the performance of graphene-based materials are strongly influenced by the preparation method of graphene [14].

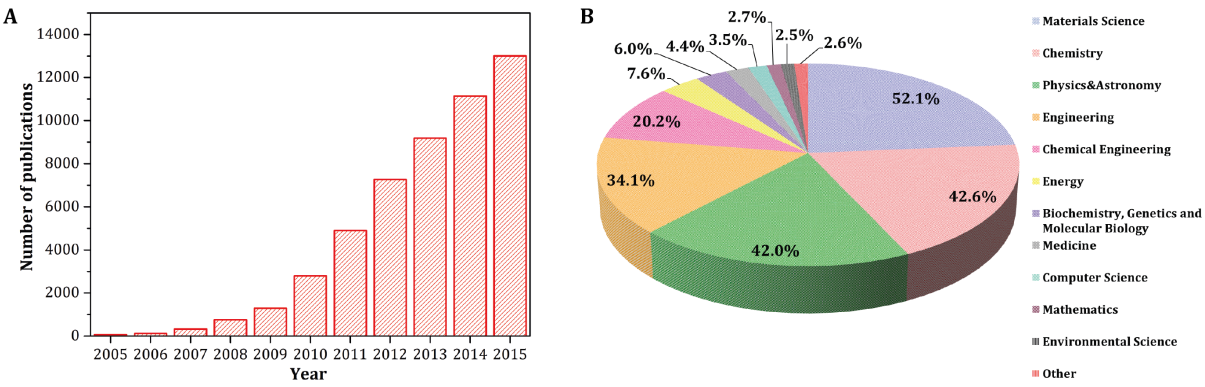

FIGURE 2.1. (A) Number of publications containing graphene as a keyword between 2005-2015. (B) Documents by subject areas. Retrieved from Scopus.

There are a few graphene preparation methods, a summary of the most important are presented in Table 2.1.

TABLE 2.1. Summary of preparation methods of graphene and its derivatives

Method	*Description*	*Advantages*	*Disadvantages*
Mechanical cleavage [1]	Exfoliation of highly oriented pyrolytic graphite by Scotch tape	Superb quality of mono-, bi-layer graphene sheets	Laborious; low production scale
Chemical vapour deposition [15]	Decomposition of hydrocarbon gases followed by carbon dissolution and precipitation on transition metal substrates	High quality and large graphene sheets	Low production scale
Exfoliation in solvents [16]	Prolonged ultrasonication of graphite dispersions in solvents	Simplicity of the method, adequate quality of few layer graphene sheets	Prolonged sonication reduces size of graphene sheets; limited number of suitable solvents
Organic synthesis [17]	Synthesis of graphene-like polycyclic hydrocarbons	Versatility of synthetic routes; capability of chemical modification	Difficult preservation of dispersibility, and planar geometry of bigger graphene sheets
Chemical derivation of graphene [18]	Oxidation of graphite with strong oxidants	Relatively large production scale; improved dispersibility in solvents	Final product is graphite oxide rather than graphene; subsequent reduction is required to restore properties comparable that of graphene; structural defects in reduced graphene sheets

The envisaged application of graphene-based products usually determines the selection of the preparation method. Preparation methods of high quality graphene are generally labour-intensive, expensive and produce only modest quantities of graphene and are therefore mainly used to provide the material for investigation of its intrinsic properties. On the other hand, due to the remarkable properties of graphene, large scale production is desired, and, thus, considerable effort has been put into the development of large scale production methods [19]. One method in particular, namely the chemical oxidation of graphite, offers the most viable route for obtaining relatively large

quantities of graphene-like material. During the oxidation process of graphite, hydroxyl and epoxy groups along with a small number of ester and tertiary alcohol groups evolve on the basal plane of graphene sheets, whereas carbonyl, carboxy and 5-6 member ring lactols decorate the edges of graphene sheets [20]. Oxidation of graphite disrupts the sp^2-hybridized structure of graphene, and increases the interlayer spacing between sheets due to the introduction of the oxygenated groups, which confer dispersibility in a variety of solvents [21], most importantly water. In addition, the oxygenated groups on graphene oxide sheets offer different routes for chemical functionalization [22] that improve the compatibility with the polymer matrix in graphene-based-polymer composites. Furthermore, the elimination of these groups allows one to obtain reduced graphene oxide [23] that possesses properties comparable to those of graphene as obtained by other methods. Although the chemical derivation of graphene has become the most widely employed method, the exact oxidation mechanism of the precursor – graphite – remains poorly understood [24].

In this study we review the solvent-based graphene preparation methods as these methods use the same precursor material that upon sonication in solvents yield graphene dispersions. We also briefly discuss the stability of such graphene dispersions. In addition, we outline the chemical oxidation methods and the prevailing knowledge on the formation of graphite oxide. Lastly, we present and discuss the rather surprising results of an *in situ* X-ray diffraction study of the graphite oxidation reaction, which has, in contrast to *ex situ* diffraction results, not yet been reported in literature.

2.2. Solvent exfoliation of graphite

Amongst the many graphene production methods, direct exfoliation of graphite in liquids has gained significant popularity [16b, 25]. The formation of cavitation bubbles and the high shear forces induced by sonication of powder graphite in a solvent provide enough energy to separate the layered structure of graphite and yield mono-, bi- and few-layer defect-free graphene sheets [26]. Although the yield of such procedures is low, ≤0.01 mg mL^{-1} depending on the solvent [27], it can be increased by prolonging sonication time and/or increasing ultrasound power at the expense of the size of graphene sheets [26]. A recent study [28] has demonstrated that similar concentration graphene dispersions can be produced by shear exfoliation of graphite powder in N-methyl-2-pyrrolidone. Here, the change in graphite concentration, shearing time, speed, and solvent volume enable to change the concentration of the resulting graphene dispersion. Whether shearing or sonication of graphite powder in solvents, the experimental evidence has led to conclude that those solvents, such as N-methyl-2-pyrrolidone and/or *N*,*N*-dimethylformamide, that have a surface energy of about 70 mJ m^{-2}, yield the highest concentration, up 1.2 mg mL^{-1} depending on the sonication time and power, graphene dispersions. Accordingly, it has been proposed that the surface energy of such solvents matches that of the graphene sheets, and as a result, is able to counter-balance the attractive van der Waals forces between the sheets, thereby preventing the exfoliated graphene sheets from aggregating [29]. However, the high boiling point and toxicity of the most studied solvents have prompted investigation into the use of milder systems. Exploration of low boiling point organic solvents, such as 1-propanol [30], chloroform [31] or acetonitrile [32], and/or solvent exchange strategies, which involve transferring graphene dispersions obtained in a high boiling point solvent to a low boiling point solvent [33], have only acquired limited success. Indeed, since the enthalpy of vaporization of a solvent is directly related to the surface energy of the solvent, only the high boiling point solvents are advantageous to prepare relatively concentrated graphene dispersions.

Another strategy to produce stable and aqueous graphene dispersions has been to employ surfactants [34], polymers [35] or pyrene derivatives [36]. The use of surfactants or polymers enables the reduction of the interfacial surface tension between graphene sheets and solvent molecules, thus promoting the stability of graphene dispersions. Ionic surfactants stabilize graphene sheets by van der Waals and/or hydrophobic interactions between the hydrophobic tails of the surfactant molecules and the graphene sheets while the hydrophilic head groups dissociate in water. Thus, graphene sheets become charged, and the associated electrical double layer repulsion ensures the stability of such dispersions [34a]. Non-ionic surfactants, on the other hand, balance graphene sheets by steric effects of protruded hydrophilic tails whereas hydrophobic tails attach to the graphene sheets by van der Waals and/or hydrophobic interactions [34c]. The steric effects are also thought to stabilize graphene dispersions in the presence of macromolecules. Stabilization of graphene dispersions by surfactants or polymers allows achieving higher concentrations of about 0.1-0.2 mg mL^{-1}, however the excess of stabilizer potentially has an adverse effect on its properties for the final graphene applications. Stabilization of graphene dispersions with pyrene derivatives has so far allowed the highest concentrations, up to 1 mg mL^{-1}, graphene dispersions, thus making it a very promising method. In this case, it is thought, graphene sheets are stabilized by π- π interactions between basal planes of graphene sheets and stabilizer molecules. If pyrene derivatives are decorated with electron withdrawing groups, such as sulfonic acid, donor-acceptor interactions also contribute to the stability of graphene dispersions.

Overall, due the simplicity of the method, direct exfoliation of graphite in solvents is an attractive way to obtain graphene dispersions. However, its application still remains limited by the number of suitable solvents and the resulting low graphene concentrations. Exfoliation of graphite in aqueous solutions containing surfactant or polymer molecules can increase the concentration of graphene dispersions, but the excess of stabilizer molecules can impair their properties, such as the electrical conductivity, of final graphene products.

2.3. Graphene from other graphitic compounds

It has long been known that lamellar compounds of graphite – so called graphite intercalation compounds (GIC) – can be produced by (electro)chemical oxidation of graphite powder in concentrated acids [37], although recently Kovtyukhova and co-authors have reported [38] that non-oxidative intercalation of some mineral acids, such as H_3PO_4 or H_2SO_4, in between graphene sheets of graphite, is possible at ambient conditions. A preceding study by Moissette et al. [39] showed that sulfuric acid-GICs could be obtained without supplying oxidizing agents, however the compound was produced at elevated temperatures where the acid decomposed yielding SO_3 species that are capable of oxidation. During the classical oxidation process of graphite in concentrated acids, before yielding the final product – graphite oxide – anions as well as neutral acid molecules intercalate between the layers of graphene forming GICs of various degrees of intercalation. In order to initiate the formation of these compounds, a small amount of oxidizing agent or the application of a voltage is often used to initiate the electron transfer reactions leading to intercalating species [40]. GICs are classified by their stage index, which denotes the number of graphene layers between adjacent intercalate layers [41]. Thus, in the first stage (n=1) GIC, the intercalating species fill every gallery between graphene sheets, whereas in higher stage GICs, the intercalating species occupy the interlayer space between the adjacent graphene sheets in alternate fashion leaving a certain number of unfilled galleries (see Figure 2.2).

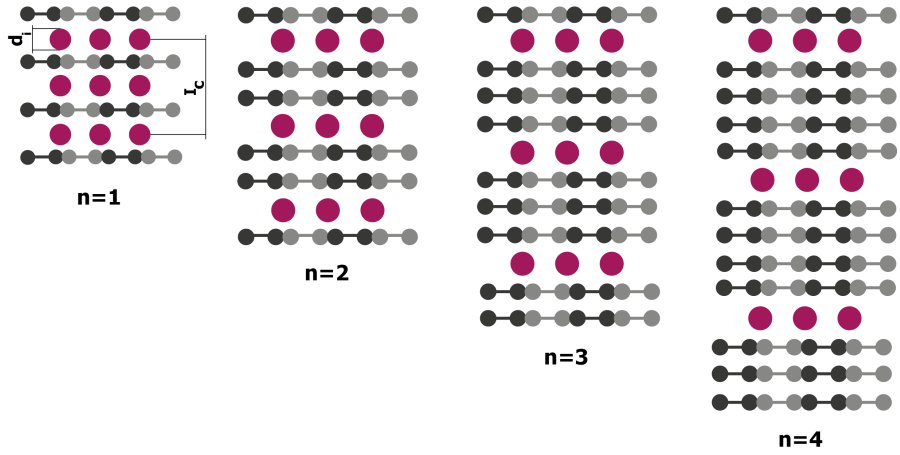

FIGURE 2.2. Schematic illustration of lamellar graphite intercalation compounds. Dark dots and lines represent graphene sheets in graphite whereas bigger red circles – intercalated species.

As the stacking order of graphene layers is not compromised during the intercalation process, GICs can be analysed by means of X-ray diffraction [41-42]. By the application of Bragg's Law [43], the stage of intercalation *n* can be obtained using the following relation [44]:

$$I_c = nc_0 + d_i \qquad (2.1)$$

where I_c is the repeat distance, c_0 – the distance between the adjacent graphene sheets (3.35 Å), and d_i – the size of the intercalating molecules.

In order to obtain GICs electrochemically, graphite as the anode material is immersed in a concentrated acid bath and a Platinum wire is used as the cathode. Upon application of voltage, electrons from graphite are withdrawn and flow to the counter electrode. As suggested by Metrot [45], upon removal of an electron, the potential energy of graphite rises and when it reaches a certain threshold value, anions as well as neutral acid molecules can intercalate between the layers of graphite forming GICs of different stages. The formation of GICs by electrochemical oxidation of graphite where samples were taken out of the reaction mixture at various times during the process has been extensively investigated by many authors [46], including direct monitoring of the intercalation process [47]. Recently, the method has also been employed in the production of

graphene dispersions [48].

TABLE 2.2. Summary of chemical oxidation methods to produce graphite oxide

Method	*Oxidant*	*Solvent*
Brodie [18a]	$KClO_3$	Fumic HNO_3
Staudenmaier [18b]	$KClO_3$	Mixture of concentrated H_2SO_4 and fumic HNO_3
Hoffman [18c]	$KClO_3$	Mixture of concentrated H_2SO_4 and concentrated HNO_3
Hummers [18d]	$NaNO_3$, $KMnO_4$	Concentrated H_2SO_4
Modified Hummers [49]	First stage: $K_2S_2O_8$, P_2O_5 Second stage: $KMnO_4$	Concentrated H_2SO_4
Improved Hummers [50]	$KMnO_4$	Mixture of concentrated H_2SO_4 and concentrated H_3PO_4

Since the production methods (see Table 2.2) of chemically derived graphene involve graphite oxidation in concentrated acid with strong oxidants, it is natural to surmise that the oxidation step is preceded by the formation of GICs. Indeed, in the early 1940s Hofmann and Rüdorff [41] investigated GICs produced in concentrated sulfuric acid by various oxidizing agents. X-ray diffraction analysis of the samples revealed formation of GICs of various stages, generally proceeding from the higher stage to the lower, before yielding graphite oxide. In addition, they also suggested the sulfuric acid-GIC composition to be about C_{24}^{+} HSO_4^{-}. Later studies by other authors [51] corroborated the findings, and the formula of the sulfuric acid-GIC compound has been refined to be $C_{(21\text{-}28)}^{+}$ HSO_4^{-} $2.5H_2SO_4$ [44]. However, it is worth to point out that these studies were conducted *ex situ*. As the GICs are only stable in concentrated acids and readily decompose if exposed to water (vapor) [41], the analysis of

these compounds is generally done by taking a small amount of the sample during the oxidation process, wrapping it in a plastic film to be analysed in an X-ray diffractometer. No studies in the literature have reported on *in situ* investigation into the structural changes of graphite during the chemical oxidation process as yet.

2.4. Experimental section

2.4.1. Sample preparation

For the *in situ* studies, 0.1 gram of fine graphite (Gr) powder (Fluka) was dispersed in 4 millilitres of concentrated (≥95%) sulphuric acid (H_2SO_4, Sigma Aldrich) followed by the addition of different amounts of Potassium permanganate ($KMnO_4$, Sigma Aldrich), see Table 2.3 below. The samples were vigorously mixed and a small aliquot (approximately 0.5 mL) was quickly transferred to the specially built sample holder for analysis. The same procedure was repeated for the samples dispersed in different concentrated acid solutions (constant Gr mass; 2.5 m/v % in an acid solution) or containing different amounts of Gr (constant acid concentration; 95 wt% H_2SO_4), see Table 2.4 for the detailed compositions.

TABLE 2.3. Sample compositions in *in situ* graphite oxidation reaction analysis.

Sample name	*Mass ratio of Gr: $KMnO_4$*
No oxidation (S-1)	1:0
Little oxidation (S-2)	1:1.2
Partial oxidation (S-3)	1:2.3
Full oxidation (S-4)	1:3.5

TABLE 2.4. Different sample compositions to evaluate acid or graphite (Gr) concentration effects.

Sample composition (constant Gr mass)	*Molar ratio of* $Gr:H_2SO_4$	*Sample composition* (constant acid concentration; 95 wt% H_2SO_4)	*Molar ratio of* $Gr:H_2SO_4$
50 wt% H_2SO_4	0.29 : 1.00	2.5 w/v %	0.11 : 1.00
80 wt% H_2SO_4	0.15 : 1.00	6.3 w/v %	0.28 : 1.00
90 wt% H_2SO_4	0.12 : 1.00	12.5 w/v %	0.57 : 1.00
95 wt% H_2SO_4	0.11 : 1.00	25.0 w/v %	1.13 : 1.00

2.4.2. Characterization

The sample holder was specially designed and consisted of two sealable circular stainless steel plates. In the middle of the bottom plate, a circular rostrum of a few millimetres height and 1 centimetre in diameter was designed with the inlet cover, made of the high-density polyethylene to order to protect stainless steel from the chemicals. In the middle of the top plate a window, covered with polyimide film, was installed thus enabling the X-ray beam to penetrate into the sample.

X-ray diffraction (XRD) measurements in Bragg–Brentano reflection mode were performed by a PANalytical X'Pert Pro PW3040/60 diffractometer with Cu Kα radiation operating at 45 kV and 40 mA in an angular 2θ range of 5°-50° at 25°C.

2.5. Results

Before undertaking an analysis of the mixture samples, we have investigated X-ray diffraction patterns of pure graphite (Gr), Potassium permanganate ($KMnO_4$) and the empty sample holder, see Figure 2.3.

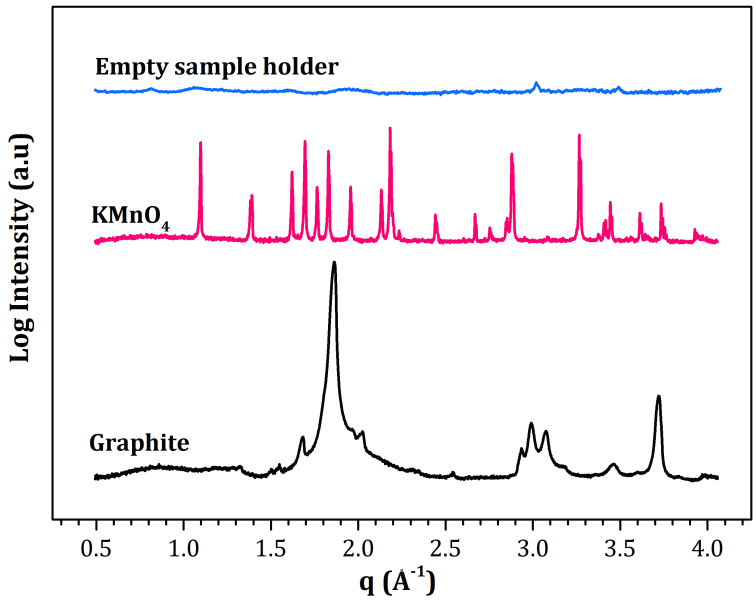

FIGURE 2.3. X-ray diffractograms of graphite (bottom), Potassium permanganate (middle) and empty sample holder (top). Note that the ordinate axis is in the ^{10}log scale.

As presented in Figure 2.3, the X-ray diffraction pattern of the Gr powder sample shows the characteristic peaks at 1.9 $Å^{-1}$, 3.0 $Å^{-1}$, 3.1 $Å^{-1}$ and 3.7 $Å^{-1}$ that correspond to (002), (100), (101) and (004) reflections, respectively [52]. As for the $KMnO_4$ powder sample, it exhibits numerous reflections due to its more complex arrangement of atoms [53]. The empty sample holder, on the other hand, shows no significant crystalline structure, which is characteristic for Kapton® polyimide film [54]. After we collected the X-ray diffraction patterns of the powder samples, we set out to examine the X-ray scattering of the Gr/H_2SO_4 mixtures containing different amounts of $KMnO_4$ by continuously measuring the samples for prolonged periods of time, see Figure 2.4.

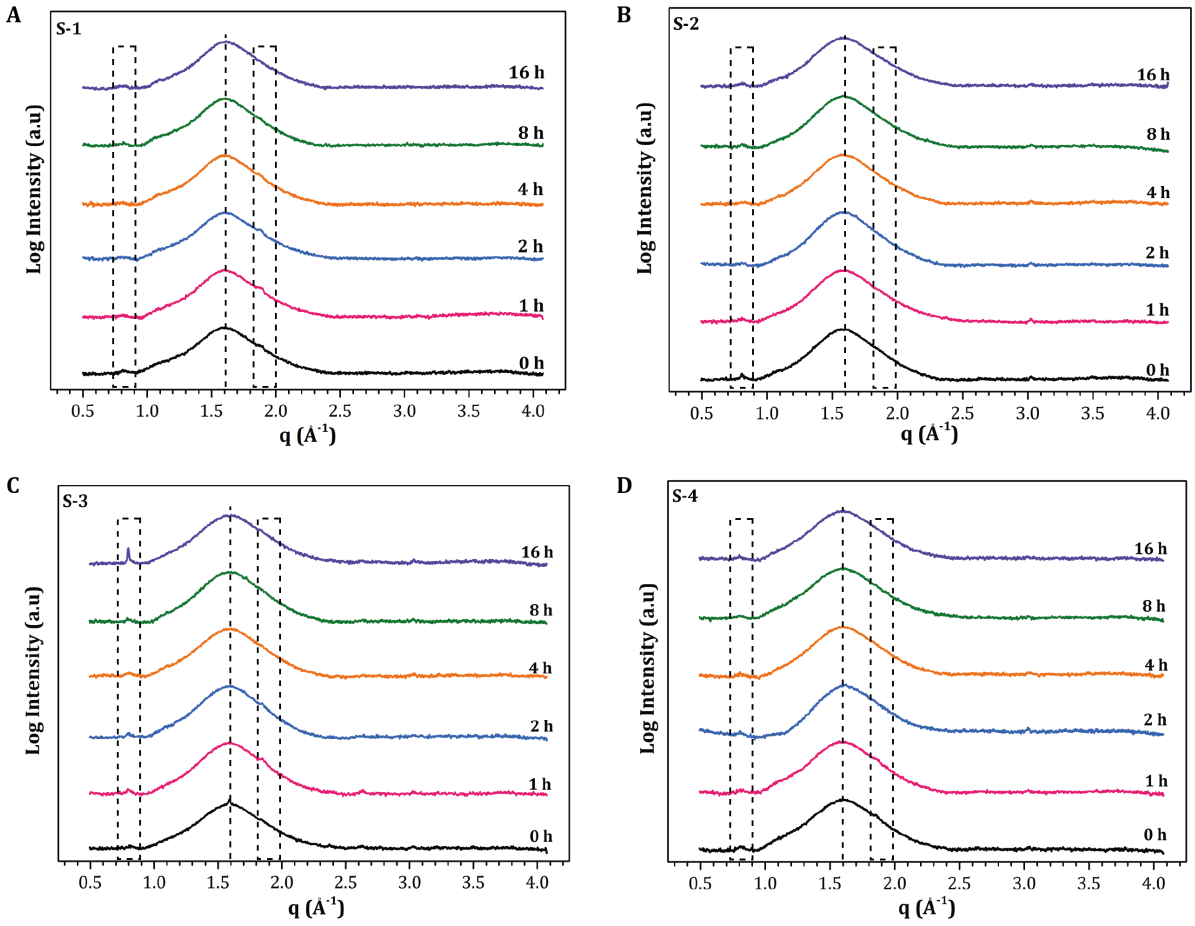

FIGURE 2.4. X-ray diffractograms of graphite (Gr) and sulphuric acid mixture with different amounts of added Potassium permanganate ($KMnO_4$): (A) in the absence of $KMnO_4$; (B) mass ratio Gr: $KMnO_4$=1:1.2; (C) mass ratio Gr: $KMnO_4$=1:2.3; and (D) mass ratio Gr: $KMnO_4$=1:3.5. The samples were measured at various times. The dotted lines draw attention to the most significant positions in the diffractograms.

As seen in Figure 2.4 (A), upon addition of Gr in H_2SO_4, the intensity of the prominent Gr peak at 1.9 $Å^{-1}$ significantly decreased, became broader and gradually disappeared for longer times, whereas other characteristic reflections of Gr became invisible. On the other hand, the broad and intense peak at 1.6 $Å^{-1}$ appeared and remained apparent at all times as has the weak peak at 0.8 $Å^{-1}$. Upon addition of a small amount of $KMnO_4$ (mass ratio Gr: $KMnO_4$=1:1.2) to the Gr /H_2SO_4 mixture (Figure 2.4 B), the prominent Gr peak at 1.9 $Å^{-1}$ almost disappeared altogether, and a strong broad peak at 1.6 A^{-1} along with the weak peaks at 0.8 $Å^{-1}$ and 3.0 $Å^{-1}$ were visible at all times. With further addition

of $KMnO_4$ (mass ratio Gr: $KMnO_4$=1:2.3), (Figure 2.4 C), the peak at 1.6 $Å^{-1}$ remained prominent, the intensity of the peak at 0.8 $Å^{-1}$ slightly increased and the peak at 3.0 $Å^{-1}$ diminished. In addition, a new weak peak at 2.6 $Å^{-1}$ arose, however it remained visible only at certain times. The characteristic Gr peak at 1.9 $Å^{-1}$, albeit broadened and weakened, was also initially visible, but disappeared later. Finally, as shown in Figure 2.4 (D), with completed addition of $KMnO_4$ as prescribed in the Hummer's method (mass ratio Gr: $KMnO_4$=1:3.5) to the Gr/H_2SO_4 mixture, the peaks at 0.8 $Å^{-1}$ and 1.6 $Å^{-1}$ remained visible with no observable development of new peaks.

In order to gain a better understanding of the origin of the observed peaks, we analysed a series of samples, containing graphite in varying H_2SO_4 concentration (2.5 w/v % graphite in acid). In addition, we also varied the concentration of graphite in concentrated H_2SO_4.. All samples were measured within 20 minutes after preparation, and their X-ray diffractograms are presented in Figure 2.5.

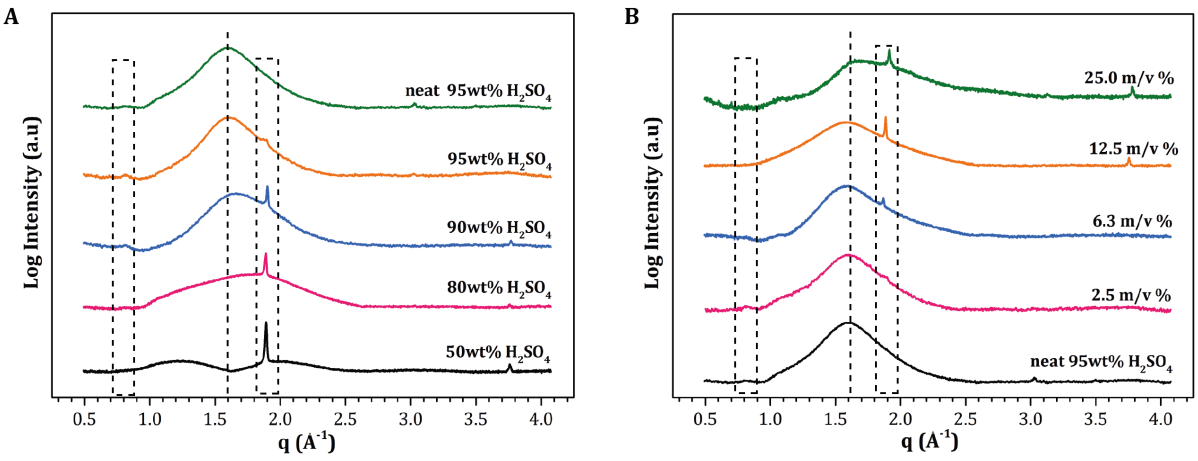

FIGURE 2.5. X-ray diffractograms of (A) graphite in different concentration H_2SO_4 acid solutions (2.5 w/v % graphite in acid), and (B) of various amounts of graphite in concentrated H_2SO_4. The dotted lines draw attention to the most significant positions in the diffractograms.

As seen in Figure 2.5 (A), with increasing acid concentration, the broad peak between 1.5 $Å^{-1}$-2.0 $Å^{-1}$ began to emerge and eventually centred at 1.6 $Å^{-1}$ for high concentrations of H_2SO_4. On the other hand, with increasing acid concentration, the intensity of the characteristic Gr peak at 1.9 $Å^{-1}$ as well as the peak at 3.7 $Å^{-1}$ gradually diminished. As illustrated in Figure 2.5 (B), with increasing amount of

Gr in concentrated H_2SO_4, the characteristic peaks at 1.9 $Å^{-1}$ and 3.7 $Å^{-1}$ became more prominent. However, the broad peak at 1.6 $Å^{-1}$ did not change its shape nor position with the amount of Gr, nonetheless, at the highest investigated Gr concentration in concentrated H_2SO_4, it skewed and moved to 1.7 $Å^{-1}$. In addition, at higher concentrations of Gr, the broad and weak peak at 1.1 $Å^{-1}$ became visible.

2.6. Discussion

We anticipated that monitoring the graphite oxidation reaction *in situ* by means of X-ray diffraction, would enable us to observe the structural evolution of graphite as discussed in the Introduction. In a recent study, employing the same graphite oxidation procedure, by Dimiev and Tour [55], it was shown that graphite oxidized in three consecutive steps. Upon addition of a small amount of $KMnO_4$ (mass ratio graphite:$KMnO_4$=1:1), the first stage sulphuric acid-GIC was formed. With further addition of oxidant, its molecules diffused into the interlayer spacing between graphene sheets, reacted with acid yielding strong oxidizing species that initiate the production of pristine graphite oxide (PGO). After the addition of 4 weight equivalents of $KMnO_4$, the authors observed a very sharp and strong XRD peak at 2θ=9.7° (q=0.7 $Å^{-1}$), which led them to propose that the stacking order of the graphene sheets during the oxidation process was preserved, and only expansion along graphite's c-axis ([002] reflection) occurred. The authors argued that H_2SO_4 molecules remained intercalated in between the galleries in PGO, and that the structure was stable as long as it was not exposed to large amounts of water. Quenching the reaction mixture with H_2O during the oxidation procedure lead to exfoliated PGO sheets and subsequently restacked GO sheets did no longer possess long range order along the c-axis, thus giving a much weaker XRD signal. In addition, the interlayer spacing in restacked graphite oxide (CGO) was slightly reduced. Finally, based on Raman spectroscopy and optical microscopy results, the authors observed that the formation of sulfuric acid-GIC took 5 minutes only, whereas the formation of graphite oxide takes hours. The XRD results of this study are summarized in Figure 2.6 (A) and Table 2.5, and contrasted to our experimental evidence presented in Figure 2.6 (B). It is,

however, important to mention that the authors in this study prepared the samples for XRD diffraction by taking a small amount of sample from the reaction mixture at certain times into the oxidation process, centrifuging it for 30 min, discarding supernatant, and wrapping the wet powder sample in plastic.

TABLE 2.5. Characteristic peak positions observed by Dimiev and Tour [55]. Acronyms (vs) and (s) stand for very strong and strong scattering peaks, respectively.

Sample name	*Mass ratio of Gr: $KMnO_4$*	*Characteristic peak positions*	
		2θ, °	*q, $Å^{-1}$*
Stage-1 GIC	1:1	22.3 (vs) 33.7 (s) 45.2 (s)	1.6 2.4 3.1
TF-1 & TF-2	1:1 1:2	11.4 (s) 21.6 (s) 22.3 (s) 33.7 (s)	0.8 1.5 1.6 2.4
TF-3 & TF-4	1:3 1:4	9.7 (vs)	0.7
CGO	–	11.0 (s)	0.8

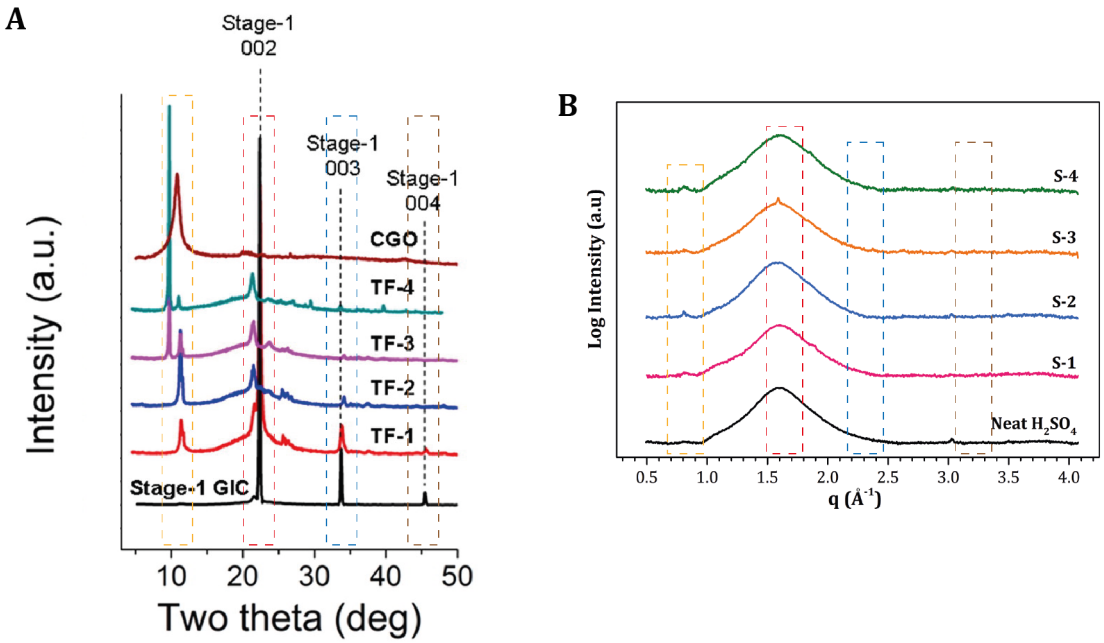

FIGURE 2.6. (A) X-ray diffraction patterns of graphite powder samples with different amounts of $KMnO_4$ added to the reaction mixture (adapted from [55]). TF-1, TF-2, TF-3 and TF-4 stand for the

weight equivalent of $KMnO_4$ to graphite (see Table 2.5), stage-1 GIC – sulfuric acid-GIC, CGO-restacked graphite oxide. (B) X-ray diffraction patterns of graphite samples with different amounts of $KMnO_4$ obtained by probing samples *in situ* after 5-15 minutes after preparation. S-1, S-2, S-3 and S-4 stand for the weight equivalent of $KMnO_4$ to graphite as described in the experimental part. The colored dotted lines draw attention and compare the most significant positions in the diffractograms.

Our X-ray diffraction patterns, presented in Figure 2.6 (B) however, reveal a different picture. We do not observe the evolution of a graphite structure, only a broad peak at 1.6 A^{-1} that corresponds to the distance of 3.9 Å between the adjacent sulphuric acid molecules – the so called liquid ring – and the distance is comparable to the value reported in the literature [56]. In a recent study Kovtyukhova et al. [38] reported that sulfuric acid-GIC does not produce the characteristic diffraction pattern as observed by Dimiev and Tour so long as the compound remains in liquid. Consequently, they arrived at the conclusion that the non-oxidative intercalation of sulfuric acid molecules can only occur when the hydrogen bonding network between the acid molecules is disrupted, either by heating or evaporation, since only then the acid molecules are able to initiate the inter-layer opening of graphene sheets in graphite. However, the weak and broad characteristic graphite peak ([002] reflection) at 1.9 $Å^{-1}$ observed in the Gr/H_2SO_4 mixture in our experiments suggests that sulphuric acid molecules can presumably partially intercalate in between graphene sheets in a random fashion thus disrupting the regular stacking of graphene sheets in graphite, see Figure 2.7 for a schematic illustration.

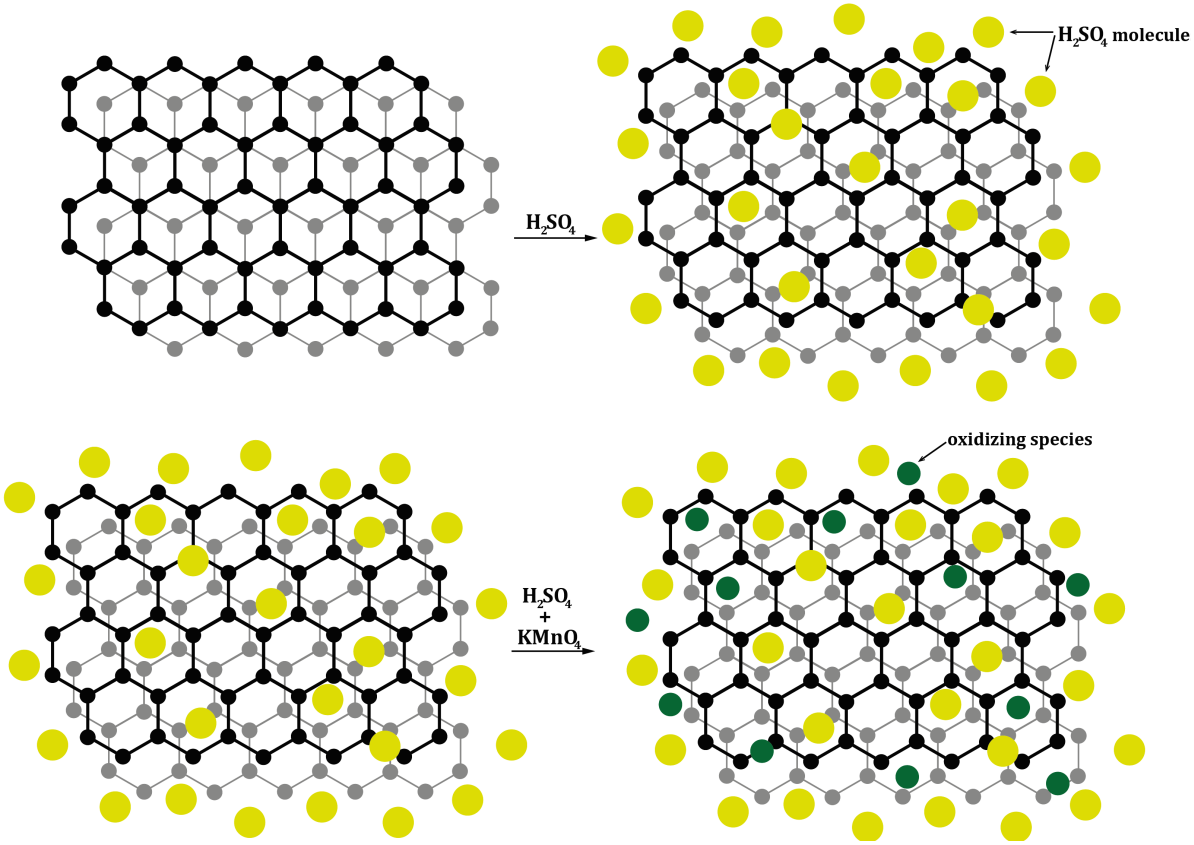

FIGURE 2.7. Schematic illustration of the graphite oxidation mechanism. Big dark yellow circles represent sulfuric acid molecules whereas smaller dark green circles – oxidizing species that form upon the reactions between sulfuric acid and Potassium permanganate.

This result is in agreement with the observed lowest intercalation efficiency of sulfuric acid by Kovtyukhova and co-authors [38]. When $KMnO_4$ is added, the characteristic graphite peak diminishes and/or disappears altogether It is, however, unlikely that graphite fully exfoliated into graphene sheets in the experimental procedure applied here, as this process requires high-energy input and/or time. As illustrated in Figure 2.5 (A), the characteristic peak of graphite 1.9 $Å^{-1}$ does not disappear for diluted H_2SO_4 solutions. This suggests that increased water content in H_2SO_4 reduces the activity of the acid molecules as they favour interactions with water molecules, and as a result the graphite-H_2SO_4 interactions are significantly reduced. On the other hand, the significant reduction of the graphite characteristic peak in concentrated sulfuric acid suggests that graphene-graphene interactions are apparently weaker compared to graphene-acid interactions. As discussed

earlier, the experimental studies by Coleman and co-workers led to suggest that the solvents, which have surface energies around 70 mJ m^{-2} are highly suitable for stable and relatively concentrated graphene dispersions. However, the matching surface energies may not be sufficient to guarantee a homogenous dispersion of graphene if the interfacial tension between sheets and solvent molecules is not minimized as well [57]. Now, the surface energy of sulfuric acid [58] is around the same value as that of the solvents yielding most concentrated graphene dispersions. Using a simple expression [59], the interfacial energy between two components can be estimated as follows :

$$\gamma_{H_2SO_4-Gr} = \left(\sqrt{\gamma_{H_2SO_4}} - \sqrt{\gamma_{Gr}}\right)^2 \qquad (2.2)$$

Since the surface energies of graphene and sulfuric acid are comparable, the interfacial energy between these two components is, indeed, negligible. In fact, the interfacial energy between graphite and acid is also small, assuming the surface energy value of graphite to be 52.1 mJ m^{-2} [60]. This suggests, that concentrated sulfuric acid may be a suitable solvent for solvent-assisted graphene preparation as the van der Waals forces between the adjacent graphene sheets can be fully overcome.

Dried 1st stage sulphuric acid-GIC and PGO compounds exhibit strong and well-defined peaks, see the diffractograms in the original article [55], that are not observed in our experiments upon addition of $KMnO_4$. The absence of oxidant reflections in Figure 2.4 (B-D) indicates its reaction with concentrated H_2SO_4 that produces the oil-like, green-colored strongly oxidizing substance Mn_2O_7 [61], also observed in the reaction vial upon mixing, as well as other oxidizing species [62]. The newly developed species presumably oxidizes graphene sheets in a similar manner as proposed by Dimiev and Tour, however the 1st stage sulphuric acid-GIC and PGO structures are more likely to remain invisible in XRD due to the yet not defined interaction between sulfuric acid molecules and graphene sheets in graphite.

As for the weaker diffraction peak at 0.8 $Å^{-1}$ it is likely to correspond to the spacing between the second layer of sulphuric acid molecules. However, upon addition of $KMnO_4$, the intensity of the peak at 0.8 $Å^{-1}$ slightly increases, which could indicate the presence graphite oxide.

2.7. Conclusions

Our X-ray diffractometry results appear to indicate that during the graphite oxidation process using concentrated sulfuric acid and Potassium permanganate no strong crystalline order, unique to the sulfuric acid-graphite intercalation compounds and/or graphite oxide, develops if they remain in concentrated acid. This suggests that the formation of sulfuric acid-graphite intercalation compounds as well as graphite oxide cannot be excluded, but it is certain that they are not sufficiently ordered to yield the required characteristic diffraction peaks. Similarly, depending on the concentration of acid, the graphene-graphene interactions in graphite also appear to be significantly weakened by the sulfuric acid molecules, hence concentrated sulfuric acid may be a good solvent for graphene dispersions, provided there is sufficient energy input to separate the layers of graphene. However, upon removing the excess of acid, order does develop as demonstrated elsewhere.

Acknowledgements

We thank Nico Alberts for designing and building the sample holder for the X-ray diffraction measurements, and appreciate help of Kees Goubitz in collecting X-ray diffractograms. We also thank dr.ir. M.Makkee for reviewing parts of this Chapter.

2.8. References

1. Novoselov, K. S.; Geim, A. K.; Morozov, S. V.; Jiang, D.; Zhang, Y.; Dubonos, S. V.; Grigorieva, I. V.; Firsov, A. A. *Science* **2004,** *306* (5696), 666-669.

2. Lee, C.; Wei, X. D.; Kysar, J. W.; Hone, J. *Science* **2008,** *321* (5887), 385-388.

3. Bunch, J. S.; Verbridge, S. S.; Alden, J. S.; van der Zande, A. M.; Parpia, J. M.; Craighead, H. G.; McEuen, P. L. *Nano Lett* **2008,** *8* (8), 2458-2462.

4. Du, X.; Skachko, I.; Barker, A.; Andrei, E. Y. *Nat Nanotechnol* **2008,** *3* (8), 491-495.

5. Balandin, A. A.; Ghosh, S.; Bao, W. Z.; Calizo, I.; Teweldebrhan, D.; Miao, F.; Lau, C. N. *Nano Lett* **2008,** *8* (3), 902-907.

6. Huang, X.; Qi, X. Y.; Boey, F.; Zhang, H. *Chem Soc Rev* **2012,** *41* (2), 666-686.

7. Bai, S.; Shen, X. P. *Rsc Adv* **2012,** *2* (1), 64-98.

8. Liu, Y. X.; Dong, X. C.; Chen, P. *Chem Soc Rev* **2012,** *41* (6), 2283-2307.

9. Zhang, N.; Zhang, Y. H.; Xu, Y. J. *Nanoscale* **2012,** *4* (19), 5792-5813.

10. Huang, X.; Zeng, Z. Y.; Fan, Z. X.; Liu, J. Q.; Zhang, H. *Adv Mater* **2012,** *24* (45), 5979-6004.

11. Machado, B. F.; Serp, P. *Catal Sci Technol* **2012,** *2* (1), 54-75.

12. Chung, C.; Kim, Y. K.; Shin, D.; Ryoo, S. R.; Hong, B. H.; Min, D. H. *Accounts Chem Res* **2013,** *46* (10), 2211-2224.

13. Weiss, N. O.; Zhou, H. L.; Liao, L.; Liu, Y.; Jiang, S.; Huang, Y.; Duan, X. F. *Adv Mater* **2012,** *24* (43), 5782-5825.

14. Novoselov, K. S.; Fal'ko, V. I.; Colombo, L.; Gellert, P. R.; Schwab, M. G.; Kim, K. *Nature* **2012,** *490* (7419), 192-200.

15. (a) Somani, P. R.; Somani, S. P.; Umeno, M. *Chem Phys Lett* **2006,** *430* (1-3), 56-59; (b) Seah, C. M.; Chai, S. P.; Mohamed, A. R. *Carbon* **2014,** *70*, 1-21.

16. (a) Hernandez, Y.; Nicolosi, V.; Lotya, M.; Blighe, F. M.; Sun, Z. Y.; De, S.; McGovern, I. T.; Holland, B.; Byrne, M.; Gun'ko, Y. K.; Boland, J. J.; Niraj, P.; Duesberg, G.; Krishnamurthy, S.; Goodhue, R.; Hutchison, J.; Scardaci, V.; Ferrari, A. C.; Coleman, J. N. *Nat Nanotechnol* **2008,** *3* (9), 563-568; (b) Ciesielski, A.; Samori, P. *Chem Soc Rev* **2014,** *43* (1), 381-398.

17. (a) Wu, J. S.; Pisula, W.; Mullen, K. *Chem Rev* **2007,** *107* (3), 718-747; (b) Cai, J. M.; Ruffieux, P.; Jaafar, R.; Bieri, M.; Braun, T.; Blankenburg, S.; Muoth, M.; Seitsonen, A. P.; Saleh, M.; Feng, X. L.; Mullen, K.; Fasel, R. *Nature* **2010,** *466* (7305), 470-473.

18. (a) Brodie, B. C. *Phil. Trans. R. Soc. Lond.* **1859,** *149*, 249-259; (b) Staudenmaier, L. *Berichte der deutschen chemischen Gesellschaft* **1898,** *31*, 1481–1487; (c) Hofmann, U.; Konig, E. *Z Anorg Allg Chem* **1937,** *234* (4), 311-336; (d) Hummers, W. S.; Offeman, R. E. *J Am Chem Soc* **1958,** *80* (6), 1339-1339.

19. Li, Y.; Chopra *Journal of the Minerals, Metals and Materials Society* **2014,** *67* (1), 34-52.

20. Gao, W.; Alemany, L. B.; Ci, L. J.; Ajayan, P. M. *Nat Chem* **2009,** *1* (5), 403-408.

21. Paredes, J. I.; Villar-Rodil, S.; Martinez-Alonso, A.; Tascon, J. M. D. *Langmuir* **2008,** *24* (19), 10560-10564.

22. Kuila, T.; Bose, S.; Mishra, A. K.; Khanra, P.; Kim, N. H.; Lee, J. H. *Prog Mater Sci* **2012,** *57* (7), 1061-1105.

23. Stankovich, S.; Dikin, D. A.; Piner, R. D.; Kohlhaas, K. A.; Kleinhammes, A.; Jia, Y.; Wu, Y.; Nguyen, S. T.; Ruoff, R. S. *Carbon* **2007,** *45* (7), 1558-1565.

24. Dreyer, D. R.; Park, S.; Bielawski, C. W.; Ruoff, R. S. *Chem Soc Rev* **2010,** *39* (1), 228-240.

25. Du, W. C.; Jiang, X. Q.; Zhu, L. H. *J Mater Chem A* **2013,** *1* (36), 10592-10606.

26. Khan, U.; O'Neill, A.; Lotya, M.; De, S.; Coleman, J. N. *Small* **2010,** *6* (7), 864-871.

27. Hernandez, Y.; Lotya, M.; Rickard, D.; Bergin, S. D.; Coleman, J. N. *Langmuir* **2010,** *26* (5), 3208-3213.

28. Paton, K. R.; Varrla, E.; Backes, C.; Smith, R. J.; Khan, U.; O'Neill, A.; Boland, C.; Lotya, M.; Istrate, O. M.; King, P.; Higgins, T.; Barwich, S.; May, P.; Puczkarski, P.; Ahmed, I.; Moebius, M.; Pettersson, H.; Long, E.; Coelho, J.; O'Brien, S. E.; McGuire, E. K.; Sanchez, B. M.; Duesberg, G. S.; McEvoy, N.; Pennycook, T. J.; Downing, C.; Crossley, A.; Nicolosi, V.; Coleman, J. N. *Nat Mater* **2014,** *13* (6), 624-630.

29. Coleman, J. N. *Accounts Chem Res* **2013,** *46* (1), 14-22.

30. Choi, E. Y.; Choi, W. S.; Lee, Y. B.; Noh, Y. Y. *Nanotechnology* **2011,** *22* (36).

31. O'neill, A.; Khan, U.; Nirmalraj, P. N.; Boland, J.; Coleman, J. N. *J Phys Chem C* **2011,** *115* (13), 5422-5428.

32. Qian, W.; Hao, R.; Hou, Y. L.; Tian, Y.; Shen, C. M.; Gao, H. J.; Liang, X. L. *Nano Res* **2009,** *2* (9), 706-712.

33. Zhang, X. Y.; Coleman, A. C.; Katsonis, N.; Browne, W. R.; van Wees, B. J.; Feringa, B. L. *Chem Commun* **2010,** *46* (40), 7539-7541.

34. (a) Lotya, M.; Hernandez, Y.; King, P. J.; Smith, R. J.; Nicolosi, V.; Karlsson, L. S.; Blighe, F. M.; De, S.; Wang, Z. M.; McGovern, I. T.; Duesberg, G. S.; Coleman, J. N. *J Am Chem Soc* **2009,** *131* (10), 3611-3620; (b) Lotya, M.; King, P. J.; Khan, U.; De, S.; Coleman, J. N. *Acs Nano* **2010,** *4* (6), 3155-3162; (c) Guardia, L.; Fernandez-Merino, M. J.; Paredes, J. I.; Solis-Fernandez, P.; Villar-Rodil, S.; Martinez-Alonso, A.; Tascon, J. M. D. *Carbon* **2011,** *49* (5), 1653-1662.

35. (a) Bourlinos, A. B.; Georgakilas, V.; Zboril, R.; Steriotis, T. A.; Stubos, A. K.; Trapalis, C. *Solid State Commun* **2009,** *149* (47-48), 2172-2176; (b) May, P.; Khan, U.; Hughes, J. M.; Coleman, J. N. *J Phys Chem C* **2012,** *116* (45), 24390-24391.

36. (a) Zhang, M.; Parajuli, R. R.; Mastrogiovanni, D.; Dai, B.; Lo, P.; Cheung, W.; Brukh, R.; Chiu, P. L.; Zhou, T.; Liu, Z. F.; Garfunkel, E.; He, H. X. *Small* **2010,** *6* (10), 1100-1107; (b) Parviz, D.; Das, S.; Ahmed, H. S. T.; Irin, F.; Bhattacharia, S.; Green, M. J. *Acs Nano* **2012,** *6* (10), 8857-8867.

37. Ebert, L. B. *Annu Rev Mater Sci* **1976,** *6*, 181-211.

38. Kovtyukhova, N. I.; Wang, Y. X.; Berkdemir, A.; Cruz-Silva, R.; Terrones, M.; Crespi, V. H.; Mallouk, T. E. *Nat Chem* **2014,** *6* (11), 957-963.

39. Moissette, A.; Fuzellier, H.; Burneau, A.; Dubessy, J.; Guérard, D.; Lelaurain, M. *Materials Science Forum* **1992,** *91-93*, 95-99.

40. Mckelvy, M. J.; Glaunsinger, W. S. *Annu Rev Phys Chem* **1990,** *41*, 497-523.

41. Hofmann, U.; Rudorff, W. *T Faraday Soc* **1938,** *34* (2), 1017-1021.

42. Leung, S. Y.; Dresselhaus, M. S.; Underhill, C.; Krapchev, T.; Dresselhaus, G.; Wuensch, B. J. *Phys Rev B* **1981,** *24* (6), 3505-3518.

43. Bragg, W. H.; Bragg, W. L. *P R Soc Lond a-Conta* **1913,** *88* (605), 428-438.

44. Dresselhaus, M. S.; Dresselhaus, G. *Adv Phys* **1981,** *30* (2), 139-326.

45. Metrot, A.; Tihli, M. *Synthetic Met* **1985,** *12* (1-2), 517-523.

46. (a) Forsman, W. C.; Dziemianowicz, T.; Leong, K.; Carl, D. *Synthetic Met* **1983,** *5* (2), 77-100; (b) Inagaki, M.; Iwashita, N.; Kouno, E. *Carbon* **1990,** *28* (1), 49-55; (c) Moissette, A.; Fuzellier, H.; Burneau, A.; Dubessy, J.; Lelaurain, M. *Carbon* **1995,** *33* (2), 123-128; (d) Kang, F. Y.; Zhang, T. Y.; Leng, Y. *J Phys Chem Solids* **1996,** *57* (6-8), 883-888.

47. Yosida, Y.; Tanuma, S. *Synthetic Met* **1989,** *34*, 341-346.

48. (a) Su, C. Y.; Lu, A. Y.; Xu, Y. P.; Chen, F. R.; Khlobystov, A. N.; Li, L. J. *Acs Nano* **2011,** *5* (3), 2332-2339; (b) Parvez, K.; Li, R. J.; Puniredd, S. R.; Hernandez, Y.; Hinkel, F.; Wang, S. H.; Feng, X. L.; Mullen, K. *Acs Nano* **2013,** *7* (4), 3598-3606.

49. Kovtyukhova, N. I.; Ollivier, P. J.; Martin, B. R.; Mallouk, T. E.; Chizhik, S. A.; Buzaneva, E. V.; Gorchinskiy, A. D. *Chem Mater* **1999,** *11* (3), 771-778.

50. Marcano, D. C.; Kosynkin, D. V.; Berlin, J. M.; Sinitskii, A.; Sun, Z. Z.; Slesarev, A.; Alemany, L. B.; Lu, W.; Tour, J. M. *Acs Nano* **2010,** *4* (8), 4806-4814.

51. (a) Mermoux, M.; Chabre, Y. *Synthetic Met* **1990,** *34* (1-3), 157-162; (b) Nakajima, T.; Matsuo, Y. *Carbon* **1994,** *32* (3), 469-475; (c) N. E. Sorokina, M. A. K., V. V. Avdeev, and I. V. Nikol'skaya *Russian Journal of General Chemistry* **2005,** *75* (2), 162-168.

52. Lipson, H.; Stokes, A. *Proceedings of the Royal Society of London* **1942,** *181*, 101-105.

53. Mooney, R. C. L. *Physical Review* **1931,** *37*, 1306-1310.

54. Wu, C. G.; Chiang, C. H. *Crystengcomm* **2011,** *13* (5), 1406-1409.

55. Dimiev, A. M.; Tour, J. M. *Acs Nano* **2014,** *8* (3), 3060-3068.

56. Krishnan, R. S. *Proc. Indian Acad. Sci. A* **1937,** *4*, 661.

57. Texter, J. *Curr Opin Colloid In* **2014,** *19* (2), 163-174.

58. Lyklema, J. *Colloid Surface A* **1999,** *156* (1-3), 413-421.

59. Israelachvili, J. N., *Intermolecular and Surface Forces*. 3rd ed.; Academic Press: 2011; p 704.

60. Perez-Mendoza, M.; Almazan-Almazan, M. C.; Mendez-Linan, L.; Domingo-Garcia, M.; Lopez-Garzon, F. J. *J Chromatogr A* **2008,** *1214* (1-2), 121-127.

61. Tromel, M.; Russ, M. *Angew Chem Int Edit* **1987,** *26* (10), 1007-1009.

62. Royer, D. J. *J Inorg Nucl Chem* **1961,** *17* (1-2), 159-167.

CHAPTER 3

TUNABLE ORDER IN ALGINATE/GRAPHENE BIOPOLYMER NANOCOMPOSITES

This chapter has been published as:

Vilcinskas, K., Norder, B., Goubitz, K., Mulder, F.M., Koper, G.J.M., Picken, S.J., *Tunable Order in Alginate/Graphene Biopolymer Nanocomposites*. Macromolecules, 2015, **48**(22): p. 8323-8330.

ABSTRACT

We report on highly aligned or compromised order of (reduced) graphene oxide sheets inside an alginate matrix and their microstructure obtained for various compositions. The order of the platelet particles with respect to one another is verified by environmental scanning microscopy (ESEM) and 2-Dimensional X-ray Diffraction (2D XRD). The microscopic order within the platelet particles has been analyzed by X-ray diffraction (XRD) measurements in the Bragg-Brentano reflection configuration as well as in Debye-Scherrer diffraction mode. The azimuthal angle intensity profiles obtained from 2D XRD analysis have been fit to Maier-Saupe and Affine Deformation Model predictions, and the Affine Deformation Model proved to be the most reliable to quantify the order parameter $\langle P_2 \rangle$ values of Sodium alginate-graphene oxide and Calcium alginate-reduced graphene oxide composites with different weight fractions of the filler. The $\langle P_2 \rangle$ values for Sodium alginate-graphene oxide composites are found to show little dependence on the concentration of graphene oxide sheets above about 10 wt%, with a maximum $\langle P_2 \rangle$ value of 0.8 at 25 wt% of graphene oxide inside the Sodium alginate matrix. The alignment of reduced graphene oxide sheets inside the Calcium alginate matrix is observed to be lower, with an average $\langle P_2 \rangle$ value of 0.7. We do not observe orientation of reduced graphene oxide sheets inside the Barium alginate matrix. The formation of a highly aligned Sodium alginate-graphene oxide composite structure has been explained by the Affine Deformation Model, whereupon drying the developed yield stress causes sheets to align in-plane with the polymer matrix. The impaired orientation of reduced graphene oxide sheets inside the Calcium alginate matrix and absence of orientation in the Barium alginate matrix have been explained by the structure development in the polymer matrix itself due to metal-ion induced cross-linking.

3.1. Introduction to alginate-graphene composites

It has been widely reported that inclusion of graphene into polymer matrices yields composite materials with improved mechanical [1], thermal [1b, 2], electrical [3], and gas barrier properties [4]. However, the hydrophobic nature of graphene, its poor dispersibility in many of the commonly used solvents and its consequent propensity to aggregate readily, hampers preparation of graphene-polymer composites with optimal properties. In order to facilitate processability and good dispersion of the sheets, graphene oxide (GO) is often used either as a filler itself or as a precursor of graphene filler [5]. The oxygenated groups on GO sheets enable dispersion in aqueous media, thus making it attractive for the preparation of composites with water-soluble polymers, such as polyvinyl alcohol [6] or chitosan [7]. The addition of GO also yields composite materials with enhanced mechanical [7-8] and gas barrier properties [6, 9].

Recently, several studies [10] reported on the properties of GO-Sodium alginate composites. Alginates are naturally occurring copolymers that have been renowned for their gelling properties with multivalent metal ions [11], and have been widely utilized in food industry and for medical applications [12]. Amongst the reported properties of Sodium alginate-GO composites, some authors discussed the preferential alignment of GO sheets within the polymer matrix and the unusual changes in morphology upon inclusion of the sheets. However, they did not make an attempt to quantify the degree of orientation of the sheets nor interpret its origin.

In this study, we aim to explore the nature of the alignment of (reduced) graphene oxide sheets within an alginate matrix and assess the orientation quantitatively as a function of weight fraction of sheets within the polymer matrix. We also investigate how an alkaline earth metal ion influences the morphology of alginate and subsequently its composites of various weight fractions of reduced graphene oxide sheets with regard to their degree of order.

3.2. Experimental section

3.2.1. Sample preparation

Sodium alginate salt (Protanal® RF 6650, high molecular weight, mannuronic to guluronic acid ratio about 1.0:1.5 as indicated by the supplier) was kindly provided by FMC Biopolymer. To prepare 1 wt% aqueous polymer solution, 1 gram of Sodium alginate salt (Na-Alg) was dissolved in 99 grams demineralized water, containing 0.4 grams of glycerol (99+ Pure, Acros Organics) under vigorous stirring until a homogenous solution was attained.

Graphene oxide (GO) was prepared via Kovtyiukhova's method [13]. Briefly, during the first oxidation step, 10 grams of graphite powder (Fluka) was put into a solution comprised of 15 mL concentrated H2SO4 (Sigma Aldrich), 5 grams of K2S2O8 (Sigma Aldrich), and 5 grams of P2O5 (Sigma Aldrich) at 80 °C, and left to stir for 6 h. Afterwards, the mixture was carefully diluted with distilled water, filtered, washed on the filter until the rinse water pH became neutral, and dried under vacuum at 50 °C overnight. Subsequently, 2 grams of the pre-oxidized graphite powder were put into cold (about 0°C) 46 mL concentrated sulfuric acid while stirring, and 6 grams of KMnO4 (Sigma Aldrich) in small portions were added to the mixture, keeping its temperature below 10°C. The mixture was then stirred at 35 °C for 2 h, after which 92 mL of distilled water was slowly added to the mixture. 15 minutes after, another portion of 280 mL of distilled water was added, followed by the addition of 5 mL 30% H2O2 (Sigma Aldrich) while stirring. The mixture was filtered and washed with 500 mL of 5wt% aqueous HCl (Sigma Aldrich) solution. The as-produced GO was dispersed in water by vigorous stirring, poured in a cellulose membrane (Sigma Aldrich, molecular weight cut-off 14 000) and dialised for 2.5 days. The purified GO dispersion was then sonicated for 30 min, subjected to high speed centrifugation for 20 min (centrifugation force g about 20 000), clear supernatant discarded and viscous brown fraction of GO collected. The final GO concentration in the dispersion was determined by measuring the dry mass of 5 GO samples after evaporation at 100 °C.

Composite films with various weight fractions of GO were prepared by drop-wise addition of aqueous GO dispersion into a 1 wt% Na-Alg solution and continuous stirring until a homogenous mixture was attained (about 2 hours). The mixture then was poured into a Petri dish and dried under vacuum at 50 °C overnight (about 15 hours).

Subsequently, the thus obtained free-standing water-soluble Na-Alg/GO composite films of ~30 µm in thickness were cut into strips of about 30x3 mm^2 and immersed into a 5 wt% $CaCl_2$ (Sigma Aldrich) or a 5 wt% $BaCl_2 \cdot 2H_2O$ (Riedel-de Haën) solution for 20 min to obtain alkaline earth metal cross-linked alginate composite films. The excess salt was removed using copious amounts of demineralized water. The samples were dried under vacuum at 50 °C. Note that, without the cross-linking salt, the Na-Alg/GO films readily dissolve in water since they are hydrophilic, whereas the cross-linked films are water-insoluble and form a swollen gel.

Finally, the reduced graphene oxide (rGO)/alginate composite films were prepared by immersing the water-insoluble alkaline earth metal cross-linked alginate/GO composite films, as described above, into an aqueous hydrazine (Sigma Aldrich) solution for 48 h at ambient temperature. The weight ratio of GO to hydrazine was about 10:7. During the course of reduction, the composite films changed their color appreciably, from dark brown to black. Hydrazine is not known to affect the alginate, therefore the color change indicates the reduction of GO. After reduction, the composite films were washed with copious amounts of demineralized water, dried under vacuum at 50 °C and stored in the desiccator with silica gel as the drying agent. Prior to further analysis, the samples were kept in the furnace at 50 °C under vacuum for at least 48 h.

A couple of separate Na-Alg/GO mixture samples were disturbed after 3h and 7h of the drying process by stirring them with a spatula for about 30 seconds and subsequently leaving them to dry the rest of the night (about 12 or 8 h).

3.2.2. Characterization

The cross-sectional images and electron microprobe images of the samples were collected by Environmental Scanning Electron Microscopy (ESEM) using a Philips XL30 Series ESEM. Prior to imaging, the samples were coated with graphite using a Leica EM CED030 sputter coating.

X-ray diffraction (XRD) measurements in Bragg-Brentano reflection mode were performed by a PANalytical X'Pert Pro PW3040/60 diffractometer with Cu Kα radiation operating at 45kV and 40 mA in an angular 2θ range of 5-50 ˚.

2-Dimensional X-ray Diffraction (2D XRD) measurements were carried out using a Bruker D8 Discover X-ray diffractometer with a Hi-Star 2D detector and with Cu Kα radiation filtered by cross-coupled Göbel mirrors operated at 40kV and 40mA. The distance between the samples and the detector was maintained at 6 cm and 13 cm for perpendicular and parallel directions to the sample plane, respectively.

Atomic force microscopy (NTMDT Ntegra) (AFM) was used to observe the morphology of graphene oxide sheets. For analysis, 0.05wt% graphene oxide aqueous dispersion was spin-coated on a clean silicon wafer (Siltronix) and examined in tapping mode.

Figure 3.1 (A) depicts a typical AFM image of the obtained GO sheets. The thickness, measured from the height profile of the AFM image, Figure 3.1 (B), shows that the average thickness of the sheets is about 1.0 nm, which indicates the formation of single-layered exfoliated GO [14]. The lateral dimensions of the sheets vary from sheet to sheet, however, the average length/width ratio – hence aspect ratio – is considered to be high.

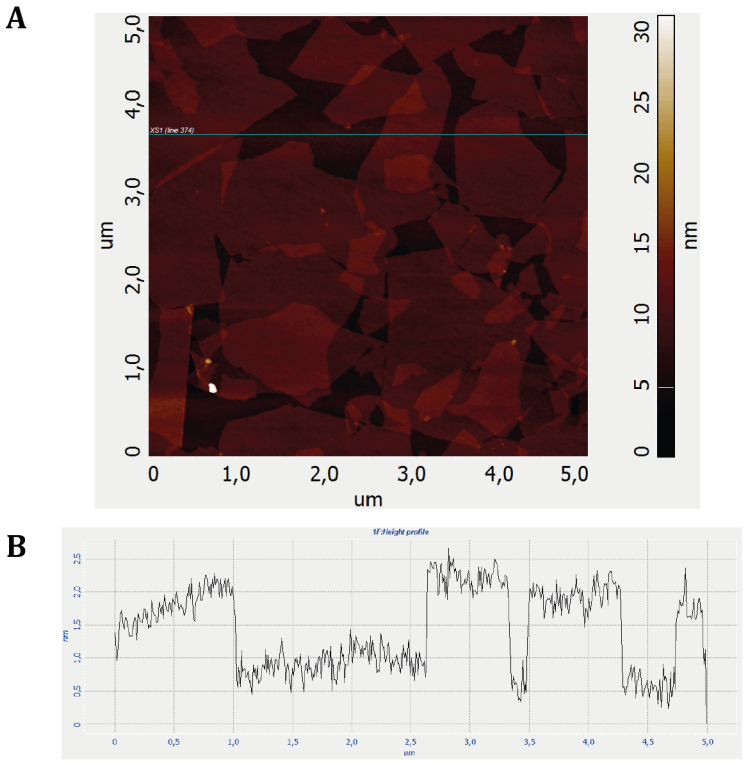

FIGURE 3.1. Tapping mode AFM image (A) of graphene oxide sheets on a silica substrate and the height profile (B) corresponding to the line in the AFM image

3.3. Results

3.3.1. Orientation

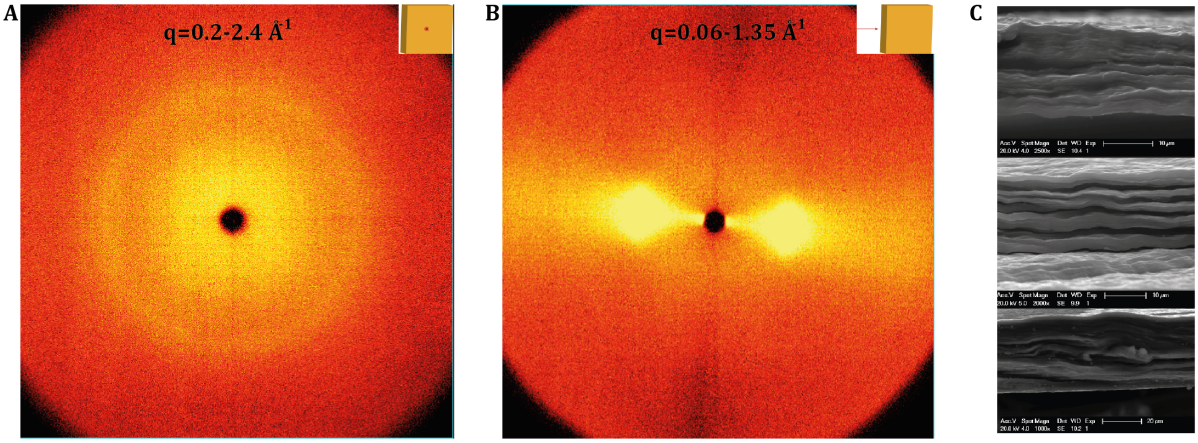

FIGURE 3.2. Representative 2D XRD images of Sodium alginate/25wt% GO samples with the X-ray beam (inset) along (A) (q=0.19-2.42 Å^{-1}) and almost perpendicular (B) (q=0.06-1.35 Å^{-1}) to the layer

normal. Graph (C) shows cross-sectional ESEM images of Sodium alginate/25wt% GO (top, scale bar 10 μm) Calcium alginate/25wt% rGO (middle, scale bar 10 μm), and Barium alginate/25 wt% rGO (bottom, scale bar 20 μm).

Figure 3.2 (A)-(B) show 2D XRD patterns of the Na-Alg/25 wt% GO composite sample analyzed along (Figure 3.2 A) and almost perpendicular (Figure 3.2 B) to the layer normal where the latter reveals the ordering of the platelet particles with respect to one another inside the polymer matrix. The diffusive scattering ring around the layer normal reveals isotropic scattering, which originates from the GO sheets that are randomly positioned in the plane of the film. In contrast, the scattering pattern almost perpendicular to the layer normal demonstrates intense equatorial scattering, indicating preferential alignment of the sheets in the polymer matrix. The ESEM micrographs presented in Figure 3.2 (C) confirm the in-plane orientation of sheets inside a polymer matrix.

Recently, highly ordered Sodium alginate/montmorillonite samples have been obtained by a similar procedure as reported here [15]. These authors have explained the formation of the highly ordered composite by the creation of a network between the negatively charged alginate backbone and the positively charged Montmorillonite edges. Upon drying these samples, a yield stress develops that causes the clay platelets to align. We suggest that the same mechanism is responsible for the alignment of GO sheets although the interactions between the oxygenated GO groups and the polymer backbones are of a different nature. These interactions have been studied recently by Chen et al [10d] that analyzed Na-Alg/GO composite paper by means of Fourier Transform Infrared Spectroscopy (FTIR) and X-ray Photoelectron Spectroscopy (XPS). They concluded that the widely abundant hydroxyl groups of the Sodium alginate chains interact with the carbonyl and/or the epoxy groups that are present on GO sheets by forming hydrogen bonding networks. We will discuss the mechanism of the alignment of GO sheets further in the Discussion section.

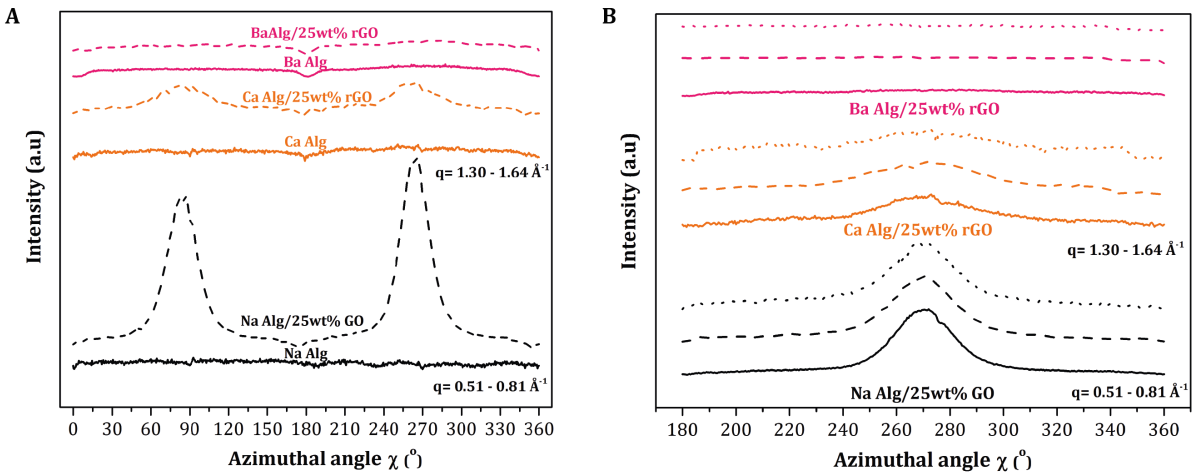

FIGURE 3.3. (A) Azimuthal angle χ plots for the samples with the X-ray beam parallel to the sample plane: Na-Alg (black solid line), Na-Alg/25wt% GO (black dashed line), Ca-Alg (orange solid line), Ca-Alg/25wt% rGO (orange dashed line), Ba-Alg (pink solid line), Ba-Alg/25wt% rGO (pink dashed line). (B) Azimuthal angle χ plots for the samples with the X-ray beam parallel to the sample plane. The solid lines represent the undisturbed samples, the dashed – disturbed after 3 hours into the drying process, the dotted – disturbed after 7 hours into the drying process.

Figure 3.3 (A) illustrates the dependence of the X-ray scattering intensity (q = 0.51-0.81 $Å^{-1}$) on azimuthal angle with parallel incidence to the film plane for the samples containing either no (r)GO filler or 25wt% filler. For all the samples we observed isotropic scattering upon incidence perpendicular to the plane as illustrated in Figure 3.2 (A) indicating no significant alignment, whereas the scattering intensity with incidence parallel to the sample plane varies with the amount of the filler. As can be seen in Figure 3.3 (A), neither Sodium alginate nor Calcium or Barium alginate polymer chains show preferential in-plane alignment. In contrast, the Na-Alg/25wt% GO composite film exhibited two distinct peaks at χ = 90° and χ = 270°. The scattering intensity of Ca-Alg/25 wt% rGO composite sample is similar albeit reduced, and the two distinct peaks are broadened despite the fact that reduced graphene oxide sheets are aligned in the Calcium alginate matrix. The Ba-Alg/25 wt% rGO composite reveals no significant X-ray scattering dependence on the azimuthal angle.

Figure 3.3 (B) shows the dependence of the X-ray scattering intensity on azimuthal angle for the samples containing 25 wt% filler, parallel incidence to the sample plane, that have been disturbed at different times during the drying process. The distinct peak at $\chi = 270°$ remains present for Na-Alg/25 wt% GO composite and Ca-Alg/25 wt% rGO composite samples indicating no apparent disorder of the filler sheets upon disturbance. As before, the Ba-Alg/25 wt% rGO reveals no significant X-ray scattering dependence on the azimuthal angle both for the disturbed and undisturbed systems.

3.3.2. Microscopic structure

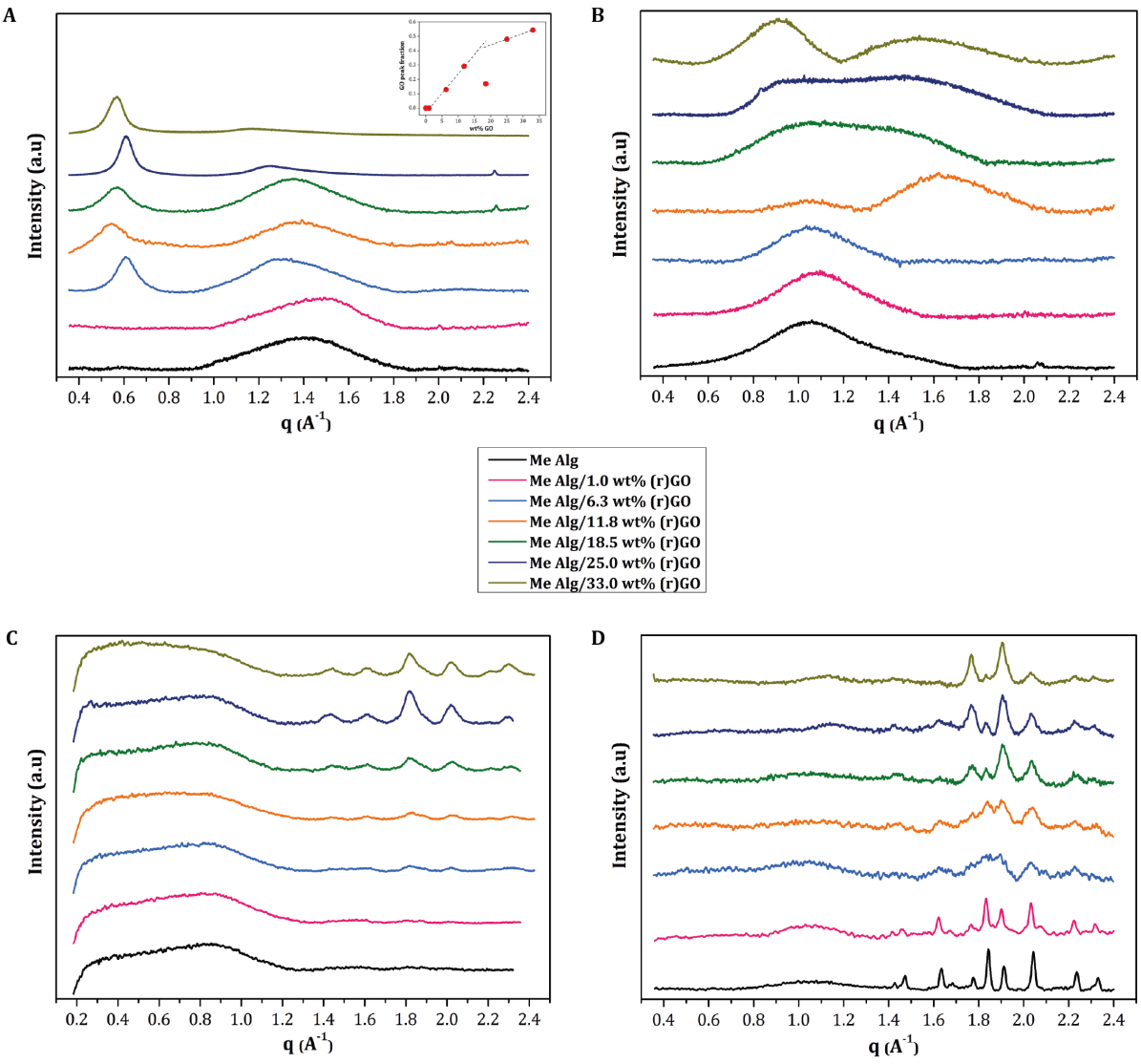

FIGURE 3.4. (A) X-ray scattering patterns of Na-Alg/GO composite films collected in the Bragg-Brentano reflection configuration. The inset spectrum represents relative fractional scattering from

GO versus the concentration of GO. (B) X-ray scattering patterns of Ca-Alg/rGO composite films collected in the Bragg-Brentano reflection configuration. (C) X-ray scattering patterns of Ba-Alg/rGO composite films with the beam along to the layer normal collected in in Debye-Scherrer diffraction mode. (D) X-ray scattering patterns of Ba-Alg/rGO composite films collected in the Bragg-Brentano reflection configuration. The spectrum of each sample has been normalized and shifted upwards.

The microscopic order of the samples of various compositions has been analyzed by XRD in the Bragg-Brentano reflection configuration and is presented in Figure 3.4 (A)-(D). Figure 3.4 (C) represents the microscopic order of the samples of various compositions collected in Debye-Scherrer diffraction mode (done on the 2D XRD instrument). As shown in Figure 3.4 (A), with increasing concentration of GO, the peak at about 0.6 $Å^{-1}$, corresponding to an interlayer spacing of approximately 11 Å between GO sheets, becomes more prominent. Using the Scherrer equation [16], the apparent width of an ordered stack of graphene oxide sheets was found to be approximately 144 Å, which yields to 13-14 sheets per stack. The absence of this peak at low weight fractions of filler indicates complete exfoliation of GO sheets [17]. The broad peak at about 1.4 $Å^{-1}$ corresponds to an amorphous structure of Sodium alginate with an average intermolecular distance between the polymer chains of 4.5 Å. This value is approximately 2 Å smaller than the value reported previously [10a, 10c]. We attribute the reduced interlayer spacing between the polymer chains to the drying process at an elevated temperature and under vacuum that enables to achieve almost water-free polymer film samples. With an increasing amount of GO, the distance between the neighboring chains increases to nearly 5.2 Å, which we attribute to the intercalation of the sheets between the polymer chains. The inset graph shows the relative fractional scattering from GO versus the content of GO. As the amount of GO in the polymer matrix increases, the relative scattering fraction from GO sheets becomes larger due the growing number of scattering centers. We have observed the initial slope of 2, which corresponds well to C/O ratio in GO, which is often reported to be 4:1-2:1 [18]. At high GO concentrations, the relative scattering fraction from GO becomes less concentration dependent presumably due to the onset of stacking of GO sheets and multiple scattering effects.

Figure 3.4 (B) represents the XRD patterns obtained in reflection mode for Calcium alginate and its rGO composite films. Upon cross-linking alginate chains with Calcium ions, the average distance between the polymer chains increased up to 6.3 Å, a similar value that has been reported previously [19]. With increasing amount of rGO, a new peak evolves at about 1.7 $Å^{-1}$, corresponding to an interlayer distance between rGO sheets of approximately 3.7 Å. As the concentration of rGO increases, two distinctive peaks merge and separate again at 33 wt% of filler. The original polymer peak shifts towards higher inter-spacing values with increasing amount of rGO, which suggests that the intercalated structure remains intact during the ion exchange reaction and subsequent reduction of the GO sheets. A small increment in the distance (up to 4 Å) between rGO sheets can be also observed with an increased concentration of the filler.

Figure 3.4 (C) shows spectra of Barium alginate and its rGO composites of various compositions spectrum measured with 2D XRD perpendicular to the plane of the samples. Here, with an increasing concentration of rGO, the peak at 1.8 $Å^{-1}$ becomes distinctively higher, and is accompanied by another set of four growing peaks at 1.4 $Å^{-1}$, 1.6 $Å^{-1}$, 2.0 $Å^{-1}$ and 2.2 $Å^{-1}$ albeit the latter less intense. This suggests that with increasing amount of rGO, an incommensurate modulated structure is formed [8], which seems to impair the alignment of the sheets as shown in Figure 3.3 (A). The system develops a central peak 1.8 $Å^{-1}$ and the satellite peaks at the above mentioned positions, corresponding to repeat distances of about 16 Å , a distance that is well compatible with the average domain size of 126 Å as obtained from the width of the 1.8 $Å^{-1}$ peak using the Scherrer formula. The peak at 2.3 $Å^{-1}$ is ascribed to the in-plane (104) graphite reflection [21]. The X-ray scattering in reflection mode presented in Figure 3.4 (D) reveals more details. Surprisingly, we could observe the semi-crystalline structure of the Barium alginate sample, containing nearly 30 wt% of glycerol. The spectrum also revealed additional peaks, which have not been observed in the 2D XRD experiment. The data collected in reflection mode corroborate the observations discussed earlier, however with some deviations. A new peak at approximately 1.9 $Å^{-1}$ becomes apparent, and the two peaks at 1.4 $Å^{-1}$ and 1.6 $Å^{-1}$ vanish for the Ba-Alg/33wt% rGO sample. Nonetheless, the peaks at 2.0 $Å^{-1}$ and 2.2

$Å^{-1}$ remain at their position, thus not entirely dismissing our assessment of the development of the incommensurately modulated structure.

Interpretation of data collected in transmission mode, Figure 3.4 (C), is somewhat involved. First of all, the information of the sample structure is almost entirely lost at the initial part of the spectrum due to the broadening of the polymer peak. Secondly, the inconsistency between data collected in transmission mode and reflection mode can be further explained by fundamental differences between the two measurement techniques and dissimilar scattering vector directions (see Supporting Information Figure 3.7.1.). First of all, due to the small film thickness compared to the penetration depth of the beam, both techniques should probe the total film. However, the path length of the incident and diffracted beam in transmission mode through polymer material is on average longer than in reflection mode, which will be responsible for the blurring of the signal obtained in transmission mode. The diffracted beam in the reflection mode is moreover refocused at the detector slits, which significantly improves the resolution. In addition, the scattering vector remains parallel to the normal for reflection mode and varies orientation for the transmission mode. This implies, that the form factor of the scattering centers varies differently for the two techniques, which might explain dissimilar intensity variations of peaks with diffraction angle.

3.3.3. Order parameter

It is well established that the azimuthal angle profile can be used to quantify the orientational order parameter $\langle P_2 \rangle$ [22]. For perfectly aligned samples $\langle P_2 \rangle = 1$, whereas for randomly oriented samples $\langle P_2 \rangle = 0$. The degree of orientation can be calculated using Maier-Saupe [23] or affine deformation [24] models for the structure of the composite. The former model is formulated on the basis of long-ranged anisotropic interactions between molecules inducing orientation in one particular direction. The latter one assumes a uniform reduction of intermolecular spacing upon overall macroscopic deformation. As discussed earlier, we surmise that the drying step induces orientation of the sheets, so the affine deformation model is expected to be the more valid. In order to verify this presumption

and compute <P_2>, we first fit our data by two distribution functions to examine, which of these yields the best fit. In the first attempt, data from intensity profiles of an azimuthal angle were fit by an intensity profile involving the Maier-Saupe (MS) distribution function [22a]

$$I(\chi) = I_b + Ae^{\alpha\cos^2(\chi)} \tag{3.1}$$

where I_b is the baseline intensity, A – a constant representing the relative scattering intensity, α – the width of the distribution, and χ – the azimuthal angle.

The same data were also fit to an intensity profile involving the affine deformation (AD) distribution function:

$$I(\chi) = I_b + A\frac{\cos^3\left[\tan^{-1}\left(\lambda\tan(\chi)\right)\right]}{\cos^3(\chi)} \tag{3.2}$$

where I_b , A and χ as previously mentioned, and λ the degree of vertical compression as described in [15].

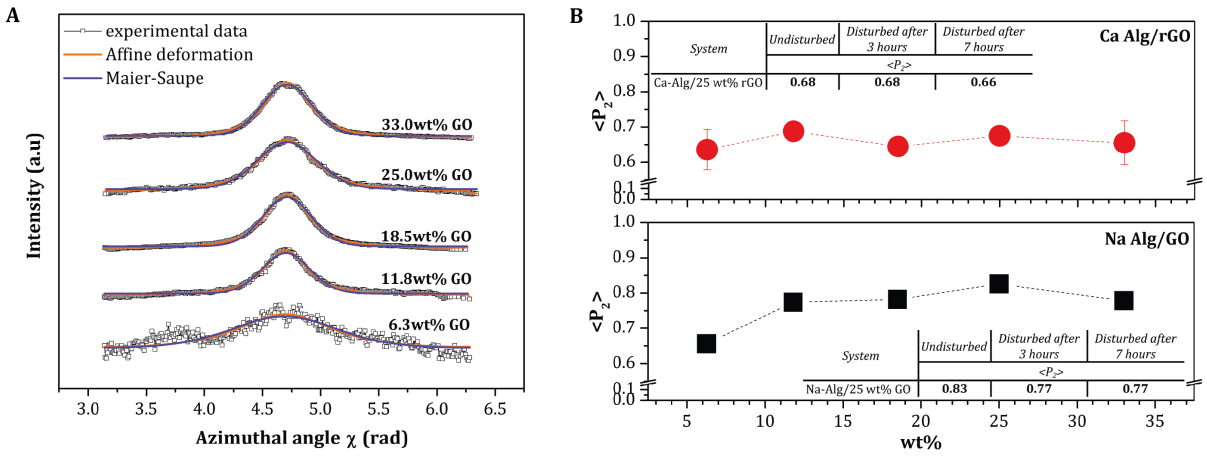

FIGURE 3.5. (A) Azimuthal angle χ (in radians) profile of the scattering intensity. The solid lines represent affine deformation (orange) and Maier-Saupe (violet) distribution function fits. (B) Order

parameter <P_2> dependence on (r)GO concentration. The inset shows the order parameter values of the systems that have been disturbed at various times during the drying process

From Figure 3.5 (A) we see that both orientation distribution functions provide good fits, albeit that the affine deformation function describes the data points slightly better, especially near the tails. Hence, the AD model was used to quantify <P_2> although the values obtained for the MS model were very similar.

From the fit values of the vertical degree of compression (λ), the order parameter <P_2> was determined using:

$$\left\langle P_2 \right\rangle = \frac{\int_{-1}^{1} P_2\left(\cos\chi\right) F\left(\chi\right) d\cos\chi}{\int_{-1}^{1} F\left(\chi\right) d\cos\chi} \tag{3.3}$$

with the second-order Legendre polynomial:

$$P_2\left(\cos\chi\right) = \frac{1}{2}\left(3\cos^2\chi - 1\right) \tag{3.4}$$

and where F(χ) is the Affine Deformation distribution function in eq.(3.2). The calculated <P_2> values are presented in Figure 3.5 (B). Remarkably, high order parameter values are achieved for the Na-Alg/GO composites, which compare favorably to values reported for GO sheets aligned under magnetic field [25]. With higher amounts of GO, the order parameter values tend to decrease presumably due to jamming effects of neighboring GO sheets. The degree of alignment of rGO sheets in Calcium alginate is inferior and appears to be less dependent of the weight fraction of the filler.

3.4. Discussion

TABLE 3.1. Characteristic properties of different alginate composites

System	*Factor*			
	<P_2>	*Structure*	*Concentration effects*	
			<P_2>	*Structure*
Na-Alg/GO	Highest	Amorphous	Varies little > 10 wt%	No
Ca-Alg/rGO	Moderate	Amorphous	Slightly decreases > 10 wt%	No
Ba-Alg/rGO	Not-observed	Semi-crystalline	−	Varying

As presented in Table 3.1., it is apparent that different types of alginate composites exhibit dissimilar properties. Though both Na-Alg/GO and Ca-Alg/rGO composites possess an amorphous structure even with increasing amount of filler, the order parameter values differ significantly. We emphasize, that the first drying step is the important step to obtain highly ordered Na-Alg/GO composites. As mentioned earlier, the interactions between carbonyl and epoxy groups present on the GO sheets and hydroxyl groups on the Sodium alginate polymer chains involve the formation of a hydrogen-bonding network. Before drying, the mixture of Sodium alginate and graphene oxide is isotropic as orientational freedom of graphene oxide sheets is not severely restricted. Upon drying, the strength of the hydrogen-bonding network between the two species increases, the mixture begins to gel and the viscosity of the mixture increases upon evaporation of water. As the drying continues, stress begins to develop in the system causing graphene oxide sheets to align in-plane. At a critical value, the critical gelation point, the system forms a rigid gel, whereupon graphene oxide sheets remain permanently locked inside the polymer matrix. The gelled polymer matrix subsequently shrinks further upon drying leading to the observed high level of alignment. The results, presented in Figure 3.3 (B), indicate a significant degree of resilience of Na-Alg/25 wt% GO system to disturbance while in the drying process. As described in the experimental procedure, a couple of separate mixture samples were disturbed after 3 hours and 7 hours during the drying process. The $<P_2>$ values of the

perturbed Na-Alg/25 wt% GO system varied a little but overall the $<P_2>$ values remained quite high ($<P_2> = 0.77$). This indicates that below the critical gelation point, the developing stress is able to reinstate the alignment of GO sheets and suggests that the transition point is rather abrupt. The $<P_2>$ values of the perturbed Ca-Alg/25 wt% rGO system showed little change, if any change at all. The perturbed Ba-Alg/25wt% rGO system revealed no changes in $<P_2>$ values. The influence of an alkali earth metal cation and the reduction reaction medium are discussed in the next paragraph.

The experimental data shows (Figure 3.5 B) that the order parameter values are not significantly affected by increasing graphene oxide concentration above about 10 wt% in the Sodium alginate matrix. However, beyond approximately 30 wt%, the order parameter value slightly decreases. We suggest that at higher weight fractions of GO, the level of exfoliation of GO sheets decreases as the sheets begin to stack. As a result of drying, the system begins to gel at a higher solids concentration, which, in turn, adversely affects ordering of the sheets.

In addition, the alignment of the sheets is also influenced by the presence of alkaline earth metal cations, in particular by their size as well as their affinity to the polymer matrix and the GO sheets. It is well known that some metal cations exhibit different affinity to the alginate matrix, such as that Barium ions have higher binding affinity to alginate than Calcium ions [11]. Furthermore, a recent study [26] has shown that Ca^{2+} and Ba^{2+} cations intercalate in between GO sheets and strongly interact with sp^2 clusters of GO sheets through cation-π interactions. The study also has shown that the metal ions can bind to different positions of the graphene sheets, and that the binding energy not only depends on the position, but also on the metal cation. These results indicate that the Barium ion binds stronger than Calcium to graphene sheets. A preceding investigation [27] into competitive binding between alkaline earth metal ions with water and benzene has concluded that the solvent exchange rate between the cations and benzene strongly depends on the solvation extent of a cation. The study shows that Barium rapidly exchanges water molecules with benzene, whereas the rate of exchange for Calcium strongly depends on the extent of solvation, showing the tendency to

decrease with increasing level of hydration. On the basis of the above information, we suggest that during the reduction reaction of GO in aqueous hydrazine medium, competing reactions between oxygenated groups on the alginate backbone, sp^2 clusters of rGO sheets, water molecules and alkaline earth metal ions take place, thus strongly affecting the orientation of the sheets inside the polymer matrix.

Surprisingly, we have found that Barium alginate, containing nearly 30 wt% of glycerol, possesses a semi-crystalline structure. To exclude the possibility of recrystallization of the Barium chloride salt and potential contamination, we performed XRD and elemental mapping experiments and found that corresponding scattering peaks of the salt do not at all match with the scattering pattern of Sodium chloride [28] nor Barium chloride (see Figure 3.7.2.-3.7.3. in Supporting Information). With increasing amount of rGO, the original semi-crystalline structure of Barium alginate is modified by the presence of the sheets resulting in what appears to be an incommensurately modulated crystalline structure. We speculate that structural changes begin taking place during the cross-linking procedure, and the system once again reorganizes itself during the reduction reaction in a complicated manner as discussed before.

3.5. Conclusions

We conclude, that highly aligned graphene oxide sheets in the Sodium alginate matrix can be obtained by a simple preparation method without the need of an external field. The degree of alignment of reduced graphene sheets in the Barium or Calcium alginate matrices, however, is compromised. Environmental Scanning Electron Microscopy micrographs have allowed us to observe a highly dense and layered structure of the composite samples of various compositions. X-ray diffraction studies have shown that different morphological structures can be formed upon cross-linking alginate with the divalent alkali metal ions in the presence of the filler. The preferential alignment of the sheets has been confirmed by 2-dimensional X-ray diffraction experiments. The Affine Deformation Model can accurately describe the data and confirms the formation of highly

ordered structures due to gelling and the associated yield stress development upon drying the samples.

The degree of alignment is influenced by several factors. Our study has shown, that competing interactions between an alkali metal ion, graphene oxide sheets and the polymer matrix in the aqueous environment render a range of possible order parameter values. Furthermore, the degree of order in the Sodium alginate matrix shows strong graphene oxide concentration dependence. Nevertheless, it is clear that our composite systems could be employed as potential gas barrier coatings comparable to what has been attained by other workers in the field [29] as the present results show that it is possible to make highly aligned composite films without requiring any complicated or time consuming preparation methods, such as layer-by-layer deposition.

Acknowledgements

The authors wish to acknowledge M. Bus for helping to obtain AFM images, and J.Zlopasa for fruitful discussions. We also appreciate Arjan Thijssen's help with ESEM images.

3.6. References

1. (a) Zhao, X.; Zhang, Q. H.; Chen, D. J.; Lu, P. *Macromolecules* **2010,** *43* (5), 2357-2363; (b) Song, P. G.; Cao, Z. H.; Cai, Y. Z.; Zhao, L. P.; Fang, Z. P.; Fu, S. Y. *Polymer* **2011,** *52* (18), 4001-4010.

2. Wang, X.; Yang, H. Y.; Song, L.; Hu, Y.; Xing, W. Y.; Lu, H. D. *Compos Sci Technol* **2011,** *72* (1), 1-6.

3. (a) Qi, X. Y.; Yan, D.; Jiang, Z. G.; Cao, Y. K.; Yu, Z. Z.; Yavari, F.; Koratkar, N. *Acs Appl Mater Inter* **2011,** *3* (8), 3130-3133; (b) Liao, K. H.; Qian, Y. Q.; Macosko, C. W. *Polymer* **2012,** *53* (17), 3756-3761.

4. (a) Kim, H.; Miura, Y.; Macosko, C. W. *Chem Mater* **2010,** *22* (11), 3441-3450; (b) Kuila, T.; Bose, S.; Mishra, A. K.; Khanra, P.; Kim, N. H.; Lee, J. H. *Polym Test* **2012,** *31* (1), 31-38.

5. Kuila, T.; Bose, S.; Mishra, A. K.; Khanra, P.; Kim, N. H.; Lee, J. H. *Prog Mater Sci* **2012,** *57* (7), 1061-1105.

6. Kim, H. M.; Lee, J. K.; Lee, H. S. *Thin Solid Films* **2011,** *519* (22), 7766-7771.

7. Yang, X. M.; Tu, Y. F.; Li, L. A.; Shang, S. M.; Tao, X. M. *Acs Appl Mater Inter* **2010,** *2* (6), 1707-1713.

8. Xu, Y. X.; Hong, W. J.; Bai, H.; Li, C.; Shi, G. Q. *Carbon* **2009,** *47* (15), 3538-3543.

9. Kang, H. L.; Zuo, K. H.; Wang, Z.; Zhang, L. Q.; Liu, L.; Guo, B. C. *Compos Sci Technol* **2014,** *92*, 1-8.

10. (a) Ionita, M.; Pandele, M. A.; Iovu, H. *Carbohyd Polym* **2013,** *94* (1), 339-344; (b) Cao, K. T.; Jiang, Z. Y.; Zhao, J.; Zhao, C. H.; Gao, C. Y.; Pan, F. S.; Wang, B. Y.; Cao, X. Z.; Yang, J. *J Membrane Sci* **2014,** *469*, 272-283; (c) Valentini, L.; Rescignano, N.; Puglia, D.; Cardinali, M.; Kenny, J. *Eur J Inorg Chem* **2015,** (7), 1192-1197; (d) Chen, K.; Shi, B.; Yue, Y.; Qi, J.; Guo, L. *Acs Nano* **2015,** *9* (8), 8165–8175.

11. Haug, A.; Smidsrod, O. *Acta Chem Scand* **1970,** *24* (3), 843-854.

12. Pawar, S. N.; Edgar, K. J. *Biomaterials* **2012,** *33* (11), 3279-3305.

13. Kovtyukhova, N. I.; Ollivier, P. J.; Martin, B. R.; Mallouk, T. E.; Chizhik, S. A.; Buzaneva, E. V.; Gorchinskiy, A. D. *Chem Mater* **1999,** *11* (3), 771-778.

14. (a) Stankovich, S.; Piner, R. D.; Chen, X. Q.; Wu, N. Q.; Nguyen, S. T.; Ruoff, R. S. *J Mater Chem* **2006,** *16* (2), 155-158; (b) Kulkarni, D. D.; Choi, I.; Singamaneni, S.; Tsukruk, V. V. *Acs Nano* **2010,** *4* (8), 4667-4676.

15. Zlopasa, J.; Norder, B.; Koenders, E. A. B.; Picken, S. J. *Macromolecules* **2015,** *48* (4), 1204-1209.

16. Scherrer, P. *Göttinger Nachrichten Math. Phys* **1918**, 98-100.

17. Kim, H.; Abdala, A. A.; Macosko, C. W. *Macromolecules* **2010,** *43* (16), 6515-6530.

18. Pei, S. F.; Cheng, H. M. *Carbon* **2012,** *50* (9), 3210-3228.

19. (a) Li, L. B.; Fang, Y. P.; Vreeker, R.; Appelqvist, I. *Biomacromolecules* **2007,** *8* (2), 464-468; (b) Sikorski, P.; Mo, F.; Skjak-Braek, G.; Stokke, B. T. *Biomacromolecules* **2007,** *8* (7), 2098-2103.

20. van Smaalen, S. *Crystallography Reviews* **1995,** *4* (2), 79-202.

21. Howe, J. Y.; Rawn, C. J.; Jones, L. E.; Ow, H. *Powder Diffr* **2003,** *18* (2), 150-154.

22. (a) Feng, S.; Xiong, X. Q.; Zhang, G. L.; Xia, N.; Chen, Y. M.; Wang, W. *Macromolecules* **2009,** *42* (1), 281-287; (b) Picken, S. J. *Macromolecules* **1990,** *23* (2), 464-470; (c) Picken, S. J.; Aerts, J.; Visser, R.; Northolt, M. G. *Macromolecules* **1990,** *23* (16), 3849-3854.

23. Saupe, A.; Maier, W. *Z Naturforsch Pt A* **1961,** *16* (8), 816-824.

24. Treloar, L. R. G., *The Physics of Rubber Elasticity*. 3rd ed.; Oxford Classic Texts in the Physical Sciences: 2005; p 62.

25. Wu, L. L.; Ohtani, M.; Takata, M.; Saeki, A.; Seki, S.; Ishida, Y.; Aida, T. *Acs Nano* **2014,** *8* (5), 4640-4649.

26. Sun, P. Z.; Zheng, F.; Zhu, M.; Song, Z. G.; Wang, K. L.; Zhong, M. L.; Wu, D. H.; Little, R. B.; Xu, Z. P.; Zhu, H. W. *Acs Nano* **2014,** *8* (1), 850-859.

27. Rodriguez-Cruz, S. E.; Williams, E. R. *J Am Soc Mass Spectr* **2001,** *12* (3), 250-257.

28. Wyckoff, R. W. G., Crystal Structures 1. Interscience Publishers: New York, 1963; pp 85-237.

29. (a) Gokhale, A. A.; Lu, J.; Parker, N. J.; Izbicki, A. P.; Sanyal, O.; Lee, I. *J Colloid Interf Sci* **2013,** *409*, 219-226; (b) Yang, Y. H.; Bolling, L.; Priolo, M. A.; Grunlan, J. C. *Adv Mater* **2013,** *25* (4), 503-508; (c) Huang, H. D.; Ren, P. G.; Chen, J.; Zhang, W. Q.; Ji, X.; Li, Z. M. *J Membrane Sci* **2012,** *409*, 156-163.

3.7. Supporting information

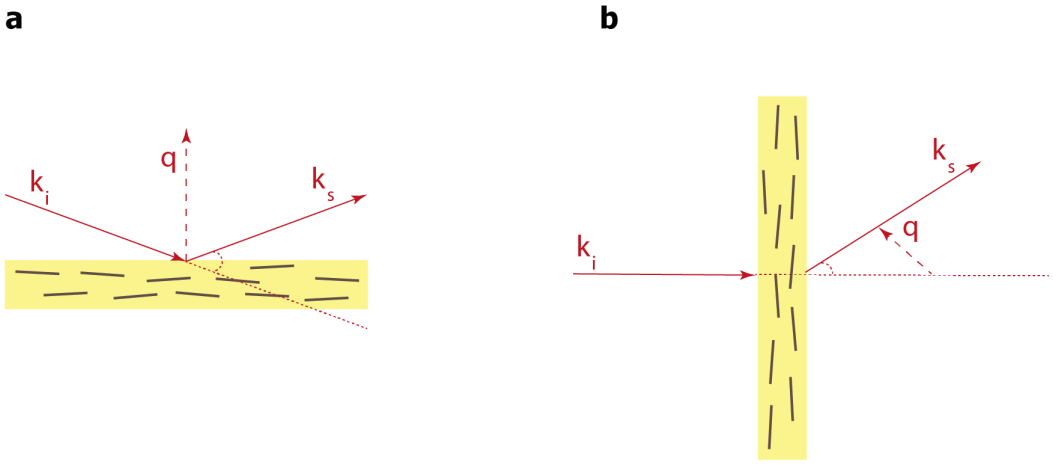

FIGURE 3.7.1. Schematic illustration of the scattering vector in a) reflection mode and b) transmission mode in the X-ray diffraction measurement.

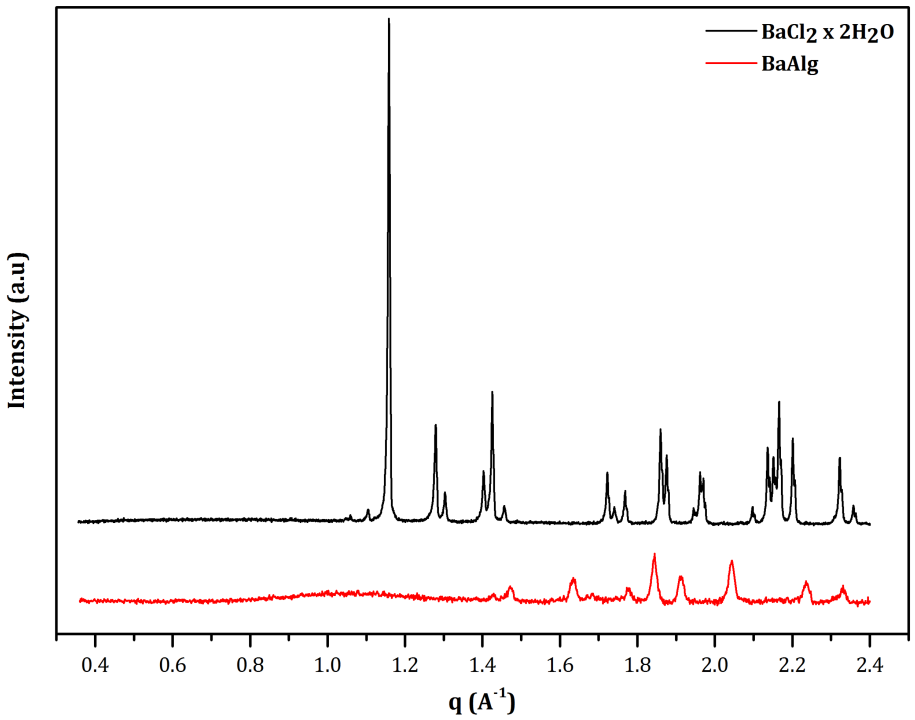

FIGURE 3.7.2. X-ray scattering patterns of $BaCl_2$ x $2H_2O$ (black solid line) and Ba-Alg (red solid line) sample film collected in reflection mode.

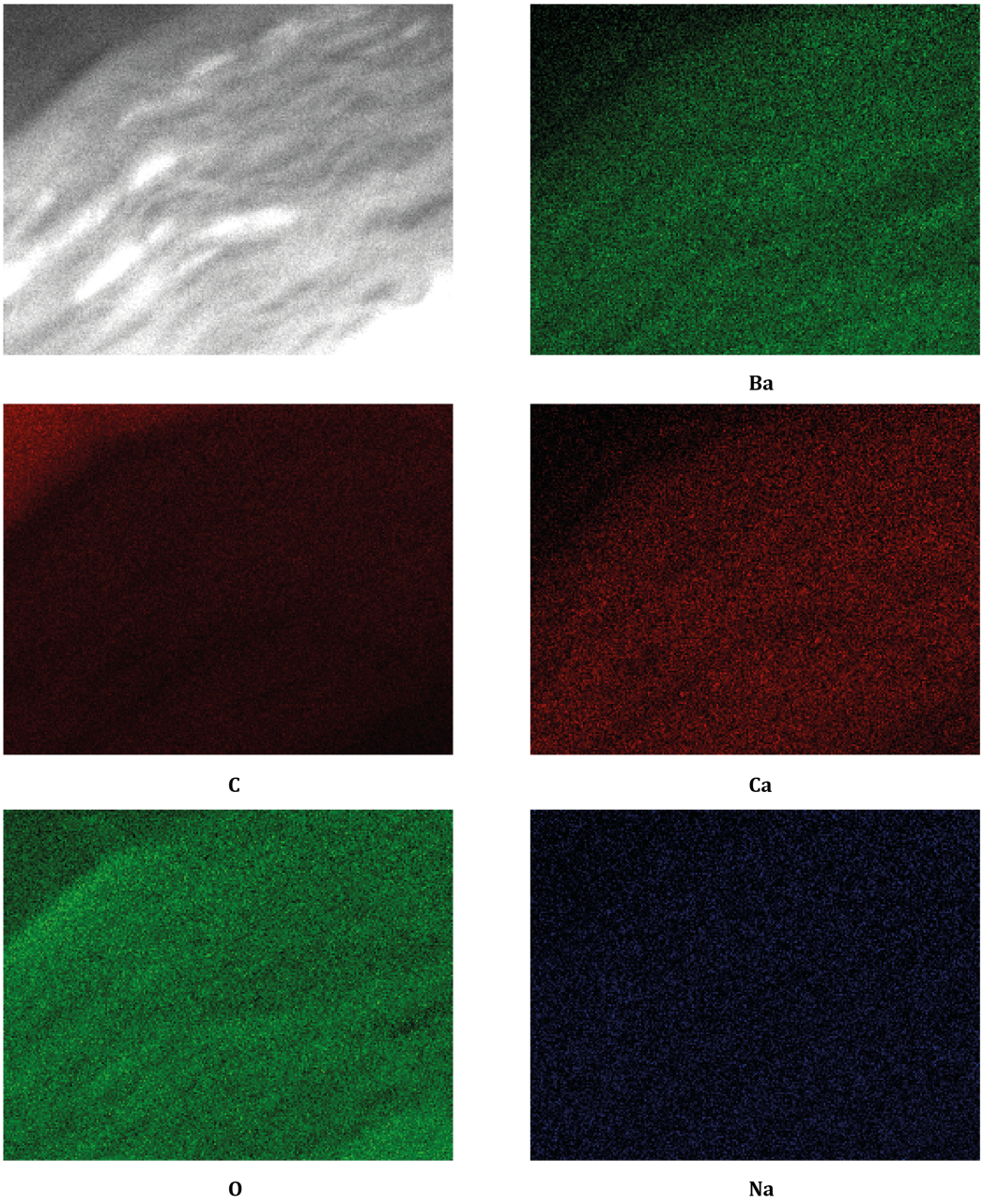

FIGURE 3.7.3. Electron microprobe images obtained of Ba-Alg/25wt% rGO sample (magnification x 10,000)

CHAPTER 4

WATER SORPTION AND DIFFUSION IN (REDUCED) GRAPHENE OXIDE-ALGINATE BIOPOLYMER NANOCOMPOSITES

This chapter is based on:

Vilcinskas, K., Zlopasa, J., Jansen, K. M. B., Mulder, F. M., Picken, S. J., Koper, G. J. M. *Water sorption and diffusion in (reduced) graphene oxide-alginate biopolymer nanocomposites*. Macromolecular Materials and Engineering, 2016, 301: p.1049−1063.

ABSTRACT

We analyze water sorption and diffusion in (reduced) graphene oxide-alginate composites of various compositions. Water sorption of Sodium alginate can be significantly reduced by the inclusion of graphene oxide sheets due to the formation of an extensive hydrogen-bonding network between oxygenated groups. Cross-linking alginate with divalent metal ions and presence of reduced graphene oxide can further improve the swelling resistance due to the strong interactions between metal ions, alginate and filler sheets.

Water sorption kinetics in all alginate composites indicate a non-Fickian diffusion process that can be accurately described by the Variable Surface Concentration model. In addition, water barrier properties of Sodium alginate-graphene oxide composites can be adequately predicted by using a simple model that takes the orientational order of the filler sheets and their effective aspect ratio into account.

Depending on conditions and composition, overall water barrier properties of alginate composites improve upon (reduced) graphene oxide filling, making them attractive for moisture barrier coating applications.

4.1. Introduction to water transport in alginate and its graphene composites

It is well established that the presence of high aspect ratio filler platelets, i.e. platelets with a large size to thickness ratio, forces diffusing species to undertake longer pathways while traversing polymer composites, thereby significantly improving the composite's barrier properties [1]. As a consequence, polymer composites with completely exfoliated and regularly arranged filler platelets are desirable as barrier coatings [2]. Since their isolation in 2004 [3], graphene and its derivative graphene oxide have attracted enormous attention in the field of polymer composites [4]. In particular, the inherent gas impermeability of graphene [5] and graphene oxide [6] makes them attractive for the preparation of barrier composites [7]. Indeed, inclusion of graphene (oxide) has been shown to significantly reduce water permeability through poly(vinyl alcohol) [8], polyimide [9], different types of nylon [10], starch [11] and natural rubber [12] composites.

Recently, a few studies have addressed the properties of Sodium alginate-graphene oxide composites [13]. Alginate is a naturally occurring block copolymer, comprised of irregularly arranged blocks of β-D-mannuronic acid (M) and α-L-guluronic acid (G) that form cross-linked junctions with multivalent metal ions [14]. The hydrophilicity of Sodium alginate and the presence of oxygenated groups on graphene sheets enable the easy dispersion of graphene oxide in water. Hence, Sodium alginate-graphene oxide composites can be readily prepared by solution casting. Among other properties, one study [13b] has examined the swelling resistance and the pervaporation of ethanol/water mixtures for membranes of Sodium alginate-graphene oxide and Sodium alginate-reduced graphene oxide. The authors have shown that inclusion of graphene (oxide) improves the swelling resistance of composite films due to the presence of aligned graphene (oxide) sheets and the formation of a hydrogen-bonding network between oxygenated groups of graphene (oxide) and alginate chains. In addition, the composite films exhibited a high selectivity and transport rate of water molecules due to the oxygen-containing groups on the graphene sheets, structural defects,

edge-to-edge slits and interfacial free cavities. However, the authors of the study did not investigate the mechanism of water sorption and diffusion for their composite films.

Earlier studies by Andreopoulos [15] and Hirai et al. [16] examined water sorption and diffusion in Sodium alginate, alginic acid and Cobalt cross-linked alginate films. These authors observed sigmoidal shaped water sorption curves of different types of alginates that suggest a non-Fickian water diffusion mechanism in alginates. As yet, water sorption and diffusion in Sodium alginate-graphene (oxide) composites containing high weight fractions of filler as well as in divalent metal ions cross-linked alginate-reduced graphene oxide composites have not been investigated systematically.

In this study we explore water sorption of different alginates and their (reduced) graphene oxide composites. In addition, we model the diffusion mechanism in the composite films and quantify water mobility. Lastly, we will show that the water barrier properties of Sodium alginate-graphene oxide composites are related to the orientational order of graphene oxide sheets in alginate matrix and their effective aspect ratio.

This study is not only of purely academic interest. Biocompatibility of alginates [17] and good barrier properties of (reduced) graphene oxide could be attractive for barrier coating applications and its composites may find application in, for instance, the food industry [18].

4.2. Experimental section

4.2.1. Sample preparation

The composite samples were prepared in the experimental procedure described in Chapter 3.

4.2.2. Characterization

Atomic force microscopy (NTMDT Ntegra) (AFM) was used to observe the morphology of graphene oxide sheets. For analysis, 0.05wt% graphene oxide aqueous dispersion was spin-coated on a clean silicon wafer (Siltronix) and examined in tapping mode.

Fourier Transform Infrared Spectroscopy (FTIR) experiments were performed with Nicolet 6700 spectrometer. The spectra were averaged over 128 scans at a resolution of 4 cm^{-1} in 650-4000 cm^{-1} range.

Gravimetric water vapor sorption analysis (TGA-RH) was performed on a Q5000SA (TA Instruments) instrument at 20 °C and 60 °C in the 1-80 % relative humidity (RH) range (water activity a_w=0.01-0.80 range). The instrument consists of a humidity and temperature-controlled chamber with inside a balance. Flushing the chamber with the combined streams of dry and wet nitrogen gas, the desired relative humidity values can be obtained where the installed thermocouples ensure homogenous temperature in the chamber during the experiment. For each measurement, one piece of a rectangular sample was used that was visually inspected prior the measurement to be without any visible structural defects. The mass of all specimens was close to 2 mg.

For the measurements at 20 °C, the samples were initially equilibrated at 60 °C and 1% RH for 1 hour to ensure they were moisture-free. Afterwards the temperature was lowered to 20 °C and 1% RH, and the samples were allowed to equilibrate at the corresponding conditions for 1 hour. Subsequently, the temperature was kept constant at 20 °C and the RH values were increased by 20% in each step. Water mass uptake was measured for 200 min at each RH value. If the weight change

was less than 2 µg for 10 min, the RH value was allowed to increase to a higher value. After having finished measuring the weight gain at 80% RH, the RH was lowered to 1%, and the desorption process continued for 800 min, unless the weight change was smaller than 2 µg for 10 min.

For the measurements at 60 °C, a similar procedure was followed in which the samples were subjected to pre-programmed relative humidity steps immediately after the drying step at 60 °C.

4.3. Results and discussion

4.3.1. FTIR analysis

There are strong indications in the literature [19] that alginate and its complex exhibit structural changes in the presence of multivalent ions. Hence, we included an FTIR analysis to analyze the influence of both filler material and multivalent ions, see Figure 4.1.

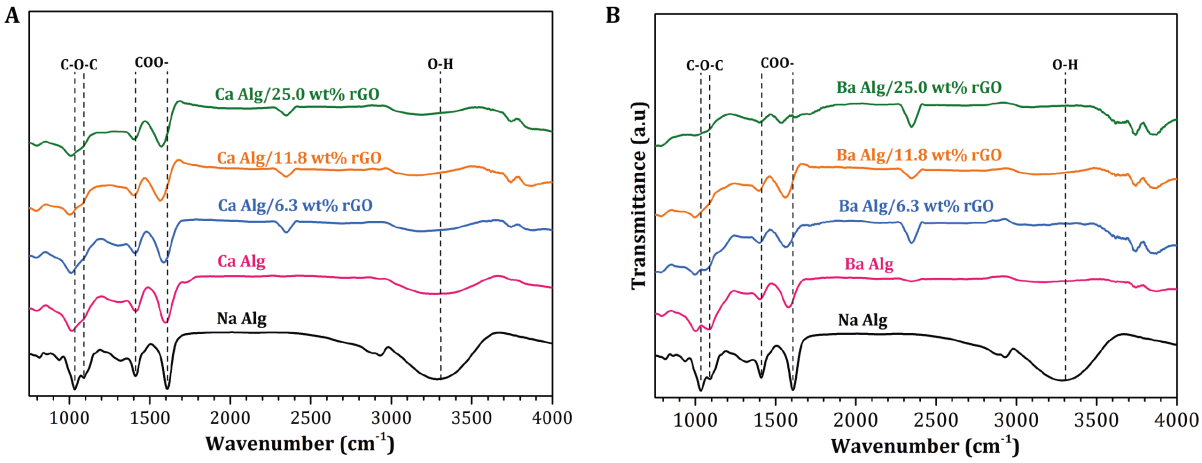

FIGURE 4.1. FTIR spectra of Sodium alginate (Na Alg), (A) Calcium alginate (Ca Alg) and its composites with various fractions of reduced graphene oxide (rGO) as well as (B) Barium alginate (Ba Alg) and its composites with various fractions of reduced graphene oxide (rGO). The spectra of each sample has been normalized and shifted upwards.

A summary of the characteristic peak positions is also presented in Table 4.1. As recent studies [13c, 20] investigated Sodium alginate-graphene oxide composites spectra in detail, we only focus on spectra

of divalent metal ion cross-linked-reduced graphene oxide composites and use the spectrum of Sodium alginate as a reference.

TABLE 4.1. Summary of characteristic peaks of composites of various compositions, see Figure 4.1.

Composition		*Peak positions (cm^{-1})*				
Polymer	Filler wt%	O-H stretching	C-O-O$^-$ stretching	C-O-O$^-$ stretching	C-O-C stretching	C-O-C stretching
Na-Alg/GO	0	3305	1607	1410	1090	1030
Ca-Alg/rGO	0	3275	1593	1418	–	1021
	6.3	3190	1577	1418	–	1022
	11.8	3170	1558	1418	–	1017
	25.0	3170	1576	1418	–	1018
Ba-Alg/rGO	0	3179	1577	1397	1080	989
	6.3	3179	1577	1397	1080	989
	11.8	3178	1576	1397	1080	989
	25.0	3101	1558	1397	–	–

As seen in Figure 4.1, the neat sodium alginate sample has produced characteristic peaks at 3305 cm^{-1}, 1607 cm^{-1}, 1410 cm^{-1}, 1090 cm^{-1} and 1030 cm^{-1}. The broad peak at 3305 cm^{-1} corresponds to stretching of hydroxyl groups, whereas the bands at 1607 cm^{-1} and 1410 cm^{-1} are characteristic for asymmetric stretching of carboxyl groups [19a]. The peak at 1030 cm^{-1} and a shoulder at 1090 cm^{-1} indicate stretching of C-O-C bonds [19b].

Since divalent metal ions can replace Sodium at carboxyl groups of alginate chains, the two peaks at 1607 cm^{-1} and 1410 cm^{-1} should be monitored for the ion exchange reaction [19a]. As presented in Figure 4.1 (A) and Table 4.1, after cross-linking alginate with Ca^{2+} ions, the peak at 1607 cm^{-1} has significantly weakened, broadened and shifted to 1593 cm^{-1}. Furthermore, the peak at 1410 cm^{-1} has also weakened, expanded and shifted to 1418 cm^{-1}. In addition, the shoulder at 1090 cm^{-1} has disappeared, and the peaks at 3305 cm^{-1} and 1030 cm^{-1} weakened, broadened and shifted towards lower frequencies. These changes indicate substitution of Sodium ions and formation of cross-linked

egg-box junctions between Calcium ions, carboxyl groups and oxygen atoms of alginates, see [21] for a schematic illustration.

Upon inclusion of chemically reduced graphene oxide (rGO), the bands at 3275 cm^{-1}, 1593 cm^{-1} and 1022 cm^{-1} have continued to move to lower wavenumbers, and their intensity has slightly decreased, albeit not so for the band of asymmetric stretching of carboxyl group. Such changes suggest that upon inclusion of the filler, the remaining unreduced oxygenated groups of rGO sheets can interact with the oxygenated groups of alginate chains, presumably via hydrogen-bonding. Indeed, during the hydrazine reduction process at ambient conditions, some of the oxygenated groups, such as hydroxyl and/or carbonyl, are preserved [22]. A band at 2362 cm^{-1} is ascribed to CO_2 molecules present in the ambient.

Similar changes in spectra have been observed upon cross-linking with Barium ions, see Figure 4.1 (B), and subsequent inclusion of rGO, although with some differences. As for the Calcium cross-linked alginate, upon ion exchange reaction with Barium ions, the bands at 3305 cm^{-1}, 1607 cm^{-1} and 1410 cm^{-1} diminish in intensity and shift towards lower wavenumbers. However, the peak at 1030 cm^{-1} has moved to much lower frequency in comparison to that of Calcium alginate, and the shoulder at 1090 cm^{-1} has not disappeared, but rather shifts to lower wavenumbers. Such dissimilar interaction with divalent metal ions could presumably originate from the distinct binding of these ions to alginate chains [24] that we further discuss in the succeeding paragraphs. In addition, these observations also suggest that Barium ions interact stronger with the oxygenated groups of alginate chains as manifested in the shift to lower frequencies. Upon inclusion of rGO, the characteristic peaks at 1577 cm^{-1}, 1397 cm^{-1} and 989 cm^{-1} do not change their position, but rather gradually diminish in intensity, whereas the shoulder peak only disappears for higher weight fractions of rGO. Such dissimilar interactions with Barium ions imply specific interactions between different divalent metal ions, polymer and filler, that are governed by the affinity of metal ion to the polymer matrix and filler sheets.

4.3.2. Water sorption

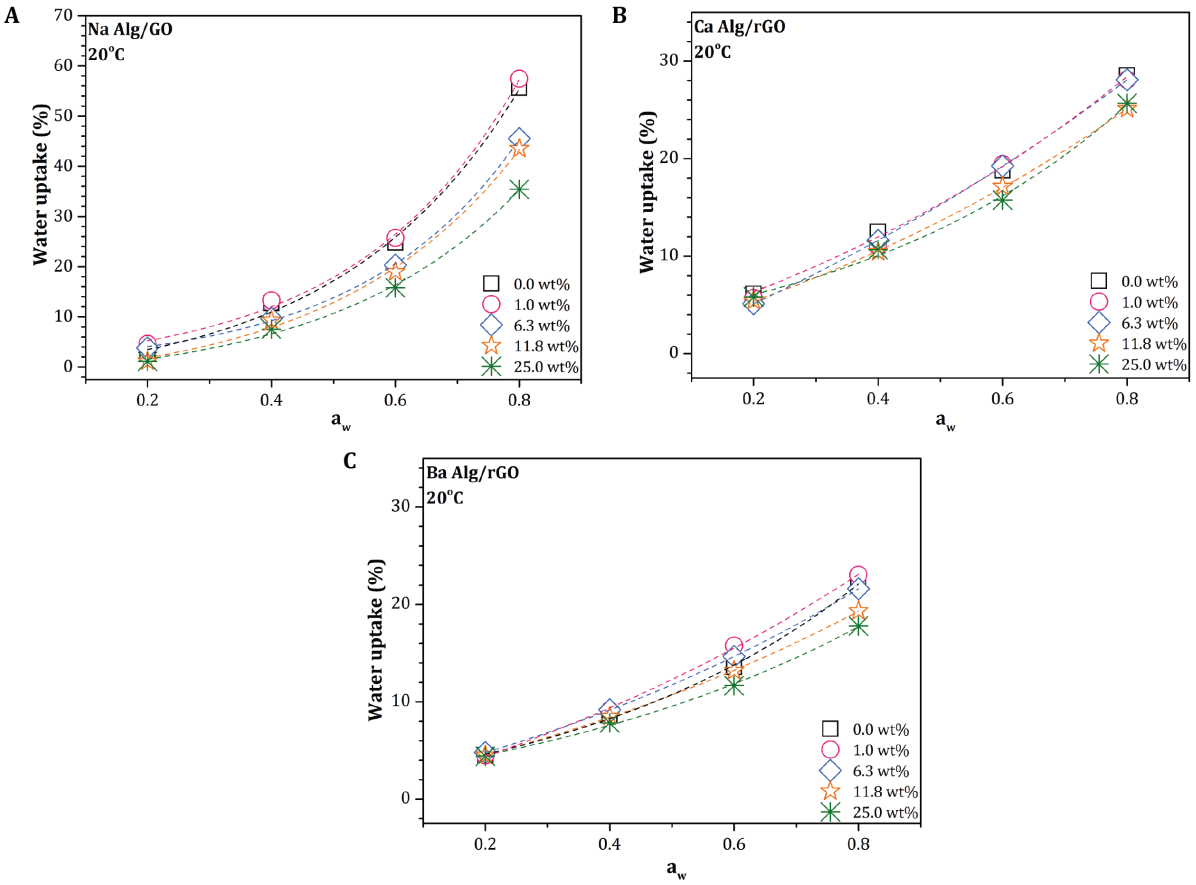

FIGURE 4.2. Water sorption isotherms at 20°C of (A) Sodium alginate-graphene oxide composites, (B) Calcium alginate-reduced graphene oxide composites, and (C) Barium alginate-reduced graphene oxide composites. a_w indicates water activity or relative humidity. Please, note different ordinate scale bar of graphs (B)-(C). Dashed lines serve as guides to the eye only.

Figure 4.2 (A)-(C) shows water sorption isotherms at 20°C for alginate composites of various compositions. Based on the classification of sorption isotherms proposed by Brunauer et al. [24], water sorption isotherms of Sodium alginate-graphene oxide (Na-Alg/GO) composites appear to possess a sigmoidal shape, often observed for hydrophilic polymers [25]. On the other hand, the water sorption isotherms of divalent metal ion cross-linked alginate-reduced graphene oxide composites are more characteristic to those of less hydrophilic polymers [26]. Indeed, the interaction of divalent metal ions with oxygenated groups of alginate significantly reduces water sorption capacity, which is further

lowered by the more hydrophobic nature of chemically reduced graphene oxide. Although there are numerous water sorption models reported in literature[27], we have unfortunately not been able to obtain adequate fit of our data to any of them.

As illustrated in Figure 4.2 (A), the water uptake for Na-Alg/GO composites decreases with increasing weight fraction of graphene oxide (GO), most notably at higher water activity values a_w. However, the inclusion of small amounts (1 wt%) of GO slightly increases the water sorption capacity. We would like to point out that our composite films contain nearly 30 wt% of glycerol (by polymer weight) as a plasticizer that is known to strongly influence the water sorption capacity [28]. We suggest that upon addition of a small amount of GO, the initial hydrogen-bonding network between hydroxyl groups of glycerol and oxygenated groups of the alginate backbone is disrupted in a manner that allows more adsorption sites for the water molecules, hence increasing the sorption capacity. With further increment of the GO weight fraction, favorable structural rearrangements take place that yield fewer adsorption sites for water molecules due to the formation of the extensive hydrogen-bonding network between oxygenated groups of GO sheets and polymer backbone [13c]. Furthermore, the water sorption capacity is also influenced by water activity. At low humidity values, sorption is insignificant due to the presence of a strong hydrogen-bonding network, but as the water activity increases, water uptake becomes more considerable due to the increased number of sorbed water molecules that weaken the hydrogen-bonding network between the filler sheets and alginate chains, thus increasing polymer chain mobility and free volume.

On the other hand, as illustrated in Figure 4.2 (B)-(C), the water sorption capacity for divalent metal ion cross-linked alginate composites is significantly reduced, albeit not at low water activity (a_w=0.2) where it is higher than that of Na-Alg/GO composites. We propose that the higher water sorption capacity at low water activity arises due to the increased free volume in composites upon introduction of divalent metal ions. As initially available vacancies are occupied by water molecules, the improved swelling resistance at higher water activities can be attributed to strong interactions

between divalent metal ions, oxygenated groups of graphene sheets and polymer backbone that solvent molecules are not able to break efficiently. In addition, Barium alginate composites show the lowest water sorption capacity, suggesting that the higher affinity of Ba^{2+} ions to the polymer backbone [29] and carboxyl groups present on the graphene oxide sheets [30] results in stronger interaction that significantly reduce water uptake in comparison to Calcium alginate and its composites. Indeed, interactions between divalent metal ion cross-linked alginates and their reduced graphene oxide composites, as analyzed by FTIR, have shown to be dependent on the divalent metal ion. Overall, the swelling resistance of alginate significantly improves upon introduction of cross-linked junctions with divalent metal ions. The strong interactions between divalent metal ions, oxygenated groups on graphene sheets, and the alginate backbone, as well as the hydrophobic nature of reduced graphene oxide contribute to the decreased water sorption capacity.

Although not yet at equilibrium, Sodium alginate-graphene oxide composites appear to desorb almost completely whereas divalent metal ion cross-linked alginate-reduced graphene oxide composites still contain a small amount of water (graphs not shown here). This observation indicates that water molecules remain stronger bonded to the metal cross-linked alginate composites, presumably due to the higher coordination number of divalent metal ions [31].

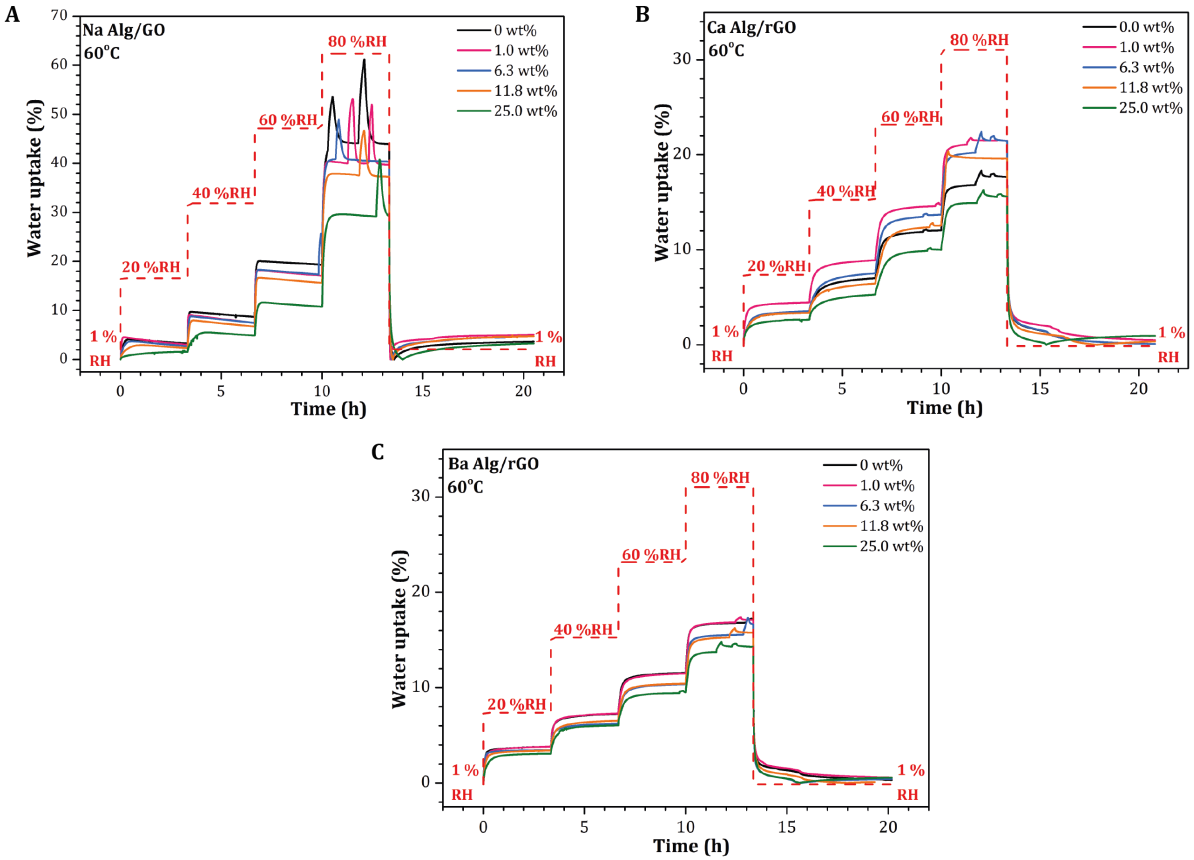

FIGURE 4.3. Water mass uptake versus sorption time graphs at 60°C for (A) Sodium alginate-graphene oxide composites, (B) Calcium alginate-reduced graphene oxide composites and (C) Barium alginate-reduced graphene oxide composites.

As illustrated in Figure 4.3(A)-(C), the water sorption capacity of alginate composites at 60°C, is reduced. Water mass uptake of non-cross-linked Na-Alg/GO composites exhibit a negative slope, indicating dominance of desorption primarily whereas water sorption curves of divalent metal ion cross-linked alginate-graphene composites suggest prevailing water sorption process. Nonetheless, overall sorption capacity of alginate composites is reduced in comparison with that at 20°C. Such dissimilar behavior could arise from different interaction strength between the constituents in the cross-linked and non-cross-linked alginate composites. We speculate that the hydrogen-bonding network between oxygenated groups of graphene oxide and alginate backbone is being disrupted at elevated temperatures leading to substantial increase in free volume of the composites. Furthermore, interaction between water molecules and exposed oxygenated groups of the

constituents are not strong enough to retain them attached by hydrogen bonding. Therefore, initially sorbed water molecules are only weakly bonded and able to escape via passages created by de-bonding between the filler and polymer. In the divalent metal ion cross-linked alginate-reduced graphene oxide composites, however, bonding is primarily based on Coulombic interactions that are at least several times stronger than hydrogen-bonding [32]. Although some structural rearrangements occurring at elevated temperatures should not be excluded, water molecules presumably are not able to attach to oxygenated groups of the constituents, therefore are able to move through interstitial cavities in the cross-linked alginate-graphene composites.

The peaks at high water activity (a_w=0.8) at 60°C are of experimental origin and should not be interpreted as real physical effects.

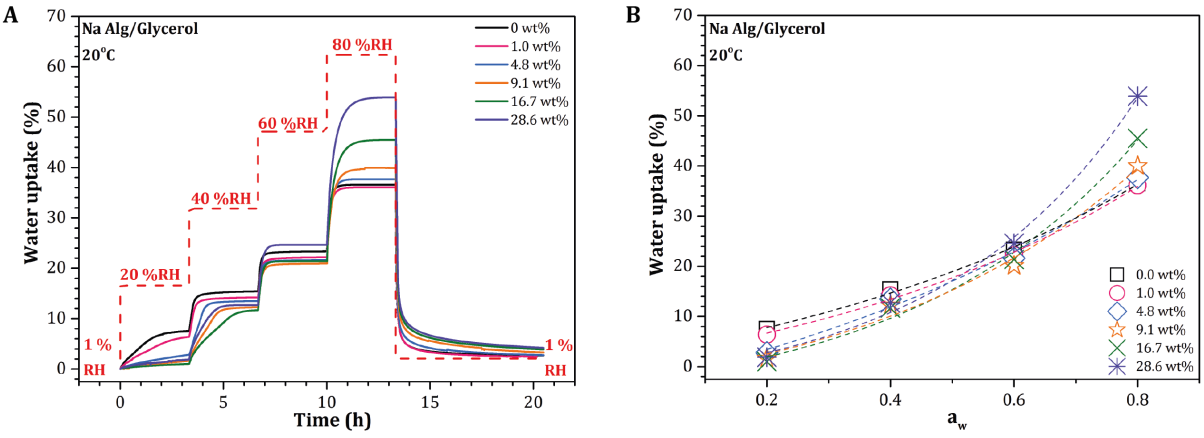

FIGURE 4.4. Water mass uptake versus sorption time graphs of Sodium alginate with various weight fractions of glycerol at (A) 20°C. Figure (B) illustrates the degree of swelling at 20°C of Sodium alginate with different weight fractions of glycerol. Dashed lines serve as a guide for eye.

At the same time, the presence of plasticizer (glycerol) in the alginate composites should not be neglected. Our introductory analysis of water uptake of Sodium alginate containing various weight fractions of glycerol suggests an important role of glycerol. As presented in Figure 4.4, the presence of glycerol significantly affects the water sorption capacity of Sodium alginate. As seen in Figure 4.4 (A)-(B) at small weight fractions of glycerol, the water sorption capacity slightly decreases suggesting

strong hydrogen-bonding based interaction between oxygenated groups of alginate and hydroxyl groups of glycerol, that water molecules are only able to disrupt at higher water activities. At higher weight fractions of plasticizer the water sorption presumably increases due to the excess of glycerol, where its hydrophilic groups offer binding sites for water molecules. Avella et al. [33] has investigated physico-mechanical properties of alginates comprised of dissimilar guluronic and mannuronic acid contents that contained varying weight fractions of glycerol. Having observed different thermal properties of alginates that showed strong plasticizer dependence, the authors suggested that binding of glycerol molecules to alginate chains is influenced by its weight fraction and the composition of the alginates. Namely, polymer chains of alginates rich in mannuronic acid units are more flexible and assume a more linear conformation, therefore glycerol molecules bonded to the polymer backbone still remain available. On the other hand, polymer chains of alginates rich in guluronic acid units are more folded and buckled, hence at low weight fractions of glycerol, alginate chains can encase the glycerol molecules. At higher weight fractions of glycerol, the accessible binding sites to guluronic acid units become saturated, thus glycerol molecules bonded to mannuronic acid units offer adsorption sites to water molecules. Indeed, as seen in Figure 4.4 (A)-(B), for the higher guluronic acid content possessing alginate we have used in our experiments, water sorption increased at high weight fractions of glycerol.

4.3.3. Modeling water diffusion and structural changes in alginate composites

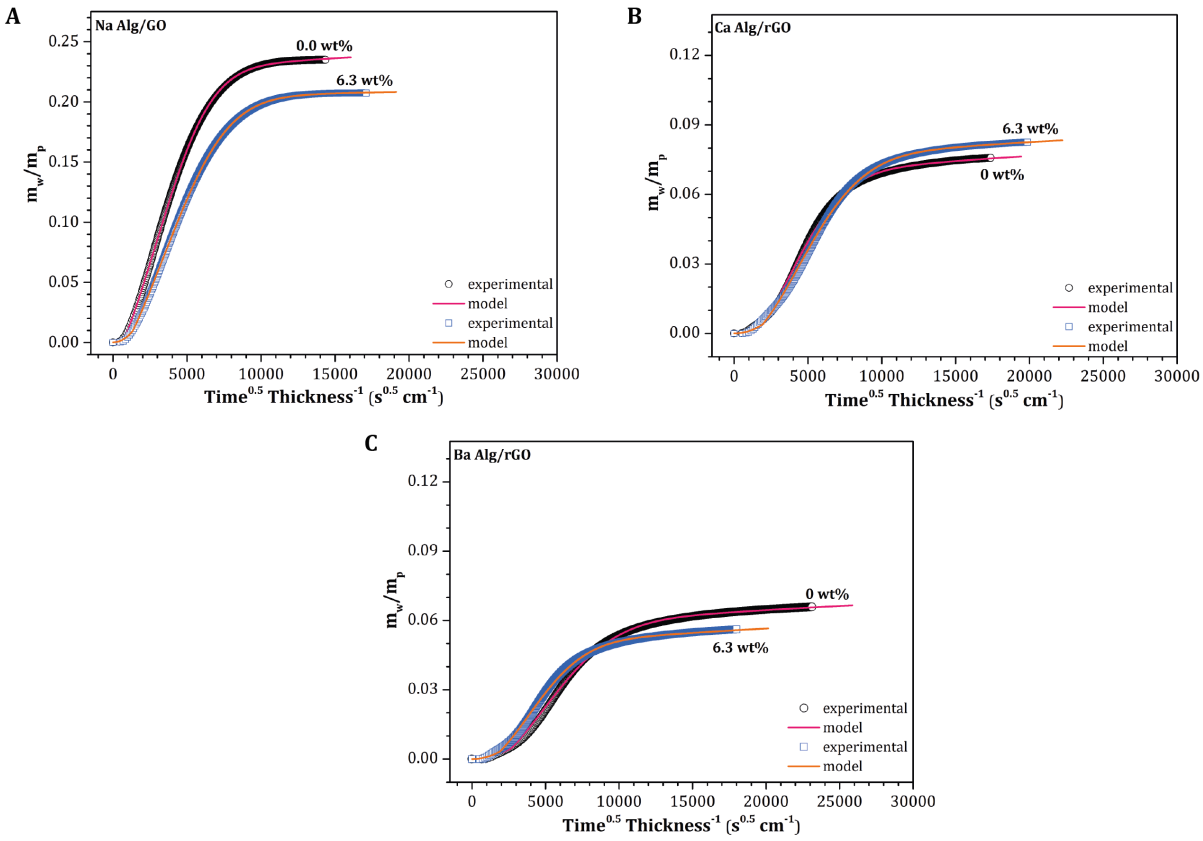

FIGURE 4.5. Representative moisture absorption versus scaled time curves taken at 20°C and a_w=0.8 of (A) Sodium alginate-graphene oxide composites, (B) Calcium alginate-reduced graphene oxide composites and (C) Barium alginate-reduced graphene oxide composites.

Figure 4.5 illustrates representative moisture sorption data (open symbols). All moisture sorption curves of alginate composites show a distinctive sigmoidal shape, indicating a non-Fickian water vapor diffusion mechanism in the composite films, previously also observed for alginate films [15-16]. In an attempt to model and quantify water diffusion in alginates and their composites, we have used the Variable Surface Concentration Model [34] to fit the experimental data (solid lines). In this model water sorption and diffusion take place in two steps. Initially, upon introduction of diffusing species, their concentration at the sample surface quickly jumps to a value C_0, and the diffusion process is governed by the concentration gradient established by C_0. In the second stage, the concentration of diffusing species slowly increases to equilibrium value of C_∞ via a first order relaxation process with

relaxation rate *k*. As proposed by the authors, the concentration gradient in the second stage becomes negligibly small and the diffusion process is governed only by the increment of the surface concentration.

The relative mass uptake of diffusing species is expressed as [35]:

$$\frac{M_t}{M_\infty} = \phi\left[1-\frac{8}{\pi^2}\sum_{n=0}^{\infty}\frac{\exp\left(\frac{-(2n+1)^2\pi^2\theta}{4}\right)}{(2n+1)^2}\right]+ \\ +(1-\phi)\left[1-\frac{\tan\sqrt{\psi}\exp(-\psi\theta)}{\sqrt{\psi}}-\frac{8}{\pi^2}\sum_{n=0}^{\infty}\frac{\exp\left(\frac{-(2n+1)^2\pi^2\theta}{4}\right)}{(2n+1)^2\left(1-\frac{(2n+1)^2\pi^2}{4\psi}\right)}\right] \quad (4.1)$$

The first term of Equation (4.1) represents the Fickian diffusion stage, where the diffusing species penetrate the sample due to the established concentration gradient. The second term of Equation (2) describes the diffusion process governed by the time-dependent surface concentration. In addition, Equation (4.1) contains three physically meaningful transport parameters, namely Φ – the relative initial concentration; D – the diffusion coefficient; ψ – the inverse of the diffusion Deborah number:

$$\phi = \frac{C_0}{C_\infty};\ \theta = \frac{Dt}{l^2};\ \psi = \frac{kl^2}{D} \quad (4.2)$$

where: C_0 is the initial water vapor concentration at the surface of the film sample; C_∞ – equilibrium water vapor concentration; k – relaxation rate; Θ – dimensionless time; t – sorption time, l – thickness of the film sample. A similar expression for the diffusion of solvent in polymer particles was studied by one of us [36].

The relative initial concentration Φ represents the ratio of the initial surface concentration of diffusing species to that achieved in the second stage of sorption. The dimensionless time Θ obtained from the fit of the model to the data enable the extraction of the diffusion coefficient D. The third parameter, the inverse of the diffusion Deborah number ψ, stems from the diffusion Deborah number [37], which is defined as the ratio of characteristic relaxation time of polymer chains versus the characteristic time of diffusion. The diffusion Deborah number is widely used for identification of non-Fickian diffusion effects [26]. When the diffusion Deborah number is significantly larger than unity, the reorganization of polymer chains is slow and the diffusion process occurs quickly, such that the whole process resembles that of diffusing species through a solid material. Similarly, if the conformational changes are quicker than the characteristic diffusion time, the diffusion Deborah number is significantly smaller than unity, and the Fickian diffusion process prevails. On the other hand, if both processes are on a similar time scale, the diffusion and relaxation are coupled, and non-Fickian diffusion dominates, see references [37-38] for a comprehensive discussion.

As illustrated in Figure 4.5, there is excellent agreement between the experimental data (open symbols) and the Variable Surface Concentration Model (solid lines). Therefore, we used it to determine the relative initial concentration, the diffusion coefficient, and the diffusion Deborah number values for the alginate composites equilibrated at different temperatures and water activities.

4.3.3.1. Sodium alginate-graphene oxide composites

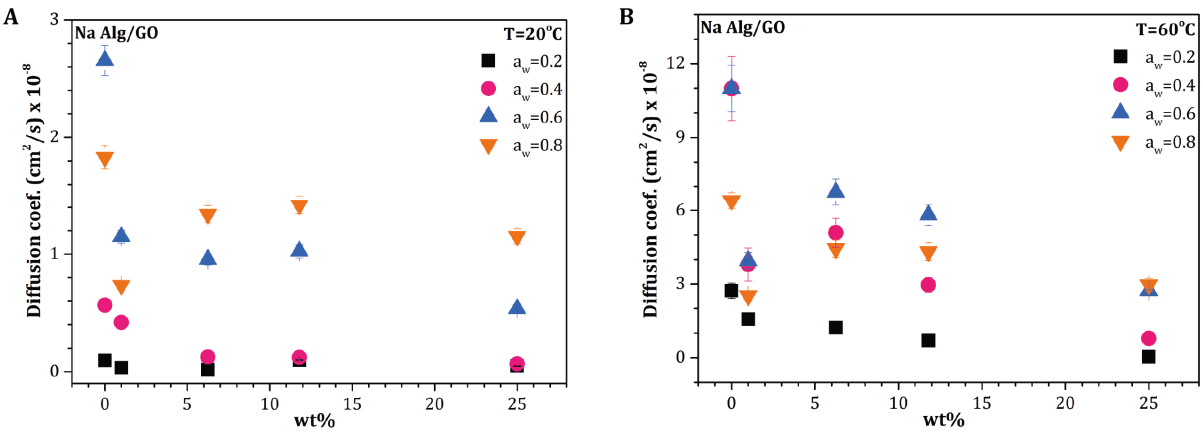

FIGURE 4.6. Estimated water diffusion coefficient values in Sodium alginate-graphene oxide composites of various compositions (wt% GO), and varying water activities at (A) 20°C and (B) at 60°C. Note that the ordinate values for graphs (A) and (B) are not equal.

As seen in Figure 4.6 (A)-(B) with increasing amount of graphene oxide, the mobility of water molecules becomes impeded due to the increased diffusion path in the presence of obstacles for diffusing species [1]. In addition, at lower water activities the diffusion coefficient values are small and increase with increasing relative humidity, albeit with some exceptions. At 20°C and low water activity (a_w=0.2), the mobility of water molecules in guluronic acid units rich Sodium alginate containing ~30 wt% of glycerol is low due to the bulk encapsulation of glycerol molecules that apparently only slightly increase the unoccupied interstitial space between polymer chains available for water transport. As water activity increases, it begins to disrupt the hydrogen-bonding network between polymer and plasticizer, and adsorbed water molecules considerably increase the spacing between adjacent chains, thus allowing more room for solvent molecules to move. However, at high water activity (a_w=0.8), maneuverability of water molecules may become restricted due to lower mobility of water clusters [39]. As proposed by the author, at low water activities, the water molecules strongly attach to the available hydrophilic groups, thus becoming relatively immobile. As water activity increases, the hydrophilic groups become saturated and additional water molecules will bind

more weakly to the already adsorbed water molecules, in this way forming a multilayer of water that is more mobile. With the further increment of water activity, the formation of water clusters results in decreased water mobility due to the relative immobility of these clusters.

Upon inclusion of graphene oxide sheets, water mobility does not change significantly at low water activity (a_w=0.2) and 20°C. As discussed earlier, the presence of an extensive and robust hydrogen-bonding network between oxygenated groups on graphene sheets and alginate backbone offers few adsorption sites for molecules resulting in negligible amount of sorbed water. Therefore, the available adsorption sites strongly interact with attached water molecules and restrict their mobility. With increasing water activity, however, the water mobility in the composites improves due to the increased free volume caused by the sorption as well as higher mobility of the newly sorbed water molecules. On the other hand, high weight fractions of filler are effective in impeding water mobility, as the water molecules are compelled to take longer pathways due to the presence of GO sheets. The decreased water transport for the sample containing 1 wt% of GO at high water activity (a_w=0.8) corroborates water sorption results discussed in the preceding paragraph and illustrated in Figure 4.2 (A), namely that increased water sorption capacity facilitates formation of relatively immobile water clusters.

In contrast to reports in literature [6, 13b], we have not observed reduced water barrier properties for Sodium alginate-graphene oxide composites. It has been argued that water molecules permeate through GO membranes entirely unimpeded due to the formation of empty spaces between non-oxidized regions of GO sheets that easily accommodate a monolayer of water molecules and allow low-frictional flow of them [6]. In addition, Cao et al. [13b] upon examination of sodium alginate-GO composites by Positron Annihilation Lifetime Spectroscopy, has concluded that addition of GO increases free volume in the sodium alginate-GO interface. Our data suggests that, even if transport of water molecules is unimpeded in GO sheets and the presence of additional space at the polymer-filler interface, inclusion of GO can nevertheless improve water barrier properties of Na-Alg/GO

composites. Besides, 2 dimensional X-ray diffraction analysis of Na-Alg/GO composites reveals a high in-plane alignment of GO sheets [40] that should significantly enhance barrier properties in the direction along the layer normal of composite samples. We have attempted to estimate the improvement of water barrier properties by taking into account the degree of filler alignment for Na-Alg/GO composites in the following paragraph.

Due to the increased kinetic energy of water molecules, water barrier properties at 60°C is significantly reduced in Sodium alginate-graphene oxide composites. Nonetheless, water barrier properties of the composites improve with the increasing weight fraction of GO sheets. Likewise for unfilled Sodium alginate and its 1 wt% GO composite at 20°C, the water mobility at 60°C initially increases with water activity, and is hindered at high water activity (a_w=0.8) due to the establishment of water clusters as discussed earlier. The samples containing higher weight fractions of GO show variable water activity dependence on mobility of solvent molecules. We speculate that increase in temperature disrupts the hydrogen-bonding network between polymer and plasticizer as well as polymer and filler, thereby offering adsorption sites for water molecules, which in turn initiates the earlier discussed diffusion mechanism.

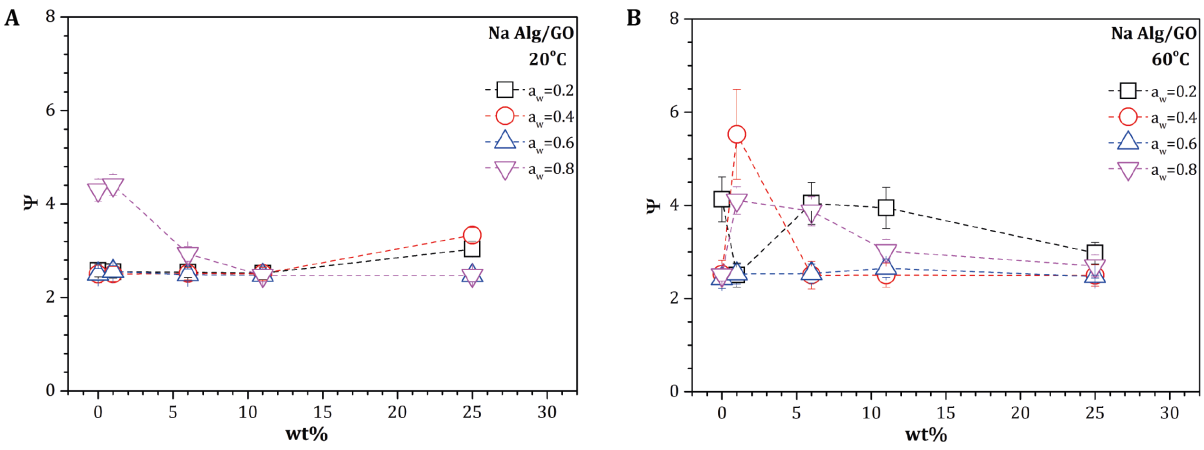

FIGURE 4.7. Diffusion Deborah number values in Sodium alginate-graphene oxide composites at (A) 20°C and (B) 60°C. Dashed lines serve as guides to the eye only.

Values of diffusion Deborah number in Sodium alginate-graphene oxide samples at various water activities at different temperatures are presented in Figure 4.7. As seen, the values are comparable and close to 2.5 for all the composites at all water activities at 20°C. Such close to unity value indicates that both relaxation and diffusion processes occur simultaneously. However, the diffusion Deborah number values at a_w= 0.2-0.4 are slightly higher for the composites containing 25 wt% of GO, implying that the extensive hydrogen-bonding network can restrict conformational changes. In addition, the diffusion Deborah number values at a_w=0.8 for unfilled Sodium alginate and its 1 wt% GO composite are also augmented, signifying the obstructive role of abundant water molecules to arrangements of polymer chains. The relative initial concentration values for all the samples are close to unity (Φ = 0.99), suggesting that water vapor concentration at the samples surface has not changed significantly in the second stage of sorption.

4.3.3.2. Alkaline earth metal ion cross-linked alginates

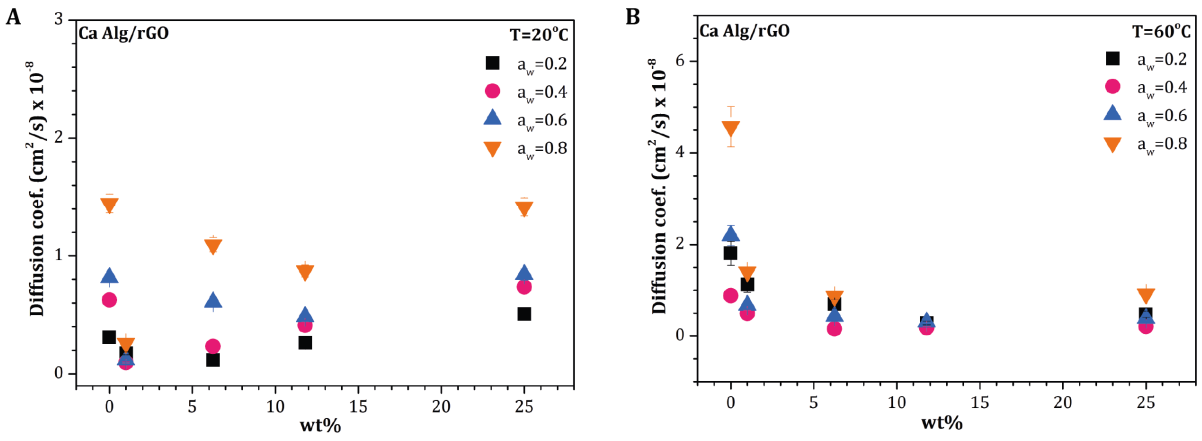

FIGURE 4.8. Estimated diffusion coefficient values for Calcium alginate-reduced graphene oxide (Ca-Alg/rGO) composites of various compositions, and varying water activities at (A) 20°C and (B) at 60°C. Note that the ordinate values for graphs (A) and (B) are not equal.

Figure 4.8 (A)-(B) illustrate the water mobility in Calcium alginate-reduced graphene oxide (Ca-Alg/rGO) composites of various compositions at different temperatures and water activities. In contrast to unfilled Sodium alginate, the water mobility at 20°C in a Calcium alginate polymer matrix

monotonically increases with the increasing water activity. Although water molecules diffuse faster at low water activities (a_w=0.2-0.4) in a Calcium alginate polymer matrix, their mobility is reduced at higher water activities (a_w=0.6-0.8), compared to unfilled Sodium alginate. Upon inclusion of 1 wt% of rGO, the water mobility in Calcium alginate-reduced graphene oxide composites is impeded at the investigated water activities range. In the samples containing higher weight fractions of rGO, water transport improves with increasing weight fraction of filler, and eventually becomes comparable to that of neat Calcium alginate for the samples containing 25 wt% of rGO. These observations suggest that the introduction of Ca^{2+} ions increases the free volume of polymer providing additional space for water molecules to move. Furthermore, inclusion of rGO appears to significantly alter the polymer structure when cross-linked with Calcium ions. We propose that upon cross-linking alginate with Calcium ions, the additional unoccupied space is created due to conformational changes of the polymer backbone. It has been reported that divalent metal ions, such as Calcium and Barium, have preferential binding sites to alginate oxygenated groups [23]. In their study the authors have suggested that Calcium ions preferentially bind to guluronic-guluronic acid and guluronic-mannuronic acid blocks. In particular, the presence of Calcium ions in between two guluronic acid units should increase the space between two adjacent polymer chains, while specific binding of Calcium ions to guluronic-mannuronic acid blocks is believed to maintain the initially linear polymer chain conformation (see Figure 1.8). Thus, at low water activities, water mobility is higher due to the created additional space when cross-linked junctions are formed. As seen in Figure 4.2 (B), the introduction of Calcium ions significantly improves the swelling resistance of the polymer, indicating a strong interaction between the metal ions and oxygenated groups of alginate chains that water molecules are not able to break efficiently even at high water activity values. Therefore, the formation of relatively immobile water clusters at high water activities in the available interstitial space reduces the diffusion coefficient value.

Presence of rGO in the Calcium alginate matrix, however, should inevitably alter the polymer structure. Before beginning to discuss effects of reduced graphene oxide weight fraction, we would

like to reiterate that we conduct the ion exchange reaction of free-standing Na-Alg/GO composite films cut in stripes by immersing them into solution of divalent metal ion salt, and subsequently reducing metal ion cross-linked alginate/GO samples in an aqueous hydrazine solution. We have previously suggested that during these processes, the competing interactions between metal ions, polymer chains and filler sheets can initiate complex structural changes [40]. In addition, it has been reported [41] that Calcium ions readily interact with carboxylic groups that are present on the edges GO sheets. Thus, before reduction of the oxygenated groups on GO sheets, the following interactions may occur: Calcium ion-alginate, alginate-Calcium ion-graphene oxide and graphene oxide-Calcium ion-graphene oxide. Based on this information, we propose that upon inclusion of low and moderate fractions (≤ 15wt%) of rGO, the interactions between the metal ions, filler sheets and polymer chains results in structural arrangements that reduce free volume, possibly by favorable Calcium ion-alginate and alginate-Calcium ion-reduced graphene oxide interactions, thus restricting water mobility and water sorption capacity (Figure 4.2 B). In addition, scarcity of oxygenated groups on rGO sheets that have been eliminated after reduction offer few sorption sites for water molecules. With further increment of rGO content, the competing interactions between the constituents presumably promotes the formation of interstitial cavities that ease transport of water molecules in the composite samples containing ≥15 wt% of rGO.

At increased temperatures the mobility of water molecules increases, as illustrated in Figure 4.8 (B). Most notably, the transport of solvent molecules significantly increases for unfilled Calcium alginate, whereas its composites with rGO show diminished diffusion coefficient values. Such observations suggest that the onset of hydro-thermally assisted decross-linking/bond re-arrangement, especially when $a_w \geq 0.6$, could be responsible for the improved water mobility in neat Calcium alginate. On the other hand, addition of rGO appears to favorably alter hydro-thermally induced structural re-arrangements in a complex manner that improves water barrier properties of Calcium alginate composites at higher temperatures.

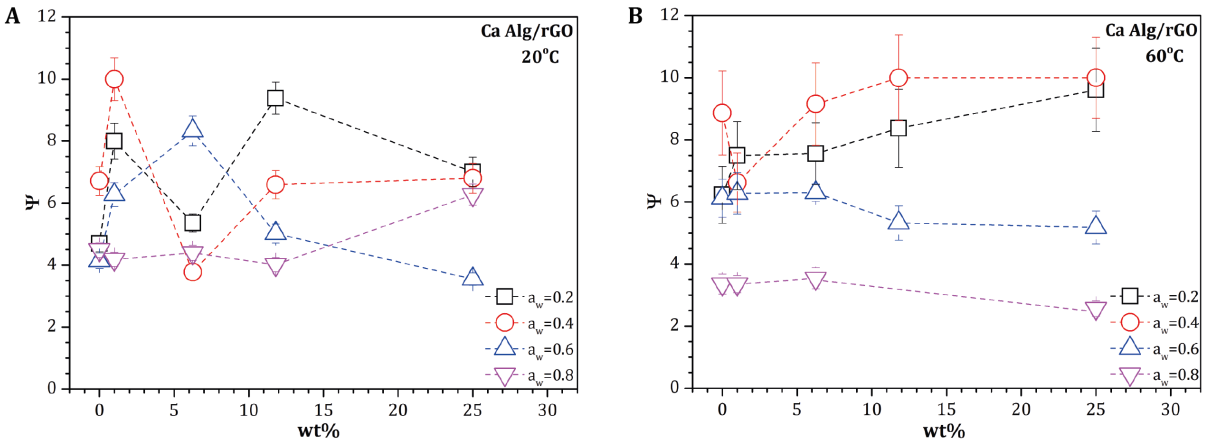

FIGURE 4.9. Diffusion Deborah number values in Calcium alginate-reduced graphene oxide composites at (A) 20°C and (B) 60°C. Dashed lines serve as guides to the eye only.

Estimated values of diffusion Deborah number in Ca-Alg/rGO composites at various water activities and temperatures are presented in Figure 4.9. In contrast to non-cross-linked Na-Alg/GO composites, the values of the parameter vary significantly with composition and water activity. Nonetheless, the values lie in between 1-10, indicating that concurrent diffusion and relaxation processes are taking place. Compared to the values of the diffusion Deborah number in unfilled Sodium alginate, the values of the corresponding parameter in Calcium alginate are slightly increased, suggesting reduced polymer chain mobility upon introduction of cross-linked junctions with Calcium ions. Upon inclusion of rGO in the Calcium alginate matrix, the diffusion Deborah number values change in a complicated manner, suggest complex multiple interactions between the constituents of the composites. In comparison to the non-cross-linked Na-Alg/GO composites, the equilibrium ratio constant Φ values for the Ca-Alg/rGO composites have decreased and lied in between 0.85-0.98, depending on water activity and composition. The highest values of Φ have been obtained for the samples at low water activity (a_w=0.2), which gradually decreased with increasing water activity. Such changes suggest that cross-linking alginate with Calcium ions and presence of rGO increases hydrophobicity of the polymer and its composites.

As for the diffusion Deborah number values at 60°C in Calcium alginate and its rGO composites, it appears that increasing water activity significantly improves polymer chain mobility as manifested in the decreasing diffusion Deborah number values. However, the uncertain variation of this parameter with the weight fraction of rGO suggests complex hydro-thermally induced interactions taking place in Calcium alginate and its rGO composites. The relative initial concentration Φ values for the composites exhibit similar values to that observed for the samples at 20°C.

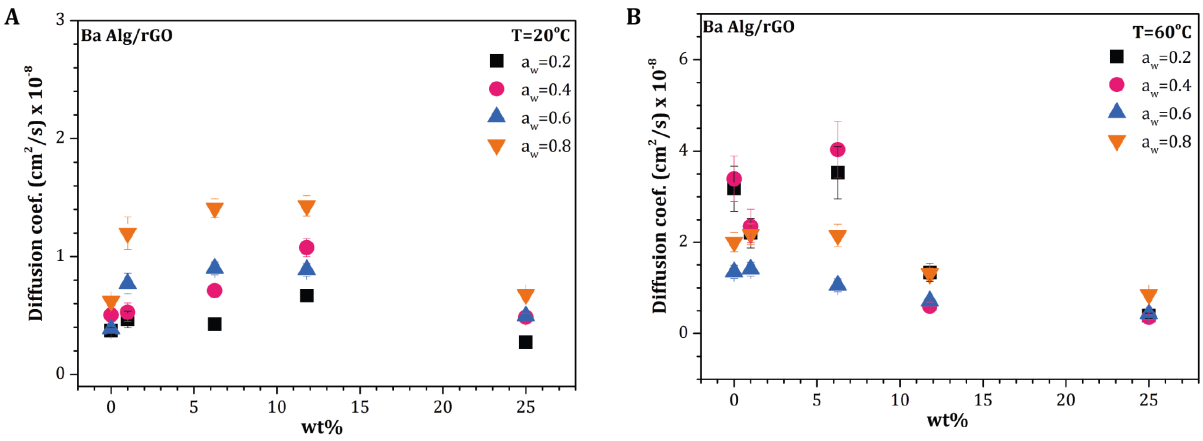

FIGURE 4.10. Estimated diffusion coefficient values in Barium alginate-reduced graphene oxide (Ba-Alg/rGO) composites of various compositions, and varying water activities at (A) 20°C and (B) at 60°C. Note that the ordinate values for graphs (A) and (B) are not equal.

Figure 4.10 (A)-(B) illustrate water transport in Barium alginate-reduced graphene oxide (Ba-Alg/rGO) composites of various compositions at different temperatures and water activities. In comparison to unfilled Calcium alginate, the water mobility at 20°C in Barium alginate decreases, except at water activity a_w=0.2. In addition, the water diffusion coefficient values in Barium cross-linked alginate remain lower at higher water activities (a_w=0.6-0.8) in comparison to non-cross-linked Sodium alginate. Contrary to Ca-Alg/rGO composites, inclusion of rGO promotes water mobility in Ba-Alg/rGO composites, albeit not in the samples containing 25 wt% of rGO. Depending on the composition and water activity, transport of water molecules is enhanced in Ba-Alg/rGO composites compared to Ca-Alg/rGO and Na-Alg/GO composites.

As introduced earlier, divalent metal ions show different binding affinity to mannuronic and guluronic acid blocks that comprise alginates [23]. As suggested by the authors, Barium ions exclusively bind to two guluronic acid and/or two mannuronic acid blocks (see the schematic illustration at the cited article). Such preferential binding of Barium ions renders a different alginate chain conformation compared to Calcium alginate. The presence of bigger Barium ions between two guluronic acid units should contribute to the increased free volume. On the other hand, binding to two mannuronic acid block of neighboring chains could compensate for the increased free volume. In addition, Barium ions possess higher affinity to the alginate matrix, hence binding to the oxygenated groups occurs more readily [29]. As revealed by X-ray diffractograms, the higher affinity of Barium ions and the preferential binding to alginate building blocks result in a semi-crystalline structure of Barium alginate, whereas Sodium and Calcium alginate possess an amorphous structure [40]. Based on this information, we propose that binding of Barium ions to mannuronic acid units flattens out the alginate chains thereby allowing mannuronic acid blocks to assume a linear conformation and order parallel to each other. In addition, X-ray diffraction studies of Barium alginate-reduced graphene oxide composites revealed a structural evolution, suggesting the formation of a quasi-crystalline structure in the presence of reduced graphene oxide [40]. We speculate that in Ba-Alg/rGO composites, alginate-Barium ion-alginate, and reduced graphene oxide-Barium ion-reduced graphene oxide interactions prevail as suggested by the observed X-ray diffractions patterns and the higher affinity of Barium ions to alginate [29] and graphene[30]. Such preferential interactions could result in conformational changes that increase unoccupied space in the composites, hence, allowing increased water mobility. On the other hand, at high weight fractions of rGO (≥25wt%), as discussed earlier, competing reactions between the constituents and higher affinity of Barium ions both to polymer and filler could promote structural changes that reduce the free volume which results in a reduced water mobility in the samples containing 25 wt% of rGO. However, further studies invoking Positron Annihilation Lifetime Spectroscopy are required

to verify the raised hypotheses for divalent metal ion cross-linked alginates and their reduced graphene oxide composites.

Likewise for other alginate composite systems, the increase in temperature facilitates water mobility in Ba-Alg/rGO composites. However, of all investigated alginate composite systems, transport of solvent molecules in Ba-Alg/rGO composites reveal the highest complexity. Contrary to previous observations, water diffusion coefficient values in Barium cross-linked composites show a tendency to decrease with increasing water activity. At present we cannot offer a sensible explanation for this effect.

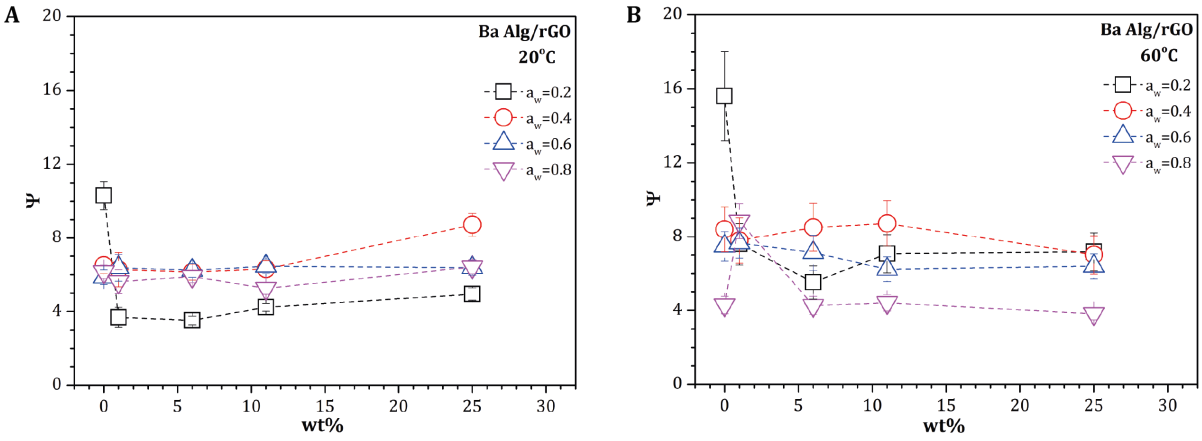

FIGURE 4.11. Diffusion Deborah number values in Barium alginate-reduced graphene oxide composites at (A) 20°C and (B) 60°C. Dashed lines serve as guides to the eye only.

The values for the diffusion Deborah number for Ba-Alg/rGO composites at different temperatures and water activities are presented in Figure 4.11. Likewise to Calcium alginate, the values at 20°C for Barium alginate are higher than those for Sodium alginate. Furthermore, the values are higher than those of Calcium alginate, indicating that higher affinity of Barium ions to alginate reduces polymer chain mobility more. As for the diffusion Deborah number values in Ba-Alg/rGO composites, they are comparable with those in Ca-Alg/rGO composites, and also exhibit a complex variation with water activities and composition. The initial relative concentration Φ values have shown similar values to

that observed for Ca-Alg/rGO composites, thus suggesting improved hydrophobicity of Ba-Alg/rGO composites.

The diffusion Deborah number values in Ba-Alg/rGO composites at 60°C show a similar trend as Ca-Alg/rGO composites with increasing water activities. However, the complex multiple parameter fitting procedure as well as at present undetermined hydro-thermally induced structural changes that take place precludes further discussion.

4.3.4. Modeling water barrier properties in Sodium alginate-graphene oxide composites

Having estimated the water mobility in Na-Alg/GO composites by using the Variable Surface Concentration model, we have attempted to describe the enhancement of the water vapor barrier properties in the composites at 20°C and a_w=0.6 taking into account the orientational order of the graphene oxide sheets in the alginate matrix [41]. We have applied a model, first proposed by L.E. Nielsen [1], of regularly arranged impermeable platelets embedded in a polymer matrix. The model is based on the assumption that in the presence of evenly dispersed impermeable platelets, the diffusing species will be compelled to take longer and more tortuous pathways, resulting in a significant increase in diffusion time and improved barrier properties. The barrier properties in composites are primarily governed by the size of filler (aspect ratio) and its volume fraction. However, this model assumes perfectly aligned and homogenously distributed platelets that do not form agglomerates. In order to account for imperfectly aligned filler platelets, the original model has been modified by Bharadwaj [42] to include the average order parameter $\langle P_2 \rangle$ values [43]. For perfectly aligned inclusions the average order parameter $\langle P_2 \rangle$ =1, whereas for isotropically oriented platelets $\langle P_2 \rangle$ =0. Based on the modified model, the relative diffusivity can be expressed as:

$$\frac{D}{D_0} = \frac{1-\phi_F}{1+\frac{\alpha}{2}\phi_F\left[\frac{2}{3}\left(\langle P_2 \rangle + \frac{1}{2}\right)\right]} \qquad (4.3)$$

where: D_0 is the diffusion coefficient in a polymer matrix, D – diffusion coefficient in a composite, Φ_F – filler volume fraction, α – aspect ratio of filler particles, $<P_2>$ - order parameter value.

We have recently observed highly aligned GO sheets within Sodium alginate matrix and quantified the average order parameter values $<P_2>$ for various filler weight fractions [40]. By employing Equation (4.3), we have tried to predict relative diffusivity in Sodium alginate-graphene oxide composites by assuming three different aspect ratios of GO sheets, and to compare the obtained values with the experimentally observed (see Figure 4.12 A).

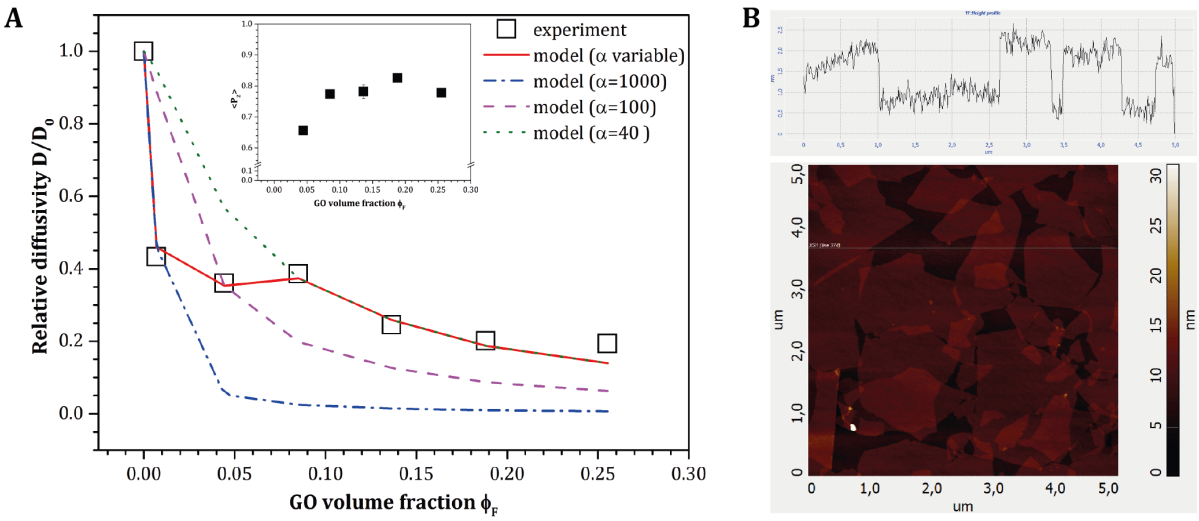

FIGURE 4.12. (A) Predicted relative diffusivity in Sodium alginate-graphene oxide composites depending on the aspect ratio of graphene oxide sheets and filler volume fraction. The inset graph shows a order parameter $<P_2>$ as a function of graphene oxide concentration. (B) Tapping mode AFM image (bottom) of GO sheets on silica substrate prepared from 0.05 wt% aqueous GO dispersion. The above picture represents height profile of the corresponding line.

As seen in Figure 4.12 (A), at high aspect ratio the presence of graphene oxide sheets ensure better water vapor barrier properties of the composite films (dotted, dashed and dashed-dotted lines in Figure 4.12 A), however a single high aspect ratio value does not enable to accurately predict the experimentally observed values. As illustrated in Figure 4.12 (B), graphene oxide sheets deposited from a dilute solution possess the average aspect ratio of 1000, however we have observed stacking

of sheets with increasing weight fraction of filler, which, in turn, would reduce the effective aspect ratio of graphene oxide sheets, especially at high weight fractions of filler. Therefore, we model water vapor barrier properties of the composites with varying aspect ratio of graphene oxide sheets. We suggest that at low volume fractions of filler, the aspect ratio remains high and close to 1000. With increasing weight fraction it gradually decreases until it becomes significantly smaller. Indeed, as illustrated in Figure 4.12 (A) by solid line, such estimation gives an adequate description of the experimentally obtained diffusivity in Sodium alginate-graphene oxide composites. So, by assuming varying aspect ratio of filler sheets and their average orientational order, water vapor barrier properties can be adequately estimated by invoking modified Nielsen's model.

4.4. Conclusions

We have investigated water sorption and diffusion in different alginate bionanocomposites. The FTIR spectra of divalent metal ion cross-linked alginates reveal stronger interaction between Barium ions and alginate chains in comparison to Calcium ions due to the higher affinity of the former. Upon introduction of the filler, the interactions between the constituents of the composites quickly become too complex to study with the present methods.

From the exposed water sorption and solvent mobilities at different temperatures and water activities in cross-linked and non-cross-linked alginate (reduced) graphene oxide composites, the sorption isotherms, showing a sigmoidal shape indicating a non-Fickian solvent diffusion mechanism, could be derived. The obtained isotherms can be modeled by the Variable Surface Concentration model. We conclude that overall, depending on the composition, alginate-reduced graphene oxide composites can indeed effectively reduce water mobility and therefore become attractive to coating applications. Furthermore, water barrier properties of Sodium alginate-graphene oxide composites can be adequately predicted by invoking a modified Nielsen's model that takes into account average orientational order of filler sheets and their effective aspect ratio.

Acknowledgements

We acknowledge H.Broekhuizen for the assistance with the TGA-RH instrument.

4.5. References

1. Nielsen, L. E. *Journal of Macromolecular Science: Part A - Chemistry* **1967,** *1* (5), 929-942.

2. Lange, J.; Wyser, Y. *Packag Technol Sci* **2003,** *16* (4), 149-158.

3. Novoselov, K. S.; Geim, A. K.; Morozov, S. V.; Jiang, D.; Zhang, Y.; Dubonos, S. V.; Grigorieva, I. V.; Firsov, A. A. *Science* **2004,** *306* (5696), 666-669.

4. (a) Compton, O. C.; Nguyen, S. T. *Small* **2010,** *6* (6), 711-723; (b) Huang, X.; Qi, X. Y.; Boey, F.; Zhang, H. *Chem Soc Rev* **2012,** *41* (2), 666-686; (c) Gambhir, S.; Jalili, R.; Officer, D. L.; Wallace, G. G. *Npg Asia Mater* **2015,** *7*.

5. Bunch, J. S.; Verbridge, S. S.; Alden, J. S.; van der Zande, A. M.; Parpia, J. M.; Craighead, H. G.; McEuen, P. L. *Nano Lett* **2008,** *8* (8), 2458-2462.

6. Nair, R. R.; Wu, H. A.; Jayaram, P. N.; Grigorieva, I. V.; Geim, A. K. *Science* **2012,** *335* (6067), 442-444.

7. Yoo, B. M.; Shin, H. J.; Yoon, H. W.; Park, H. B. *J Appl Polym Sci* **2014,** *131* (1).

8. Huang, H. D.; Ren, P. G.; Chen, J.; Zhang, W. Q.; Ji, X.; Li, Z. M. *J Membrane Sci* **2012,** *409*, 156-163.

9. Tseng, I. H.; Liao, Y. F.; Chiang, J. C.; Tsai, M. H. *Mater Chem Phys* **2012,** *136* (1), 247-253.

10. Jin, J.; Rafiq, R.; Gill, Y. Q.; Song, M. *Eur Polym J* **2013,** *49* (9), 2617-2626.

11. Ma, T. T.; Chang, P. R.; Zheng, P. W.; Ma, X. F. *Carbohyd Polym* **2013,** *94* (1), 63-70.

12. Yan, N.; Buonocore, G.; Lavorgna, M.; Kaciulis, S.; Balijepalli, S. K.; Zhan, Y. H.; Xia, H. S.; Ambrosio, L. *Compos Sci Technol* **2014,** *102*, 74-81.

13. (a) Ionita, M.; Pandele, M. A.; Iovu, H. *Carbohyd Polym* **2013,** *94* (1), 339-344; (b) Cao, K. T.; Jiang, Z. Y.; Zhao, J.; Zhao, C. H.; Gao, C. Y.; Pan, F. S.; Wang, B. Y.; Cao, X. Z.; Yang, J. *J Membrane Sci* **2014,** *469*, 272-283; (c) Chen, K.; Shi, B.; Yue, Y. H.; Qi, J. J.; Guo, L. *Acs Nano* **2015,** *9* (8), 8165-8175.

14. *Advances in Natural Polymers: Composites and Nanocomposites*. 1 ed.; Springer-Verlag Berlin Heidelberg: 2013; Vol. 18, p 426.

15. Andreopoulos, A. G. *Biomaterials* **1987,** *8* (5), 397-400.

16. Hirai, A.; Odani, H. *J Polym Sci Pol Phys* **1994,** *32* (14), 2329-2337.

17. *Advances in Natural Polymers: Composites and Nanocomposites*. 1 ed.; Springer-Verlag Berlin Heidelberg: 2013; p 426.

18. Arora, A.; Padua, G. W. *J Food Sci* **2010,** *75* (1), R43-R49.

19. (a) Sartori, C.; Finch, D. S.; Ralph, B.; Gilding, K. *Polymer* **1997,** *38* (1), 43-51; (b) Li, J. W.; He, J. M.; Huang, Y. D.; Li, D. L.; Chen, X. T. *Carbohyd Polym* **2015,** *123*, 208-216.

20. Wei, N.; Peng, X. S.; Xu, Z. P. *Acs Appl Mater Inter* **2014,** *6* (8), 5877-5883.

21. *Polysaccharides and Polyamides in the Food Industry. Properties, Production, and Patents.* 2005; p 783.

22. Pei, S. F.; Cheng, H. M. *Carbon* **2012,** *50* (9), 3210-3228.

23. Paredes, J. G. A.; Spasojevic, M.; Faas, M. M.; de Vos, P. *Frontiers in Bioengineering and Biotechnology* **2014,** *2* (26), 1-15.

24. Brunauer, S.; Deming, L. S.; Deming, W. E.; Teller, E. *J Am Chem Soc* **1940,** *62*, 1723-1732.

25. Jonquieres, A.; Fane, A. *J Appl Polym Sci* **1998,** *67* (8), 1415-1430.

26. van der Wel, G. K.; Adan, O. C. G. *Prog Org Coat* **1999,** *37* (1-2), 1-14.

27. Basu, S.; Shivhare, U. S.; Mujumdar, A. S. *Dry Technol* **2006,** *24* (8), 917-930.

28. (a) Talja, R. A.; Helen, H.; Roos, Y. H.; Jouppila, K. *Carbohyd Polym* **2007,** *67* (3), 288-295; (b) Olivas, G. I.; Barbosa-Canovas, G. V. *Lwt-Food Sci Technol* **2008,** *41* (2), 359-366.

29. Haug, A.; Smidsrod, O. *Acta Chem Scand* **1970,** *24* (3), 843-&.

30. Sun, P. Z.; Zheng, F.; Zhu, M.; Song, Z. G.; Wang, K. L.; Zhong, M. L.; Wu, D. H.; Little, R. B.; Xu, Z. P.; Zhu, H. W. *Acs Nano* **2014,** *8* (1), 850-859.

31. Persson, I. *Pure Appl Chem* **2010,** *82* (10), 1901-1917.

32. Hu, K. S.; Kulkarni, D. D.; Choi, I.; Tsukruk, V. V. *Prog Polym Sci* **2014,** *39* (11), 1934-1972.

33. Avella, M.; Di Pace, E.; Immirzi, B.; Impallomeni, G.; Malinconico, M.; Santagata, G. *Carbohyd Polym* **2007,** *69* (3), 503-511.

34. Long, F. A.; Richman, D. *J Am Chem Soc* **1960,** *82* (3), 513-519.

35. Sun, Y. M. *Polymer* **1996,** *37* (17), 3921-3928.

36. van der Zeeuw, E. A.; Sagis, L. M. C.; Koper, G. J. M. *Macromolecules* **1996,** *29* (2), 801-803.

37. Vrentas, J. S.; Jarzebski, C. M.; Duda, J. L. *Aiche J* **1975,** *21* (5), 894-901.

38. Papanu, J. S.; Soane, D. S.; Bell, A. T.; Hess, D. W. *J Appl Polym Sci* **1989,** *38* (5), 859-885.

39. Park, G. S., Transport Principles—Solution, Diffusion and Permeation in Polymer Membranes. In *Synthetic Membranes: Science, Engineering and Applications*, Bungay, P. M.; Lonsdale, H. K.; de Pinho, M. N., Eds. Springer Netherlands: 1986; pp 57-107.

40. Vilcinskas, K.; Norder, B.; Goubitz, K.; Mulder, F. M.; Koper, G. J. M.; Picken, S. J. *Macromolecules* **2015,** *48* (22), 8323-8330.

41. Park, S.; Lee, K. S.; Bozoklu, G.; Cai, W.; Nguyen, S. T.; Ruoff', R. S. *Acs Nano* **2008,** *2* (3), 572-578.

42. Bharadwaj, R. K. *Macromolecules* **2001,** *34* (26), 9189-9192.

43. de Gennes, P. G.; Prost, J., *The Physics of Liquid Crystals*. Second Edition ed.; Oxford University Press: 1995; p 347.

CHAPTER 5

COMPOSITION DEPENDENT PROPERTIES OF GRAPHENE (OXIDE)-ALGINATE BIOPOLYMER NANOCOMPOSITES

This chapter is based on:

Vilcinskas, K., Jansen, K. M. B., Mulder, F. M., Picken, S. J., Koper, G. J. M. *Composition dependent properties of graphene (oxide)-alginate biopolymer nanocomposites*. Submitted to Polymer Composites, 2016.

ABSTRACT

We report on the thermal, electrical and mechanical properties of alginate biopolymer nanocomposites prepared by solution casting with various amounts of graphene oxide (GO) or reduced graphene oxide (rGO). Our data shows that the thermal stability of alginate nanocomposites can be improved by the introduction of cross-linking through divalent metal cations, albeit that under these conditions little influence by the amount of rGO remains. On the other hand, the electrical conductivity of divalent metal ion cross-linked-rGO improves approximately 10 orders of magnitude with increasing weight fraction of rGO, whereas it declines for Sodium alginate-GO composites. In addition, storage moduli and glass to rubber transition temperatures show strong composition dependence as a consequence of complex interactions of the ions with both polymer and filler. We propose a mechanical model that allows for the accurate prediction of reinforcement by GO sheets in Sodium alginate-GO composites taking into account the orientational order of the sheets. Creep tests reveal the complex nature of multiple stress relaxation mechanisms in the nanocomposites although the stretched exponential Burgers' model accurately describes short time creep compliance.

5.1. Introduction to the properties of alginate-graphene composites

Inclusion of filler in polymer matrices yields composite materials with enhanced properties, such as improved electrical and/or thermal conductivity [1], better mechanical properties [2] or reduced gas permeation [3]. Carbonaceous nanofillers, like carbon black [4], carbon nanotubes [5], as well as graphene oxide and graphene [6], are amongst the most often used additives in designing composite materials with enriched properties. However, in order to achieve the desired improvement of the above-mentioned properties, it is crucial to ensure favorable interactions between filler and polymer phase [7]. Furthermore, it is also essential to consider other aspects such as filler functionalization, evolution of filler structure in a polymer matrix, interfacial effects and to obtain detailed structural information of composites [8].

Hydrocarbons, such as polystyrene or polypropylene, are often used for the preparation of graphene-polymer composites, however it requires functionalization of the graphene sheets in order to improve processability and reduce its propensity to agglomerate which usually compromises the optimal enhancement of properties. [9]. Recently several authors [10] have investigated the properties of bio-based polymer composites, namely Sodium alginate-graphene oxide composites. Alginates are naturally occurring copolymers comprised of alternating guluronic and mannuronic acid units, that form physical cross-links with divalent metal ions [11], and have been extensively used in the food industry as well as for pharmaceutical and medical applications [12]. Water-soluble Sodium alginate and hydrophilic graphene oxide (GO) offer a great advantage to the production of composites since both materials can be readily processed in aqueous medium. Upon drying of the composite sample, the abundance of hydroxyl groups on the Sodium alginate chains participates in the formation of the hydrogen-bonding network with carbonyl and/or epoxy groups on GO sheets [10b]. The resulting composites have shown to possess higher thermal stability [10a], increased Young's modulus [10a, 10b] and improved creep resistance [10b]. On the other hand, divalent metal ion cross-linked alginate films have useful properties, such as insolubility in water, and, as has been reported for calcium alginate films,

high storage modulus value and moderate glass transition temperature [13]. However, no attempts have been made to examine the properties of divalent metal ion cross-linked alginate-reduced graphene oxide (rGO) composites and to study the interactions between the polymer, filler and metal ions. Furthermore, to our knowledge, no studies have so far been reported to predict the reinforcing effect of GO sheets in the Sodium alginate matrix, and to model creep behavior of alginate composites of various compositions.

In this study, we set out to explore the thermal, electrical and mechanical properties of alkali earth metal ion cross-linked alginate-rGO composites, and to compare their properties to that of Sodium alginate-GO composites. In addition, we also consider composition-structure-properties aspects of the composites.

5.2. Materials and methods

5.2.1. Sample preparation

The composite samples were prepared in the experimental procedure described in Chapter 3.

5.2.2. Characterization

Thermogravimetric analysis (TGA) was conducted by using a Perkin-Elmer Thermogravimetric Analyzer TGA7 equipped with a Thermal Analysis Controller TAC 7/DX, from 25 to 400 °C (3 °C/min) under air atmosphere.

Electrical conductance of the composite samples was measured with a four-point probe device. It consisted of four equally spaced (1 mm) tips of finite radius connected to voltmeter (Keithley 2000) and ammeter (Keithley 6221). A constant voltage of 10 V was applied to the two inner tips, and an ammeter connected to the two outer tips was used to measure current through the sample. Each measurement was repeated 3 times. As the thickness of samples was significantly smaller than the spacing between the tips, the bulk resistivity ρ was obtained by following relation [14]:

$$\rho = Cd\left(\frac{V}{I}\right) \tag{5.1}$$

where: d is the thickness of the sample, V – applied voltage, I – measured current and C = 4.523 the cell constant.

The results are presented as the bulk conductivity, which is inverse of the bulk resistivity.

Dynamical mechanical thermal analysis (DMTA) was performed on a DMA Q800 (TA Instruments) instrument in a tensile mode at a frequency of 1 Hz, 5 μm amplitude, and heating rate of 3°C /min. The samples were initially conditioned at 60 °C for 30 min, then cooled and analyzed from 10-200 °C.

Creep tests were conducted on a DMA Q800 (TA Instruments) instrument at 30 °C, 40 °C, 60 °C, 80 °C and 100 °C using the same specimen as for DMTA, and applied creep stress of 4 MPa. The duration of the creep and strain recovery was 10 min and 30 min, respectively. The samples were conditioned for 5 min at each temperature before applying the load. The creep and strain recovery at 30 °C was performed twice for each sample in order to release the resulting stress, that develops during sample preparation.

5.3. Results

5.3.1. Thermogravimetric analysis

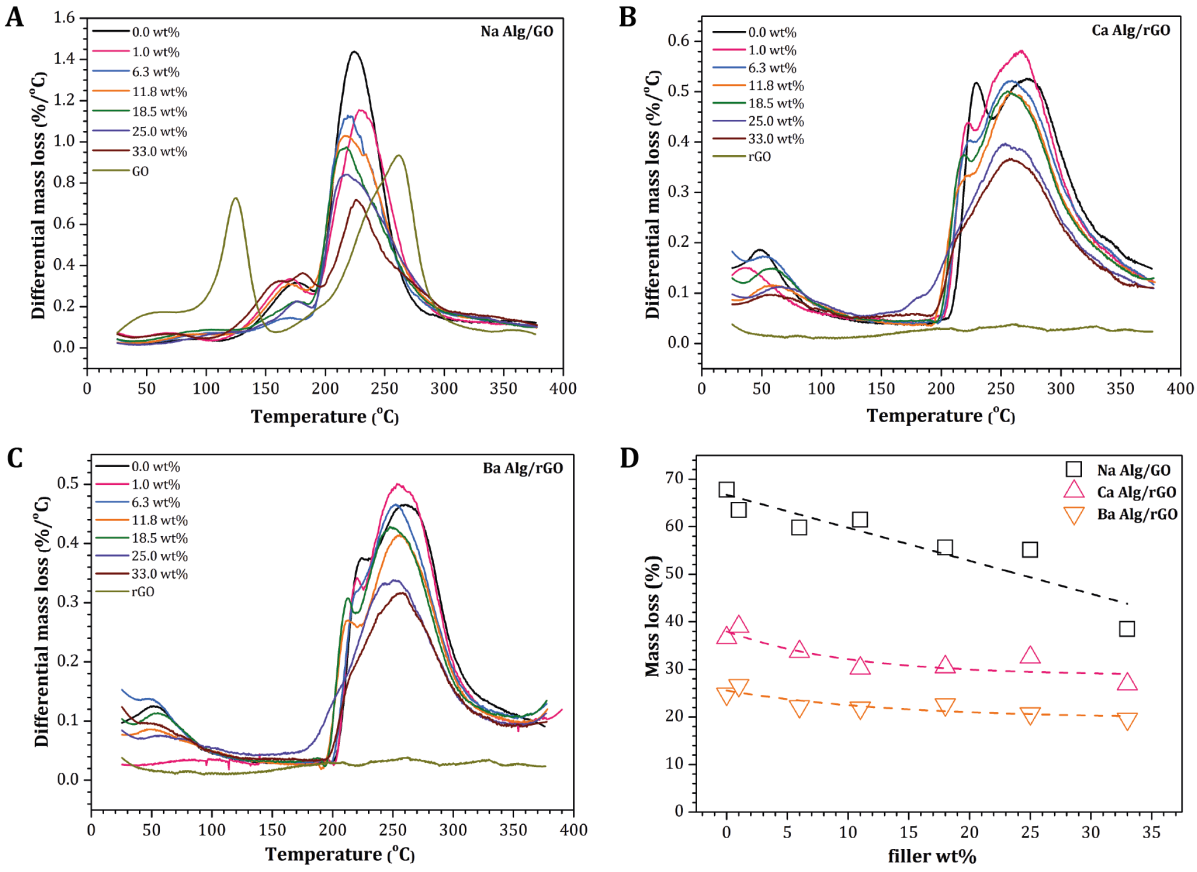

FIGURE 5.1. Differential weight loss thermograms of (A) Sodium alginate/graphene oxide (Na-Alg/GO); (B) Calcium alginate/reduced graphene oxide (Ca Alg/Gr), and (C) Barium alginate/reduced graphene oxide (Ba Alg/Gr) composites. Figure (D) gives the total relative weight loss dependence on the amount of the filler, taken at the decomposition temperature. Dashed lines serve as guides to the eye only

Figure 5.1 (A)-(C) shows the differential weight loss thermograms collected for three different types of alginate composites with varying weight fraction of filler. The initial weight loss up to 100 °C for all the samples will be due to the elimination of free water as has been found before [15].

Figure 5.1 (A) represents the differential weight loss thermogram of Sodium alginate and its composites with various weight fractions of graphene oxide (GO). Sodium alginate itself exhibits two significant weight loss peaks at ~173 °C and ~224 °C, corresponding to the loss due to decomposition into volatile components, partially with intermediate dehydration, and the decomposition of polymer into carbonaceous residue [16], respectively. As the concentration of GO increases, the Na Alg weight loss peaks shift to lower temperatures. In addition, at high weight fractions of GO (~30wt%), a new peak gradually develops at ~ 160 °C. Such changes can be explained by the hydrophilic nature of GO, where upon increasing its concentration more moisture has been trapped in the composite, thereby slightly reducing the thermal stability of Na-Alg/GO composites. Neat GO exhibits a sharp decrease in weight at ~123 °C due to the removal of moisture and decomposition of COOH groups [17]. The second weight loss peak ~260 °C can be ascribed to the removal of the remaining labile oxygen groups [18]. In addition, the absence of a weight loss peak at ~120 °C in Na-Alg/GO composites indicates interaction, presumably of a physical origin, between the carboxyl groups of GO and oxygenated groups on the polymer backbone. Indeed, the formation of an extensive hydrogen-bonding network between oxygenated groups of GO and polymer backbone has been investigated by Chen et al. [10b]

Contrary to neat GO, hydrazine reduced GO (rGO) exhibits negligible weight loss in the 25-400 °C range, which is consistent with results reported previously [17-19]. As for Sodium alginate, the thermal degradation of Calcium alginate (Ca Alg) occurs in two steps, with differential weight loss peaks observed at ~230 °C and ~270 °C. The former corresponds to dehydration [20] and the latter to decomposition of the polymer [21]. As the concentration of rGO in the polymer matrix increases, the thermal stability of the composite films somewhat reduces. This happens presumably due to the remaining hydroxyl groups at the edges of the graphene sheets upon reduction with hydrazine [17] that together with the hydrophilic groups on the alginate backbone can easily bind water molecules, hence reducing the thermal stability of the composite films.

The thermal degradation of Barium alginate also takes place in two steps within the investigated temperature range. Similarly to Calcium alginate, the weight loss peaks are observed at ~226 °C and ~260 °C, and have been ascribed to dehydration and decomposition of the polymer. Also, the peaks tend to lower temperatures upon increasing the concentration of rGO in the Barium alginate matrix.

Figure 5.1 (D) illustrates the total weight loss dependence on filler concentration for the various composite systems as obtained at the decomposition temperature (the decomposition temperature is taken to be the center of the highest temperature peak in the thermogram.) As discussed before, Na-Alg/GO composites exhibit the most significant weight loss in comparison to the alkali earth metal ion cross-linked-rGO composites. Upon inclusion of GO sheets, the weight loss of Sodium alginate composites decreases with a near linear dependence on filler weight fraction. This suggests, that the major mass loss of the composite films occurs due to the decomposition of the polymer only. For instance, the experimentally measured mass loss of Na-Alg/GO with 11.8 wt% of GO is 61.4%, and assuming a constant polymer mass loss as obtained for the pure system, the calculated value is found to be 60.3%. The weight loss of an alkali metal ion cross-linked sample is significantly reduced, and varies only slightly with the concentration of graphene. Also here, the major weight loss originates from the decomposition of the polymer. The reduction in observed mass loss is the result of the cross-linking.

5.3.2. Electrical conductivity

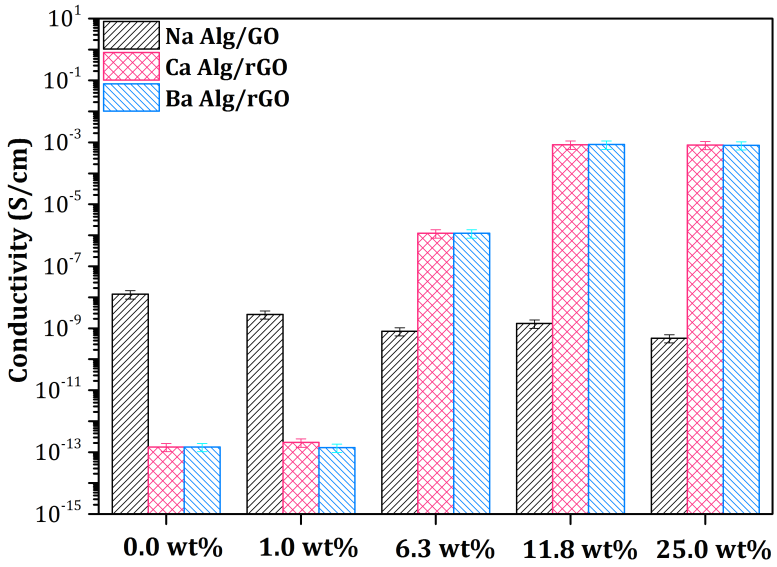

FIGURE 5.2. Electrical conductivity of alginate composites versus the weight fraction of filler.

Figure 5.2 illustrates the electrical conductivity of different alginate composites with various weight fractions of filler. As seen in the graph, the pure alginates are good insulators and their insulating properties further increase upon cross-linking with divalent metal ions and addition of GO. With increasing weight fraction of GO, the electrical conductivity of Na-Alg/GO decreased about 1 order of magnitude compared to neat Sodium alginate due to the good insulating properties of GO [22]. On the other hand, the electrical conductivity significantly improves with reduction of GO. As seen in Figure 5.2, the electrical conductivity of divalent metal ion cross-linked alginate-rGO composites increases by approximately 10 orders of magnitude and levels off beyond 12 wt% of rGO. However, it still remains several orders of magnitude lower than previously reported for other composite systems, even with much lower weight fractions of filler [23]. Although, it has been proposed that cross-linking alginate with Calcium facilitates distribution of graphite into hydrogel matrix thereby promoting electrical conductivity [24], our results suggest that divalent metal ion-polymer, divalent metal ion-rGO, and rGO-divalent metal ion-polymer interactions, preclude the formation of a connected graphene network that is required to establish effective conductive paths as explained by

the classical percolation theory [25]. We further discuss filler-polymer interactions in the Discussion section.

5.3.3. Mechanical properties

Figure 5.3 (A)-(C) shows DMTA results obtained for various types of alginate films with varying concentrations of filler. Figure 5.3 (D) summarizes the filler concentration dependence of the storage modulus for the three composite systems at the temperature of 30 °C. Even without addition of filler, the neat polymers exhibit remarkably high storage modulus values that agree with values previously reported for Sodium alginate [26] and Calcium alginate [13]. As the amount of GO in the Sodium alginate composite increases, so does the storage modulus, albeit not at very high weight fractions of GO. Alkali earth metal ion cross-linked alginates and their composites exhibit more dramatic changes in storage modulus values for different weight fractions of reduced graphene oxide. Upon inclusion of rGO, the stiffness of Calcium alginate composites initially decreases significantly only to recover and reach a maximum stiffness at 11.80 wt % of rGO, albeit still lower than that of the neat polymer. Conversely, Ba-Alg/rGO composites with increasing graphene content show improved stiffness, which decreases beyond 18.50 wt% of rGO.

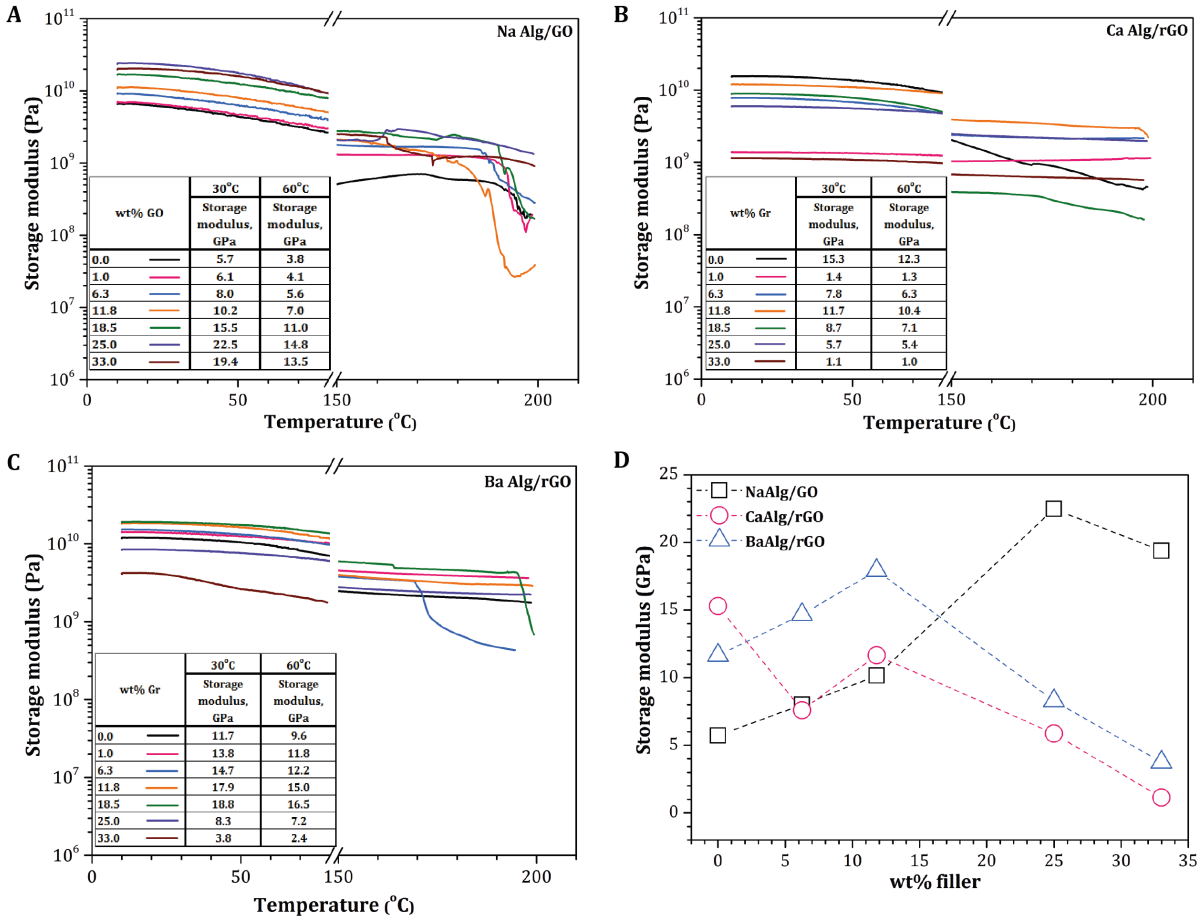

FIGURE 5.3. Storage modulus values for composite films of (A) Na-Alg/GO, (B), Ca-Alg/rGO, (C) Ba-Alg/rGO and (D) its dependence on filler concentration for various types of alginates at 30 °C. Dashed lines serve as guides to the eye only.

In addition, we have attempted to determine the glass transition temperature T_g of the different alginate composite systems using the loss modulus as obtained from DMTA measurements and presented in Figure 5.4. Unfortunately, due the absence of a well-defined loss modulus peak for Sodium alginate and its composites, we have not been able to accurately determine the glass transition temperature. We point out that all our composite systems contain ~30wt% glycerol as a plasticizer, which substantially reduces the molecular friction between Sodium alginate chains. For the Sodium alginates composites, this probably shifts the T_g values to a temperature out of the experimental window. Barium and Calcium alginate composite systems, however, are cross-linked and therefore yield distinct loss modulus peaks as seen in Figure 5.4 (A)-(B.)

Figure 5.4 (C)-(D) illustrates the glass transition temperatures of different families of cross-linked alginates. They exhibit varying dependence on the amount of graphene. With increasing amount of filler, the T_g for Ca-Alg/rGO composites slightly increases, suggesting reduced chain mobility upon inclusion of filler. In contrast, Ba-Alg/rGO composites show a relatively constant T_g independent of the amount of graphene, indicating little or no effect on the mobility of the polymer chains.

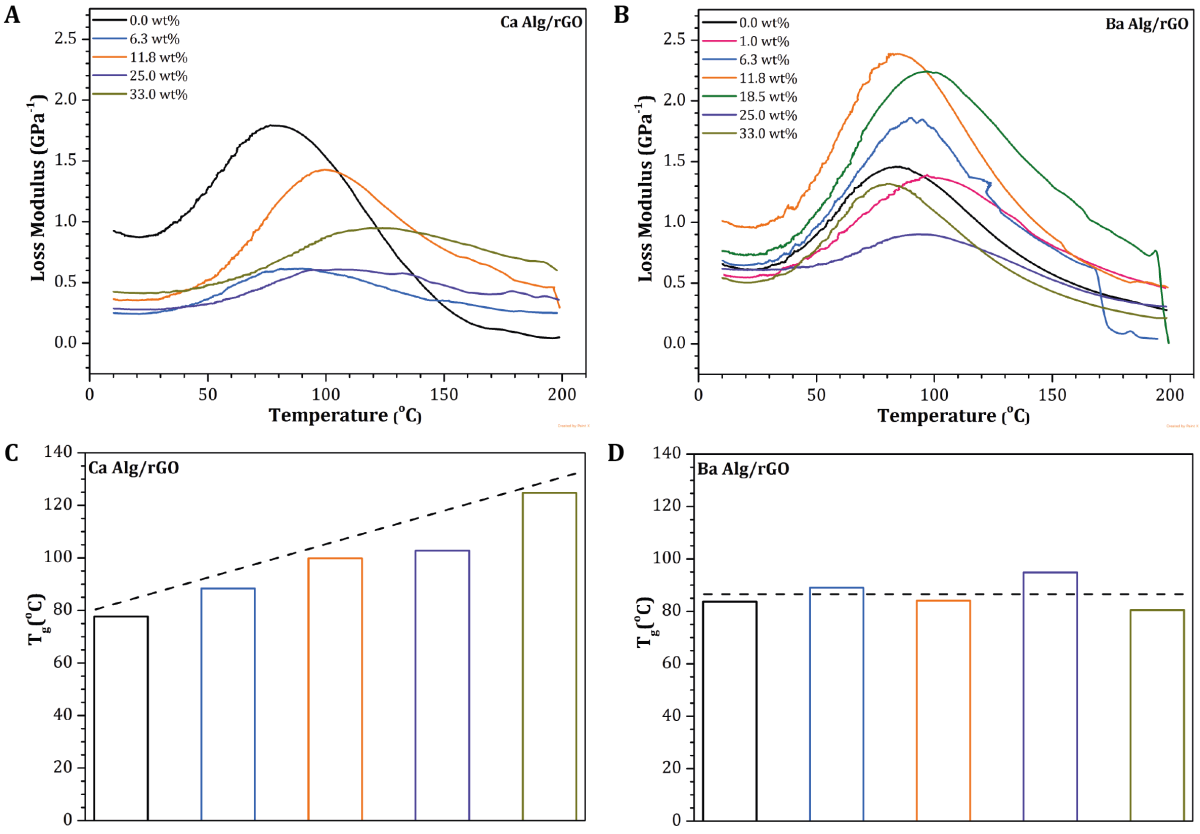

FIGURE 5.4. Loss modulus at $1s^{-1}$ versus temperature curves for (A) Ca-Alg/rGO and (B) Ba-Alg/rGO composites. Glass transition temperatures, as determined from the peak of loss modulus, for various compositions of (C) Ca-Alg/rGO and (D) Ba-Alg/rGO composites. Different colors represent different compositions as indicated in the graphs (A) and (B). Dashed lines serve as guides to the eye only.

5.3.4. Creep tests

In order to gain more information about the load performance of the different types of alginates and their composite systems, we have conducted creep tests as described in the experimental part.

Figure 5.5 displays the creep compliance, being the observed strain over the exerted stress, and strain recovery of Na-Alg/GO, Ca-Alg/rGO and Ba-Alg/rGO composite systems at 60 °C.

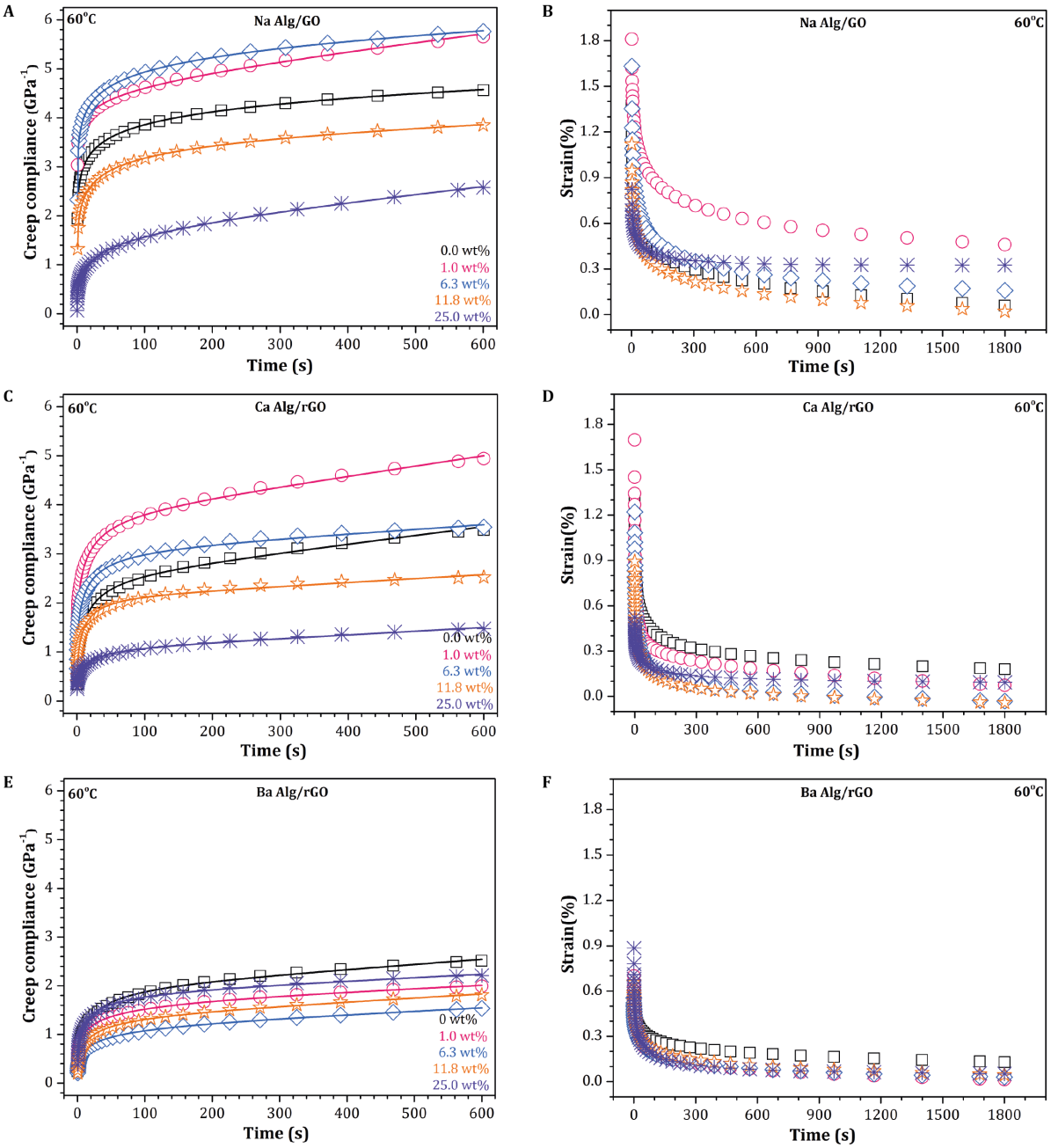

FIGURE 5.5. Creep compliance and strain recovery for (A,B) Na-Alg/GO, (C,D) Ca-Alg/rGO, and (E,F) Ba-Alg/rGO composites. Lines are fits by a modified Burgers' four-element model, see text.

Of the three different alginate composite systems, the Na-Alg/GO system reveals the poorest creep resistance. At low (1 wt%) and moderate (~6 wt%) weight fractions of GO, the samples demonstrate

lower creep resistance compared to the unfilled polymer. However, the load bearing of Na-Alg/GO composites improves at higher weight fractions, above about 11 wt%, of filler. Unlike Na-Alg/GO composites, both earth-alkali metal ion cross-linked alginate composites exhibit complex filler weight dependence, see Figure 5.4 (D)-(F).

Since all creep compliance curves largely exhibit a viscoelastic nature of the samples, we have used Burgers' four-element model to describe the behavior. The model, see Eq. (5.2), is represented by an elastic element (spring) representing the instantaneous creep and a viscous element (dashpot) to represent the irrecoverable creep, J_0 and J_2 respectively in Eq. (5.2). This series network is connected to a Kelvin-Voigt element (spring and dashpot in parallel) to represent the actual creep. This creep response is usually more complex than can be described by a simple Kelvin-Voigt system as usually polymers and their composites possess a spectrum of relaxation times [27]. To account for this, we have used a modified Burgers' model, where the exponential term, with coefficient J_1, is replaced by a stretched exponential term with an exponent n to account for the dispersion. The same model has successfully been used to accurately describe creep compliance of the polyimide PMR-15 [28] and bismaleimide-clay nanocomposites [29]. Hence, the creep compliance $J(t)$ as a function of time t can be expressed as

$$J(t) = J_0 + J_1\left[1 - \exp\left(-\left(\frac{t}{\tau}\right)^n\right)\right] + J_2 t \qquad (5.2)$$

We used the storage modulus values derived from the dynamical mechanical thermal analysis at a representative temperature for the instantaneous creep compliance J_0 as this represents the response at small time scales, i.e. at 1 s^{-1}. The irrecoverable compliance J_2 describes the permanent deformation of the sample, on the molecular level regarded as the slip of polymer chains relative to each other, and is expected to have a relative low value. The effective retardation time τ, corresponds to the time required for the macromolecular matrix to rearrange. The stretching

exponent *n* accounts for the distribution of relaxation times and assumes values between 0 and 1. A value of unity represents a single relaxation time whereas a lower value of *n* indicates a wider distribution of relaxation times [30]. As shown in Figure 5.5, the modified Burgers' model can be fit to the data with excellent accuracy using only four free variables. The obtained values for Na-Alg/GO, Ca-Alg/rGO and Ba-Alg/rGO composite systems at 60 °C are presented in the Table 5.1.

TABLE 5.1. The obtained parameters for the modified Burgers' model for different alginate composite systems at 60 °C, see also Figure 5.4.

Composition		J_0	J_1	τ	n	J_2
Polymer	*Filler (wt%)*	*(GPa^{-1})*	*(GPa^{-1})*	*(s)*		*($TPa^{-1}s^{-1}$)*
Na-Alg/GO	0.0	0.27	4.8	22.7	0.20	0.32
	1.0	0.24	5.1	2.2	0.14	1.50
	6.3	0.18	6.2	13.7	0.17	0.47
	11.8	0.14	3.7	14.7	0.26	0.48
	25.0	0.07	1.8	35.5	0.39	1.50
Ca-Alg/rGO	0.0	0.081	2.5	13.2	0.45	1.60
	1.0	0.76	3.0	9.7	0.44	2.00
	6.3	0.16	2.9	7.6	0.40	0.91
	11.8	0.01	2.1	8.7	0.44	0.67
	25.0	0.19	0.9	16.5	0.47	0.67
Ba-Alg/rGO	0.0	0.10	1.8	16.7	0.48	1.10
	1.0	0.09	1.6	15.8	0.36	0.60
	6.3	0.08	1.1	21.8	0.42	0.66
	11.8	0.07	1.3	15.7	0.44	0.80
	25.0	0.14	1.7	11.2	0.43	0.69

Finally, we have attempted to predict the long-term creep behavior of Calcium and Barium alginate-rGO composites at 60°C by applying the time-temperature superposition principle [31], whereby

viscoelastic data at one temperature can be transformed to that of a different temperature by shifting it along the time axis. The master curves and shift factors for different families of alginate composites are presented in Figure 5.6.

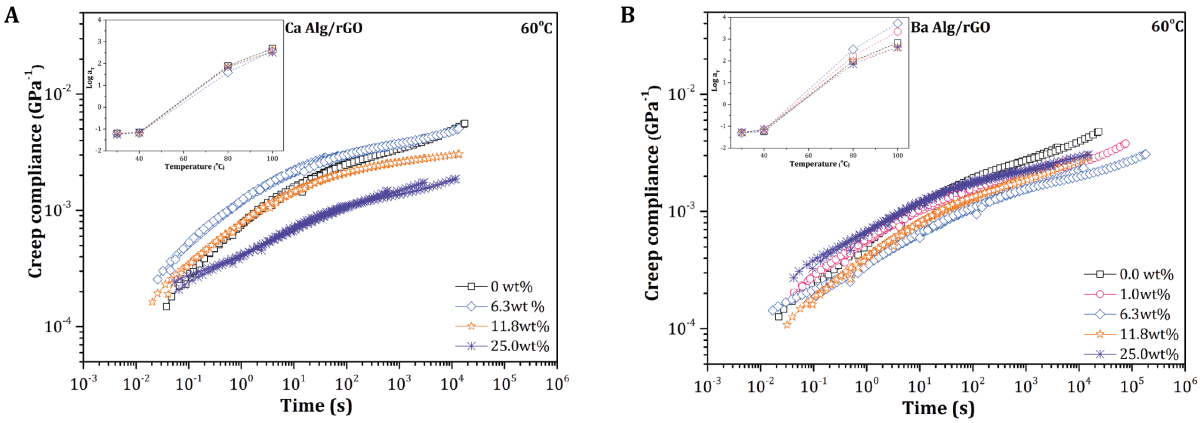

FIGURE 5.6. Master curves of creep compliance versus scaled time for (A) Calcium alginate and its composites, and (B) Barium alginate and its composites at 60°C. The insets show the shift factors used in the scaling.

It is apparent that inclusion of rGO sheets improves the long-term creep behavior for both composite systems. Additionally, the slopes of the master curves of the composites are slightly lower, suggesting a small reduction in the creep rates. However, the non-monotonous improvement of the long-term creep compliance illustrates the complexity of the undergoing processes during creep.

5.4. Discussion

In the following we shall compare the two classes of alginate composites that can be distinguished on whether or not the alginate matrix is cross-linked or not.

5.4.1. Na-Alg/GO composites

Within the explored temperature regime the thermal stability of the alginate films appears to be largely independent of filler. Changes in mass loss follow the reduction of the amount of polymer

only, see Figure 5.2 (D) and the associated discussion. A notable observation, though, is the disappearance of the GO mass loss due to dehydration, around 120 °C as shown in Figure 5.2 (A), which does signify hydrogen-bonding based interactions between oxygenated groups of GO and alginate. Electrical conductivity of Na-Alg/GO composites, on the other hand, exhibits some filler concentration dependence. The level of insulation of the composites slightly improves at higher weight fractions of GO.

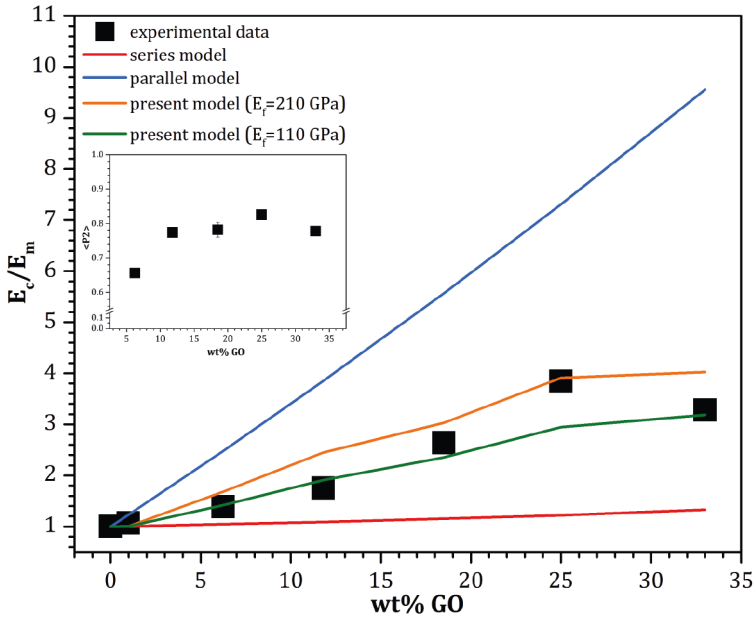

FIGURE 5.7. Predicted and measured reinforcement of Na Alg by GO as a function of filler weight fraction. The inset shows the order parameter $\langle P_2 \rangle$ as a function of GO concentration. The reinforcement is taken to be the elastic modulus of the composite material relative to the elastic modulus of the polymer matrix (data from Fig. 5.3 D).

Likewise, the reinforcement, i.e. the elastic moduli ratio E_c/E_m of composite material relative to its polymer, of the Sodium alginate matrix by introduction of GO sheets indicates moderate interactions between filler and polymer as the reinforcement varies with the filler amount, see Figure 5.3 (D). In order to quantify this effect we have invoked the Takayanagi models as discussed in detail by Sperling [7]. The original model has been derived to estimate the stiffness of multiphase polymers

such as polymer blends. It has been demonstrated earlier that the model also adequately describes polymer composite materials [32]. In the latter case, the mechanical response of the composite depends on the stiffness of the polymer matrix, E_m, and of the filler, E_f, as well as on its volume fraction, ϕ_f. We argue that the orientation of the GO sheets in the polymer matrix also matters. In the present experiments, the deformation takes place in the length direction of the film, perpendicular to the film normal. In the case of randomly oriented GO sheets in the Sodium alginate matrix, the stress transfer from the polymer matrix to the GO sheets upon deformation perpendicular to the layer normal of the sample will be inadequate, resulting in the lowest possible reinforcing effect, represented by the series model, Eq. 5.3, and graphically shown in Figure 5.7 (red line). On the other hand, the load transfer in a composite with perfectly aligned GO sheets will be optimal, yielding the highest reinforcing effect; shown as the parallel model, Eq. 5.4, in Figure 5.7 (blue line). These two cases cannot accurately describe the actual reinforcement for partially aligned filler but rather serve as extremes.

$$E_{\perp} = \left[\frac{\phi_f}{E_f} + \frac{\left(1-\phi_f\right)}{E_m} \right]^{-1} \quad \text{(Series model)} \tag{5.3}$$

$$E_{II} = \phi_f E_f + \left(1-\phi_f\right) E_m \quad \text{(Parallel model)} \tag{5.4}$$

$$E_c = \left[\frac{\langle P_2 \rangle}{E_{II}} + \frac{\left(1-\langle P_2 \rangle\right)}{E_{\perp}} \right]^{-1} \quad \text{(Present model)} \tag{5.5}$$

We have recently reported [33] that GO sheets show high orientational order in the Sodium alginate matrix, that would undoubtedly influence the composite stiffness in the axial direction. Therefore we have attempted to fit our data with a mechanical model that provides the relation between the stiffness of the polymer matrix and composite material, and depends on the average orientational order of GO sheets inside the polymer matrix, shown as the curves labeled 'present model' in

Figure 5.7. The inset shows the measured order parameter values, $\langle P_2 \rangle$, as a function of GO concentration. The stiffness of the composite material was estimated by using Equation 5.5, a similar expression was originally derived to predict stiffness of a highly oriented aramid fiber [34]. As can be seen in Figure 5.7 (yellow and green lines), the model adequately describes the reinforcing effect of oriented GO sheets inside the Sodium alginate matrix taking into account the variation of order parameter. The stiffening effect is present up to 25wt% of GO, beyond which both the reinforcement and the order begin to decrease due to jamming effects of neighboring GO sheets. In addition, the reinforcement also depends on the stiffness of GO sheet, which we have taken to be 210 GPa [35]. However, it is not unreasonable to assume that harsh graphite oxidation reaction conditions can produce defects, such as holes, inside GO sheets, that, in turn, influence the stiffness of GO sheets. In addition, the stress transfer of multilayered GO sheets is expected to be inferior to mono/bi-layer GO due to sliding of the sheets past each other, as has been reported to be the case for graphene-polymer nanocomposites [36]. Therefore, we included the curve for a GO stiffness of 110 GPa, which provides a lower bound for the measured reinforcement values.

The lower creep resistance of the samples containing low and moderate weight fractions of GO, see Figure 5.5 (A)-(B), can be explained by the slight stacking of GO sheets and weakness of the network formed by the GO sheets due to the consequently larger distance between the stacks than what could be realized by homogenously distributed sheets. As such, it supports the hypothesis of relatively strong hydrogen bonding based polymer-filler interactions. In order to estimate the average stack size, we used our previously calculated interlayer distance between GO sheets for various compositions of Na-Alg/GO composites [33]. The average GO stack size is found using the Scherrer equation [37]. This number is subsequently divided by the interlayer spacing of GO to yield the average number *N* of GO sheets per stack. As seen in Figure 5.8 (A), there are already agglomerates at low weight fractions of sheets. We note, however, that assessment of the average GO stack size at greater weight fractions of the filler can be less accurate due to the lateral inclusion of the sheets, which broadens, and sometimes skews, the diffraction peak, therefore reducing the

obtained average number of sheets per stack. As presented in Figure 5.8 (A), *N* tends to higher values with increasing weight fraction of GO, however does not do so monotonously for reasons discussed earlier. At higher filler weight fractions, the stress distribution improves due to the formation of a network between GO aggregates that compensates for the effect of further increment of *N*.

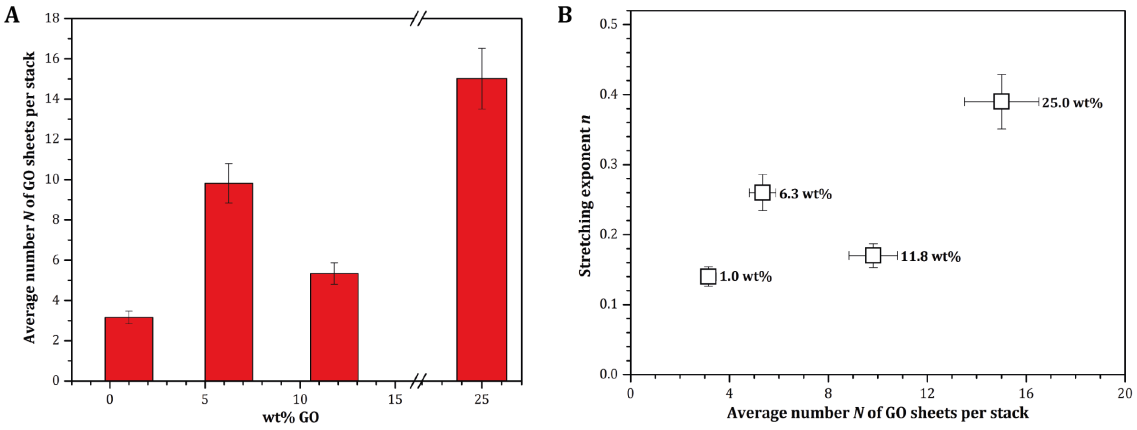

FIGURE 5.8. (A) Average number, *N,* of GO sheets per stack depending on the weight fraction of the filler. (B) Stretching exponent versus average number *N* of GO sheets per stack.

The behavior of the creep resistance in Figure 5.5 (A)-(B) is reflected by the parameter values obtained from a fit with the modified Burgers' model, see Table 5.1. For instance, with increasing GO concentration the creep retardation time τ initially sharply decreases to slowly increase with filler concentration. At 25 wt% of filler it exceeds that of the neat polymer. The stretching exponent *n* shows the same trend, initially it diminishes to increase at higher weight fractions of GO. The same tendency is also present in the creep compliance, J_1, values. Such consistent variation of parameters suggests that at low weight fractions of GO, the polymer chains gain more mobility due to the introduction of the sheets and the frailty of their network that does not build up to expectation due to stacking. Upon further increment of the filler concentration, the mobility of the chains begins to decrease due to the higher concentration of aggregates, forming a robust network. As shown in Figure 5.8 (B), it appears that the stretching exponent *n* depends on the average number *N* of GO

sheets in a stack. It increases with increasing *N*, indicating that the distribution of relaxation times is reduced upon strong introduction of GO sheets that reduces polymer chain mobility. Indeed, the formation of a hydrogen-bonding network between oxygenated groups of the polymer and GO sheets further decreases polymer chain mobility.

In summary, the thermomechanical behavior of Na-Alg/GO composites can be understood from the modification of the polymer-polymer interactions by introduction of the polymer-filler interactions. Our data suggests that after oxidation, graphene sheets possess high surface energy that results in strong filler-filler interactions that lead to incomplete dispersion of GO sheets. On the other hand, the plentiful of oxygenated groups on alginate chains and GO sheets ensures the formation of extensive hydrogen-bonding network that is strong enough to fully integrate the filler aggregates into the polymer.

5.4.2. Alkali metal cross-linked alginate films

Where for Na-Alg/GO composites there are only three kinds of interactions to consider, namely filler-filler, polymer-polymer and polymer-filler, the situation for cross-linked alginate-rGO complexes is much more involved. We will argue that for the cross-linked films the observed changes in stiffness and glass transition temperature are caused by competing reactions between the polymer, the sp^2 clusters and carboxyl groups of the graphene sheets and the alkali earth metal ion during the ion exchange reaction of Na-Alg/GO films. First of all, it has been reported that different multivalent metal ions exhibit different affinity to the alginate matrix [38], namely that Barium ions associate easier with the oxygenated groups on the alginate backbone than Calcium ions do. Indeed, Fourier Transform Infrared Spectroscopy of divalent metal ion cross-linked alginates revealed more specific interactions with Barium ions compared to Calcium ions [39]. In addition, it has been shown that different divalent metal ions binds have preferential binding sites to the oxygenated groups of alginate such as that Barium ions preferentially associate with guluronic-guluronic acid and mannuronic-mannuronic acid blocks, whereas Calcium-to guluronic-guluronic and

mannuronic-guluronic acid blocks [40]. However, it appears that the bonds between divalent metal ions and oxygenated groups of alginates are of dynamic origin as they undergo bond breakage and reformation even under small stress [41]. Secondly, both Barium and Calcium ions interact with sp^2 clusters on reduced graphene oxide sheets via cation-π interactions as discussed by Sun et al. [42]. The authors of this study have shown that metal ions intercalate between graphene sheets, bind to them at different positions with a binding energy that is higher for Barium ions than for Calcium ions. Furthermore, it has been reported that divalent metal ions can also bridge between adjacent GO sheets [43]. We would like to reiterate that we conduct the ion exchange reaction of Na-Alg/GO composites with divalent metal ion salt solutions, and subsequently reduce the metal ion cross-linked/GO composite films in the aqueous hydrazine solution. Thus, it is highly likely that divalent metal ions also form rGO-metal ion-polymer junctions together with rGO-metal ion-rGO interactions. As reduction of GO with hydrazine only eliminate epoxy and hydroxyl groups [44], the carboxyl groups remain unaffected, and hence the connections between graphene sheets, divalent metal ions and polymer backbone persist as manifested in the insolubility of cross-linked composite samples.

Based on the above information and experimental evidence, we argue that the higher affinity of Barium ions for the polymer and filler sheets improves the stress distribution in the Ba-Alg/rGO composites as manifested by the higher storage modulus values in comparison with Ca-Alg/rGO composites. At high weight fractions of filler, however, the load distribution for both composite systems appears to be impaired, presumably due to the jamming effects of filler sheets. In addition, the orientational order of rGO sheets in the divalent metal ion cross-linked alginates appears to be impaired after the ion-exchange reaction and the reduction of filler sheets in aqueous hydrazine solution since otherwise the modulus would increase with increasing weight fraction of filler as discussed in the preceding paragraph. Indeed, 2D XRD images of the divalent metal ion cross-linked alginate/rGO composites showed decreased intensity of anisotropic scattering by the filler sheets perpendicular to the layer normal of the samples [33]. In order to understand the changes that affect

the final properties of such composites, a further investigation is required. X-ray diffraction (XRD) patterns of Ca-Alg/rGO composites revealed an amorphous structure, whereas those of Ba-Alg/rGO composites indicated the presence of a semi-crystalline structure and of the formation of incommensurately modulated structures upon inclusion of graphene [33]. As seen in figure 5.4 (C)-(D), unfilled Barium alginate possesses higher T_g temperature than Ca Alg, which agrees with XRD data. We, therefore, propose that the semi-crystalline structure of Barium alginate arises due to the preferential binding of Barium ions to mannuronic acid blocks that enable these junctions to attain more linear conformation whereas guluronic acid-Barium junctions retain more folded structure, see the reference [40] for the schematic illustration.

With increasing weight fraction of graphene, however, the alginate chain mobility appears to be reduced in the Ca-Alg/rGO composite system, whereas it remains constant for Ba-Alg/rGO composites. Such distinctive behavior could be attributed to the different interactions between the constituents of the composites. We suggest that in Ca-Alg/rGO composites there are more Calcium mediated polymer-rGO junctions, which grow in number with increasing amount of filler, than there are Calcium mediated polymer-polymer junctions as well as rGO-rGO junctions, thus reducing polymer chain mobility. On the other hand, in the Ba-Alg/rGO composite family it appears to be more separate rGO-Ba^{2+}-rGO and polymer-Ba^{2+}-polymer junctions that result in the development of a two-phase system with increasing amount of rGO. Such an interpretation agrees with our experimental finding of the development of a periodic structure as observed in XRD experiments, measured electrical conductivity, and of the invariability of T_g. Indeed, the presence of divalent ions in the discussed structural arrangements of divalent metal ion cross-linked-rGO composites should be responsible for the high percolation threshold and mediocre electrical conductivity properties of the composite films.

The non-monotonous behavior of creep compliance and strain recovery for the cross-linked alginate composites as illustrated in Figures 5.5 (C)-(F), manifests the complexity of interactions between the

constituents. As mentioned earlier, ionically cross-linked divalent metal alginate junctions undergo ionic bond breakage and reformation under stress [41]. This partial de-cross-linking of an ionically cross-linked junction begins at low stress levels, efficiently dissipating the force. Subsequent increase in the stress, initiates partial de-cross-linking of a neighboring junction, in this way preventing from complete collapse of cross-linked blocks. Our findings suggest that both Calcium and Barium alginates dissipate deformation energy in a similar manner, albeit that Barium alginate possesses slightly better creep resistance that can be attributed to the higher affinity of Barium ions as discussed above. However, stress relaxation mechanisms of divalent metal ion cross-linked alginates-rGO composites are more intricate. As introduced earlier, the bridging of GO sheets with divalent metal ions lead to the enhancement of mechanical properties [43]. Upon bridging two adjacent GO sheets in-plane, the resistance to deformation along the layer normal has been shown to improve. On the other hand, if divalent metal ions both bridge adjacent GO sheets and are intercalated between them, the deformation mechanism has been reported to become more complicated, and metal ion size-dependent. Since in our experimental procedure we do not have control over binding sites of divalent metal ions, their interaction with polymer chains and, especially, with GO sheets, can result in variety of possible structural arrangements that, in turn, seem to result in difficult-to-predict trends in the creep compliance curves.

The complexity of stress relaxation mechanisms in divalent metal ion cross-linked alginates and their composites is reflected in the fit parameters presented in Table 5.1. For both the metal ion cross-linked systems, the stretch exponent increases, indicating a narrower distribution of relaxation times, as a result of cross-links. In addition to this, the retardation time τ for various compositions of metal ion cross-linked alginates increases in comparison with Sodium alginate composites. Furthermore, depressed creep compliance J_1 values corroborate reduced polymer chain mobility. However, both alkali earth metal ion cross-linked alginates show a complicated rGO concentration dependence indicating complex interactions that may be difficult to decouple.

In effect, introduction of divalent metal cations in alginate-rGO composites significantly alters polymer-polymer, polymer-filler, and filler-filler interactions. Our data shows that these interactions are strongly influenced by the affinity of metal ions to oxygenated groups of alginate chains as well as filler sheets. Depending on the nature of the metal cation and the filler weight fraction, the interactions between the polymer and filler can be rendered to be stronger as in the case of Ba-Alg/rGO composites, or weaker as for Ca-Alg/rGO composites. However, in order to determine the precise interactions between the constituents of divalent metal ion cross-linked alginate-graphene composites, our present data is insufficient, and a more detailed study will be required.

5.5. Conclusions

We have investigated thermal, electrical and mechanical properties of graphene (oxide)-alginate biopolymer nanocomposites and have shown these to be composition dependent. Thermogravimetric data analysis revealed favorable interactions between GO and Sodium alginate polymer chains. However, thermal stability of Na-Alg/GO composites showed no dependence of the filler weight fraction, and was slightly inferior to that of the unfilled polymer due to the hygroscopic nature GO sheets. On the other hand, upon introduction of cross-linking junctions in alginate-graphene nanocomposites thermal stability was improved, though not influenced by the presence of rGO sheets.

On the other hand, the electrical properties appeared to be composition dependent. Whereas electrical conductivity of Na-Alg/GO composites decreased with increasing amount of GO, the electrical conductivity of divalent metal ion cross-linked alginate-rGO composites improved about 10 orders of magnitude. However, the measured values remained several orders of magnitude lower than of other rGO-polymer composites due to the ineffective formation of a percolated conductive network of filler particles.

Similarly, the mechanical properties and the glass transition temperature of alginate-(reduced) graphene oxide nanocomposites are strongly affected by composition in particular the weight

fraction of filler. The favorable interactions between GO and Sodium alginate polymer chains as well as orientational order of the filler particles manifests itself in a dramatic increase of the storage modulus of the composites. In addition, the reinforcing effect of GO was modeled by taking into account the orientational order of sheets and yielded accurate description of the experimental data. On the other hand, the properties of alkali earth metal ion cross-linked alginate-rGO nanocomposites were strongly influenced by the divalent metal ion. Our experimental results show the formation of dissimilar microscopic structures that in a complex way influence the electrical conductivity, the elastic modulus of the nanocomposites, and the mobility of the polymer chains, which we believe is due to the specific interactions between polymer chains, filler sheets and metal cations. The lack of clear trends in the creep compliance data of different alginate nanocomposites indicates complex stress relaxation mechanisms. Nevertheless, the modified stretched exponential Burgers' model can describe the short-term creep compliance of alginate-graphene (oxide) composites with remarkable precision.

Our study clearly indicates that graphene (oxide) filled alginates form an extremely versatile class of composites that can be tuned at will from hydrophilic to hydrophobic with concurrent variation in electrical conductivity, thermomechanical strength and elastic properties. Many of these phenomena, such as its hydrophobicity, can be understood from relatively simple considerations whereas others, such as the elastic response, still remain elusive largely due to the intricate interplay between filler-alginate-multivalent ion interactions.

Acknowledgements

We acknowledge dr. M. R. Hegde and B. Norder for fruitful discussions, P.J. Droppert – for the assistance with the electrical conductivity measurements, and H. Broekhuizen – for the assistance with the DMA instrument.

5.6. References

1. Du, Y.; Shen, S. Z.; Cai, K. F.; Casey, P. S. *Prog Polym Sci* **2012,** *37* (6), 820-841.

2. Kango, S.; Kalia, S.; Celli, A.; Njuguna, J.; Habibi, Y.; Kumar, R. *Prog Polym Sci* **2013,** *38* (8), 1232-1261.

3. Choudalakis, G.; Gotsis, A. D. *Eur Polym J* **2009,** *45* (4), 967-984.

4. Roy, N.; Sengupta, R.; Bhowmick, A. K. *Prog Polym Sci* **2012,** *37* (6), 781-819.

5. Huang, Y. Y.; Terentjev, E. M. *Polymers-Basel* **2012,** *4* (1), 275-295.

6. Huang, X.; Qi, X. Y.; Boey, F.; Zhang, H. *Chem Soc Rev* **2012,** *41* (2), 666-686.

7. Sperling, L. H., *Introduction to Physical Polymer Science*. 4th ed.; John Wiley & Sons, Inc.: 2006; p 880.

8. Ganesan, V. *J Polym Sci Pol Phys* **2008,** *46* (24), 2666-2671.

9. Kuila, T.; Bose, S.; Mishra, A. K.; Khanra, P.; Kim, N. H.; Lee, J. H. *Prog Mater Sci* **2012,** *57* (7), 1061-1105.

10. (a) Ionita, M.; Pandele, M. A.; Iovu, H. *Carbohyd Polym* **2013,** *94* (1), 339-344; (b) Chen, K.; Shi, B.; Yue, Y. H.; Qi, J. J.; Guo, L. *Acs Nano* **2015,** *9* (8), 8165-8175; (c) Cao, K. T.; Jiang, Z. Y.; Zhao, J.; Zhao, C. H.; Gao, C. Y.; Pan, F. S.; Wang, B. Y.; Cao, X. Z.; Yang, J. *J Membrane Sci* **2014,** *469*, 272-283.

11. Grant, G. T.; Morris, E. R.; Rees, D. A.; Smith, P. J. C.; Thom, D. *FEBS Letters* **1973,** *32* (1), 195-198.

12. Pawar, S. N.; Edgar, K. J. *Biomaterials* **2012,** *33* (11), 3279-3305.

13. Russo, R.; Malinconico, M.; Santagata, G. *Biomacromolecules* **2007,** *8* (10), 3193-3197.

14. Smits, F. M. *Bell System Technical Journal* **1958,** *37* (3), 711-718.

15. Hatakeyama, T.; Hatakeyamaa, H.; Nakamurab, K. *Thermochimica Acta* **1995,** *252*, 137–148.

16. (a) Soares, J. P.; Santos, J. E.; Chierice, G. O.; Cavalheiro, G. O. *Eclética Quimíca* **2004,** *29* (2), 53-56; (b) Swamy, T. M. M.; Ramaraj, B.; Siddaramaiah *J Macromol Sci A* **2010,** *47* (9), 877-881.

17. Pei, S. F.; Cheng, H. M. *Carbon* **2012,** *50* (9), 3210-3228.

18. Park, S.; An, J.; Potts, J. R.; Velamakanni, A.; Murali, S.; Ruoff, R. S. *Carbon* **2011,** *49* (9), 3019-3023.

19. Wu, N.; She, X. L.; Yang, D. J.; Wu, X. F.; Su, F. B.; Chen, Y. F. *J Mater Chem* **2012,** *22* (33), 17254-17261.

20. Zhang, J. J.; Ji, Q.; Wang, F. J.; Tan, L. W.; Xia, Y. Z. *Polym Degrad Stabil* **2012,** *97* (6), 1034-1040.

21. Bekin, S.; Sarmad, S.; Gurkan, K.; Yenici, G.; Keceli, G.; Gurdag, G. *Polym Eng Sci* **2014,** *54* (6), 1372-1382.

22. Gomez-Navarro, C.; Weitz, R. T.; Bittner, A. M.; Scolari, M.; Mews, A.; Burghard, M.; Kern, K. *Nano Lett* **2007,** *7* (11), 3499-3503.

23. (a) Wang, X. L.; Bai, H.; Yao, Z. Y.; Liu, A. R.; Shi, G. Q. *J Mater Chem* **2010,** *20* (41), 9032-9036; (b) Pang, H.; Chen, T.; Zhang, G. M.; Zeng, B. Q.; Li, Z. M. *Mater Lett* **2010,** *64* (20), 2226-2229.

24. Qu, B.; Li, J.-r.; Xiao, H.-n.; He, B.-h.; Qian, L.-y. *Polym Composite* **2015**, n/a-n/a.

25. Stauffer, D., *Introduction to percolation theory*. Taylor & Francis: London ;, 1985.

26. Avella, M.; Di Pace, E.; Immirzi, B.; Impallomeni, G.; Malinconico, M.; Santagata, G. *Carbohyd Polym* **2007,** *69* (3), 503-511.

27. Menard, K. P., *Dynamic Mechanical Analysis: A Practical Introduction*. Second ed.; CRC Press 2008; p 240.

28. Marais, C.; Villoutreix, G. *J Appl Polym Sci* **1998,** *69* (10), 1983-1991.

29. Faraz, M. I.; Besseling, N. A. M.; Korobko, A. V.; Picken, S. J. *Polym Composite* **2015,** *36* (2), 322-329.

30. Dean, G. D.; Broughton, W. *Polym Test* **2007,** *26* (8), 1068-1081.

31. (a) Leaderman, H. Elastic and creep properties of filamentous materials. Massachusetts Institute of Technology, 1941; (b) Tobolsky, A.; Eyring, H. *J Chem Phys* **1943,** *11* (3), 125-134.

32. Gearing, J. W. E.; Stone, M. R. *Polym Composite* **1984,** *5* (4), 312-318.

33. Vilcinskas, K.; Norder, B.; Goubitz, K.; Mulder, F. M.; Koper, G. J. M.; Picken, S. J. *Macromolecules* **2015,** *48* (22), 8323–8330.

34. (a) Picken, S. J.; Vanderzwaag, S.; Northolt, M. G. *Polymer* **1992,** *33* (14), 2998-3006; (b) Northolt, M. G.; van der Hout, R. *Polymer* **1985,** *26* (2), 310-316.

35. Suk, J. W.; Piner, R. D.; An, J.; Ruoff, R. S. *Acs Nano* **2010,** *4* (11), 6557-6564.

36. Gong, L.; Young, R. J.; Kinloch, I. A.; Riaz, I.; Jalil, R.; Novoselov, K. S. *Acs Nano* **2012,** *6* (3), 2086-2095.

37. Scherrer, P. *Göttinger Nachrichten Math. Phys.* **1918**, 98-100.

38. Haug, A.; Smidsrod, O. *Acta Chem Scand* **1970,** *24* (3), 843-&.

39. Vilcinskas, K.; Zlopasa, J.; Jansen, K. M. B.; Mulder, F. M.; Picken, S. J.; Koper, G. J. M. *Macromolecular Materials and Engineering* **2016,** *accepted*.

40. Paredes, J. G. A.; Spasojevic, M.; Faas, M. M.; de Vos, P. *Frontiers in Bioengineering and Biotechnology* **2014,** *2* (26), 1-15.

41. Kong, H. J.; Wong, E.; Mooney, D. J. *Macromolecules* **2003,** *36* (12), 4582-4588.

42. Sun, P. Z.; Zheng, F.; Zhu, M.; Song, Z. G.; Wang, K. L.; Zhong, M. L.; Wu, D. H.; Little, R. B.; Xu, Z. P.; Zhu, H. W. *Acs Nano* **2014,** *8* (1), 850-859.

43. Park, S.; Lee, K. S.; Bozoklu, G.; Cai, W.; Nguyen, S. T.; Ruoff', R. S. *Acs Nano* **2008,** *2* (3), 572-578.

44. Gao, X. F.; Jang, J.; Nagase, S. *J Phys Chem C* **2010,** *114* (2), 832-842.

CHAPTER 6

CONCLUSIONS AND RECOMMENDATIONS

FOR FUTURE WORK

6.1. Conclusions

In situ X-ray diffraction results of the structural evolution of graphite during its oxidation by the modified Hummers method indicates no development of the clear crystalline order of graphite oxide or sulfuric acid-graphite intercalation compound. In addition, our data suggests that depending on the activity of sulfuric acid, graphene-graphene interactions in graphite can be altered. At high acid activity, its molecules presumably diffuse in between graphene layers thus compromising the crystalline order of graphite as well as its oxidation reactions products-sulfuric acid-graphite intercalation compound and graphite oxide. As a result, concentrated sulfuric acid may be a suitable solvent to obtain graphene dispersions if complete exfoliation of graphene sheets is secured. Such graphene dispersions could be attractive for the preparation of high performance materials, for instance, aramid-graphene composite fibers.

(Reduced) graphene oxide-alginate biopolymer composite films show interesting properties that are strongly influenced by the composition. Different types of such composite films can be easily prepared from precursor Sodium alginate-graphene oxide (Na-Alg/GO) composites that can be obtained by a simple solution casting technique. Owing to the presence of the oxygenated groups both on polymer chains and GO sheets, an extensive and strong hydrogen-bonding network forms during evaporation of the solvent. During the drying process, the developing stress forces initially isotropically distributed GO sheets to align in Sodium alginate matrix. At a critical point, the system forms a rigid gel whereupon GO sheets remain permanently locked in the Sodium alginate matrix which causes the high degree of alignment of the filler sheets. The orientational order of GO sheets in the Sodium alginate-graphene oxide (Na-Alg/GO) composites can be accurately described by the Affine Deformation Model, which predicts a uniform microscopic deformation upon the exerted macroscopic force. The highest order parameter values can be obtained for the composites containing up to about 25 wt% of GO, beyond which it reduces due to the significant degree of stacking of GO sheets as well as the onset of gelation at higher solids concentration during the

drying process. Furthermore, the degree of alignment of filler sheets can be compromised by cross-linking Na-Alg/GO composites with Calcium or Barium ions. The different affinity of Calcium and Barium ions to the oxygenated groups of alginate chains and GO sheets compromises the orientational order of filler sheets in these divalent metal ion cross-linked alginate/rGO composites. Subsequent reduction of the water insoluble divalent metal ion cross-linked alginate/GO films in aqueous hydrazine solution, allows to obtain Calcium alginate/reduced graphene oxide (Ca-Alg/rGO) or Barium alginate/reduced graphene oxide (Ba-Alg/rGO) composites. The competing interactions between divalent metal ions, polymer chains and GO sheets during the ion exchange and GO reduction reactions significantly affect the orientational order of filler sheets in these composite films.

Varying the composition of graphene (oxide)-alginate biopolymer composites significantly influences other properties. Whereas the unfilled Sodium alginate, Calcium alginate, Na-Alg/GO and Ca-Alg/rGO composites show an amorphous structure, Barium alginate possesses a semi-crystalline structure that upon the presence of filler evolves into an incommensurately modulated semi-crystalline structure as observed for the Ba-Alg/rGO composites. The different binding sites of Calcium and Barium ions offer the explanation for the observed dissimilar microstructures of the unfilled divalent metal ion cross-linked alginates. Since Calcium ions preferentially bind to guluronic-guluronic acid and guluronic-mannuronic acid units in alginates, and Barium ions – solely to guluronic-guluronic acid and mannuronic-mannuronic acid blocks, the chains of divalent metal ion cross-linked alginates assume different conformations. The favored binding of Barium ions to the mannuronic-mannuronic acid blocks between the adjacent polymer chains presumably flattens out the alginate chains thereby allowing mannuronic acid blocks to assume a linear conformation and order parallel to each other, whereas the preferred binding of Calcium ions to mannuronic-guluronic units – apparently precludes packing of the polymer chains in an organized manner. With increasing rGO content, the amorphous structure in the Ca-Alg/rGO composites prevails, while in the Ba-Alg/rGO composites the formation of periodically modulated structures is observed.

A high degree of alignment of GO sheets inside the Sodium alginate matrix could spark an interest in packaging applications of the composite films. The water swelling resistance of Sodium alginate can be significantly improved by addition of GO. With augmenting weight fraction of GO, the formation of the extensive and robust hydrogen-bonding network between the oxygenated groups of Sodium alginate and GO provides few adsorption sites for water molecules, however at high water activities the network is disrupted due to the increased number of water molecules. The swelling resistance of the unfilled alginates can be further improved by cross-linking alginate with Calcium or Barium ions whereupon strong interactions of these ions with the oxygenated groups of the alginate inhibit water molecules from breaking them easily. In addition, the presence of hydrophobic rGO sheets further improves swelling resistance of divalent metal ion cross-linked alginate composites. Among the investigated alginate composite families, the Ba-Alg/rGO as well as unfilled Barium alginate demonstrates the lowest water sorption capacity that can be attributed to high affinity of Barium ions to the polymer as well as filler sheets. However, the introduction of the divalent metal ions apparently increases the free volume in the unfilled cross-linked alginates as manifested in the increased water sorption capacity at low water activity.

The distinctive sigmoidal shape of the moisture sorption curves of the unfilled alginates and their composites suggest the non-Fickian diffusion mechanism in these materials. The Variable Surface Concentration Model provides an accurate description of the experimental data and allows estimating water diffusion coefficients in the samples of various compositions. The mobility of water molecules in unfilled Sodium alginate and it 1 wt% GO composite at 20°C shows the dependence on water activity that originates from the disruption of the hydrogen-bonding network between the polymer chains, or polymer chains and GO, that in turn provides more room for the diffusing species. However, the formation of the relative immobile water clusters at high water activities is responsible for the decreased water mobility in these samples. On the other hand, with higher weight fractions of GO, water mobility in Na-Alg/GO composites monotonically decrease at all water activity values. The presence of highly ordered GO sheets inside the alginate matrix compels

diffusing water molecules to undertake longer pathways in order to traverse Na-Alg/GO films. The significant improvement of the water barrier films of Na-Alg/GO composites can be accurately predicted by the modified Nielsen's model, taking into account the orientational order of filler, and assuming the variable effective aspect ratio of GO sheets.

Water mobility at 20°C in the unfilled Calcium and Barium alginates, however, slightly increases at low water activities due to the increase in the free volume of the polymer upon cross-linking with the divalent metal ions. Nonetheless, due the relative immobility of the formed water clusters at higher water activities, the water diffusion values are reduced in the unfilled divalent metal ion cross-linked alginates. The presence of rGO sheets in the Ca-Alg/rGO composites reduces water mobility in the investigated water activity range below ≤ 15 wt% of rGO, whereas beyond this value it increases. On the other hand, the water mobility in the Ba-Alg/rGO composites increases at all investigated water activities below about 25 wt% of rGO. Such disparities arise due to different interactions of the divalent metal ions with the polymer chains and filler sheets. Where more polymer-Calcium ion-rGO and polymer-Calcium ion-polymer interactions are thought to exist in the Ca-Alg/rGO composites, in the Ba-Alg/rGO composites more isolated polymer-Barium ion-polymer and rGO-Barium-ion-rGO interactions are regarded.

Water mobility at 60°C for all the unfilled alginates and their composites suggest the onset of hydro-thermally induced structural changes inside the polymer matrix that result in a complex filler weight fraction and water activity dependence on the water transport in the composite films.

Investigation into the thermal properties of the pure alginates and their composites show that these materials are thermally stable. Due to the stronger interaction energy of the ionic bonds, the thermal stability of alginate can be further improved by cross-linking with Calcium or Barium ions. However, neither the presence of GO nor rGO in Sodium alginate or in the divalent metal ion cross-linked alginates improve the thermal stability of the composites.

On the other hand, electrical and mechanical properties of the alginate composites show strong composition dependence. Sodium alginate is a good insulator and its insulating properties can be further improved by cross-linking it with Calcium and Barium ions. In addition, the electrical resistivity of Sodium alginate can be increased by addition of electrically insulating GO sheets. In contrast, the presence of rGO sheets in the divalent metal ion cross-linked alginates improves electrical conductivity significantly. Nonetheless, contrary to other polymer-rGO composites, divalent metal ion cross-linked alginate/rGO show mediocre properties and high percolation threshold due to the specific divalent metal ion interactions with the filler sheets.

The complexity of such interactions manifests themselves in the difficult-to-predict stiffness and creep resistance of the cross-linked alginate composites. Whereas the stiffness of the divalent metal ion cross-linked alginate composites varies unsystematically with rGO content, the in-plane stiffness of the Na-Alg/GO composites increases with increasing weight fraction of GO and peaks at 25 wt% of GO owing to the strong interaction between filler and polymer as well as the orientational order of GO sheets. Indeed, a simple mechanical model that takes into account the stiffening effect of GO sheets parallel and perpendicular to the applied stress direction as well as the orientational order of filler sheets can adequately describe the improved stiffness in Na-Alg/GO composites. Furthermore, as manifested in the glass to rubber transition temperature, the polymer chain mobility in the Ca-Alg/rGO decreases with increasing rGO content, whereas in the Ba-Alg/rGO composites – it shows little variation. As such these results corroborate the specific interactions between the divalent metal ions, polymer chains and filler sheets.

The complex interactions between the constituents in the alginate composites also manifest themselves in the uncertain short-term creep behavior. The poor creep resistance up to about 6 wt% of GO in Na-Alg/GO composites can be explained by the ineffective hydrogen-bonding network between the oxygenated groups of polymer and GO sheets, and the stacking of filler sheets. Nevertheless, the formation of the robust hydrogen-bonding network at higher GO content in the

Sodium alginate matrix significantly improves stress distribution, and thus compensates for the stacking of GO sheets. On the other hand, the dynamic origin of the ionic bonds in the divalent metal ion cross-linked alginates and the specific ion interactions lead to difficult-to-predict creep behavior. Despite the complex stress relaxation mechanisms in the alginate composites, the stretched exponential Burgers' model accurately describes the creep compliance curves.

6.2. Recommendations for future work

There are a couple of aspects to consider in the future research of alginate-graphene composites.

First of all, it is important to note that the concentration of a divalent metal ion precursor solution strongly influences properties of unfilled alginates. Numerous studies [1] have shown that, for instance, immersion of Sodium alginate samples into a higher concentration Calcium salt precursor solution yields samples with the improved tensile strength, although some studies reported [1a, 1d] a decreased tensile strength of Calcium alginate prepared from higher Calcium precursor salt concentrations. In general, 1-5 wt% Calcium salt precursor solutions allows producing water-insoluble Calcium alginate samples with improved tensile strength and reduced water vapor permeation [1b-d]. However, longer than 15 minutes exposure time to the Calcium ion precursor solution usually has adverse effects on the properties of Calcium alginate [1a]. It is worth of pointing out that the direct mixing of Calcium salt precursor solution with Sodium alginate solution, and subsequent casting of the mixture yields inhomogeneous samples with poor mechanical and gas barrier properties [1b]. Besides the diffusion-based method employed in this work for the preparation of divalent metal ion cross-linked alginates, an alternative route may be considered. Cross-linked alginates can be obtained by the internal gelation method [2] whereupon the cross-linker ions in an inactive form (for instance in $CaCO_3$) are added to the alginate solution and the ion exchange is subsequently initiated by the change in pH of the mixture. The advantage of this method is that it yields more homogenous gels compared to the diffusion-based route. Overall, the abundance of

multivalent metal ions that readily cross-link with alginates and different cross-linking routes offer a great diversity of alginates with different properties that remain only just explored.

It is also equally important to consider weight fractions of plasticizers that are used to improve pliability of alginate films. Many authors [3] have investigated the influence of the variety of plasticizers, such as glycerol, sorbitol, fructose, on the mechanical and water vapor barrier properties of alginates. Whereas higher weight fractions of plasticizer reduce tensile strength, their effect on gas barrier properties is less predictable. For instance, higher contents of glycerol improve water vapor and oxygen permeability, while the variation in sorbitol concentration appears to little influence these properties [3d]. As the nature of a plasticizer and its weight fraction can greatly affect the final properties of the alginate, it is therefore important consider its role.

In the experimental procedure described in Chapter 3, Na-Alg/GO composites are used as the precursors of the divalent metal ion cross-linked alginates/rGO composites. Such preparation method does not enable to have full control over the interactions between the divalent metal ions, polymer and filler. Consequently, one may consider alternative alginate/(r)GO composite preparation routes. For instance, easy-to-prepare stable rGO oxide aqueous dispersions [4] can be utilized in preparation of Na-Alg/rGO composites that subsequently can be converted to divalent metal ion cross-linked alginate/rGO composites omitting the GO reduction step. Alternatively, one may also consider to conduct the ion exchange reaction in the presence of dissolved Sodium salt where the ion exchange equilibrium is altered [5]. Besides, chemical modification of the oxygenated groups on alginate chains and GO sheets offer sites for could lead to more targeted interactions between filler sheets and polymer chains. Properties and interactions between the constituents of such composites prepared via the alternative routes have not been reported in literature as yet.

Overall, the properties of graphene (oxide)-alginate biopolymer nanocomposites have only been scarcely explored. The versatility of alginates and magnificent properties of graphene and its derivatives offer numerous possibilities for the preparation of composites. Many factors influence

the properties of these composites: the composition of alginates, molecular weight distribution in the polymer, a preparation method, plasticizer, affinity of divalent metal ions both to the polymer chains and filler sheets. Nevertheless, deeper understanding of the interplay between such factors could yield composites suited to packaging and barrier coating applications. Upon further mastery of the synthesis methods, even high tech applications as membranes for separation and ion exchange might come within reach.

6.2. References

1. (a) Pavlath, A. E.; Gossett, C.; Camirand, W.; Robertson, G. H. *J Food Sci* **1999,** *64* (1), 61-63; (b) Rhim, J. W. *Lebensm-Wiss Technol* **2004,** *37* (3), 323-330; (c) Benavides, S.; Villalobos-Carvajal, R.; Reyes, J. E. *J Food Eng* **2012,** *110* (2), 232-239; (d) Guo, L. L.; Zheng, D.; Xu, J. C.; Gao, X.; Fu, X. T.; Zhang, Q. *Carbohyd Polym* **2016,** *136*, 259-265.

2. Smidsrød, O.; Draget, K. I., *Alginate Gelation Technologies*. Woodhead Publishing, Ltd.: 1997; p 428.

3. (a) Parris, N.; Coffin, D. R.; Joubran, R. F.; Pessen, H. *J Agr Food Chem* **1995,** *43* (6), 1432-1435; (b) Olivas, G. I.; Barbosa-Canovas, G. V. *Lwt-Food Sci Technol* **2008,** *41* (2), 359-366; (c) Santana, A. A.; Kieckbusch, T. G. *Braz J Chem Eng* **2013,** *30* (4), 835-845; (d) Jost, V.; Kobsik, K.; Schmid, M.; Noller, K. *Carbohyd Polym* **2014,** *110*, 309-319.

4. Li, D.; Muller, M. B.; Gilje, S.; Kaner, R. B.; Wallace, G. G. *Nat Nanotechnol* **2008,** *3* (2), 101-105.

5. Haug, A; Smidsrød, O. *Acta Chem Scand*. 1965, 19 (2), 341-351

SUMMARY

In this work, properties of Calcium alginate-reduced graphene oxide and Barium alginate-reduced graphene oxide composite films are explored. In addition, the properties of the divalent metal ion-cross-linked alginate composite films are compared to the analogous properties of uncross-linked Sodium alginate-graphene oxide composite films of the corresponding compositions. As the filler, used in the preparation of the composite films, is obtained by chemical oxidation of graphite, the prevailing knowledge of the process coupled with *in situ* X-ray diffraction investigation of the samples prepared by such a method is presented as well.

In Chapter 2 a summary of solvent-assisted exfoliation of graphite is given to introduce readers to the underlying stability mechanisms of graphene dispersions prepared via this method. In addition, a brief overview of chemical graphite oxidation methods, which utilize concentrated acids and strong oxidants, and of the current understanding of structural graphite evolution during this process are provided. The results of *in situ* X-ray diffraction investigation into the mechanism of graphite oxidation by Hummers' method are discussed, too. In contrast to *ex situ* X-ray diffraction studies of graphite oxidation reaction using the same method by other authors, our studies suggest that no well-define crystalline order of intermediate and final products of this reaction develops. Furthermore, our findings suggest that depending on sulfuric acid activity, its molecules can presumably intercalate in between graphene sheets of graphite and significantly reduce crystalline order in it. Consequently, sulfuric acid may be a good solvent for graphene dispersions, provided there is sufficient energy input into graphite to separate the graphene layers.

In Chapter 3 the various kinds of order, either highly aligned or compromised order, of (reduced) graphene oxide sheets inside an alginate matrix is studied by environmental scanning electron microscopy and 2-Dimensional X-ray Diffraction. An amorphous structure of Sodium alginate and its graphene oxide composites as well as of Calcium alginate and its reduced graphene oxide composites are observed by X-ray diffraction measurements in the Bragg-Brentano reflection

configuration. On the other hand, a semicrystalline structure and formation of a modulated crystalline structure in Barium alginate and Barium alginate-reduced graphene oxide composites, respectively, are revealed. The azimuthal angle intensity profiles obtained from 2-dimensional X-ray diffraction analysis are fit with Maier-Saupe and affine deformation model predictions, and the latter proves to be the most reliable to quantify the order parameter $<P_2>$ values of filler sheets. A maximum $<P_2>$ value of 0.8 at 25 wt% of graphene oxide inside the Sodium alginate matrix is found whereas the maximum $<P_2>$ value of reduced graphene oxide sheets in Calcium alginate matrix is lower. The orientation of reduced graphene oxide sheets in Barium alginate is not observed. The formation of a highly aligned Sodium alginate-graphene oxide composite structure is described by the Affine Deformation Model, whereupon drying the developed yield stress causes sheets to align in-plane with the polymer matrix. The impaired orientation of reduced graphene oxide sheets inside the Calcium alginate matrix and absence of orientation in the Barium alginate matrix is explained by the structure development in the polymer matrix itself due to metal-ion induced cross-linking.

Water sorption and diffusion in (reduced) graphene oxide-alginate composites of various compositions are discussed in Chapter 4. Water sorption capacity of Sodium alginate can be significantly reduced by the inclusion of graphene oxide sheets due to the formation of an extensive hydrogen-bonding network between oxygenated groups. Cross-linking alginate with Calcium or Barium ions and presence of reduced graphene oxide can further improve the swelling resistance due to the strong interactions between metal ions, alginate and filler sheets. Water sorption kinetics in all alginate composites indicate a non-Fickian diffusion process that can be accurately described by the Variable Surface Concentration model. Depending on the composition and temperature, water mobility in the composite films can decrease or improve, but overall the water barrier properties of alginate composites improve upon addition of (reduced) graphene oxide. Lastly, water barrier properties of Sodium alginate-graphene oxide composites can be adequately predicted by a simple model taking into account the orientational order of filler sheets and their effective aspect ratio.

In Chapter 5, the thermal, electrical and mechanical properties of (reduced) graphene oxide-alginate biopolymer films are discussed. The thermal stability of Sodium alginate-graphene oxide composites is little influenced by the weight fraction of filler. On the other hand, it is improved by the introduction of cross-linking through divalent metal cations, albeit the amount of reduced graphene oxide little affects it in Calcium or Barium ions cross-linked alginate-reduced graphene oxide composites. The electrical conductivity of the divalent metal alginate-reduced graphene oxide composites improves approximately 10 orders of magnitude with increasing weight fraction of filler, however the interactions between divalent metal ions, polymer and filler sheets prevent the formation of an effective network of electrically conductive reduced graphene oxide sheets. Addition of insulating graphene oxide reduces electrical conductivity of Sodium alginate-graphene oxide composites further. Storage moduli, glass to rubber transition temperatures, and creep tests show strong composition dependence in the composite films as a consequence of dissimilar and complex interactions of the ions with both polymer and filler as well as the complex nature of multiple stress relaxation mechanisms. Nonetheless, the stretched exponential Burgers' model accurately describes short time creep compliance of the (reduced) graphene oxide-alginate biopolymer composite films. In addition, a simple mechanical model, which takes into account the orientational order of filler sheets, allows for the accurate prediction of reinforcement by graphene oxide sheets in Sodium alginate-graphene oxide composites.

SAMENVATTING

In dit proefschrift worden de eigenschappen van composietfilms van calciumalginaat met gereduceerd grafeenoxide en van bariumalginaat met gereduceerd grafeenoxide onderzocht. Bovendien worden de eigenschappen van alginaatcomposietfilms die zijn verknoopt met divalente metaalionen vergeleken met de analoge eigenschappen van niet-verknoopte natriumalginaat-grafeenoxide compositietfilms. Daar het vulmiddel, zoals het gebruikt wordt voor de bereiding van de composietfilms, wordt verkregen door chemische oxidatie van grafeen, wordt de bestaande kennis met betrekking tot het proces samen met *in situ* Röntgendiffractie-onderzoek van de monsters, die bereid zijn met die methode, ook gepresenteerd.

In hoofdstuk 2 wordt een samenvatting gegeven van door oplosmiddel-ondersteunde afschilfering van grafiet teneinde de lezers in te leiden tot het onderliggende stabilisatiemechanisme van grafeendispersies die zijn bereid met deze methode. Bovendien wordt een kort overzicht gegeven van de chemische oxidatiemethoden, die gebruik maken van geconcentreerde zuren en sterke oxidatoren, en van het huidige begrip omtrent de structurele evolutie van grafiet tijdens dit proces. De resultaten van *in situ* Röntgendiffractie-onderzoek naar het mechanisme van grafietoxidatie via Hummers' methode worden ook bediscussieerd. In tegenstelling tot *ex situ* Röntgendiffractie-onderzoek door andere auteurs naar grafietoxidatie volgens dezelfde methode laat onze studie zien dat er zich geen goed-gedefinieerde kristallijne ordening in tussen- en eindproducten van de reactie ontwikkelen. Verder suggereren onze bevindingen dat afhankelijk van de zwavelzuuractiviteit haar moleculen kunnen intercaleren tussen de grafeenvlakken van grafiet en daarmee de kristallijne orde in sterke mate tenietdoen. Als gevolg daarvan zou zwavelzuur een goed oplosmiddel voor grafeendispersies kunnen zijn, vooropgesteld dat voldoende energie wordt toegevoegd aan grafiet om de grafeenlagen te scheiden.

In hoofdstuk 3 worden de verschillende vormen van ordening, enerzijds volledig uitgelijnd en anderzijds gecompromitteerd, van de (gereduceerde) grafeenoxide plaatjes bestudeerd met behulp

van ‘environmental scanning’ elektronenmicroscopie en 2-dimensionale Röntgendiffractie. Een amorfe structuur van natriumalginaat en zijn grafeenoxide-composieten zowel als van calciumalginaat en zijn gereduceerde grafeenoxide-composieten werd waargenomen met Röntgendiffractie in de Bragg-Brentano reflectie-configuratie. Aan de andere kant werd een semi-kristallijne structuur en de formatie van een gemoduleerde kristalstructuur ontwaard in respectievelijk bariumalginaat en bariumalginaat composieten met gereduceerd grafeenoxide. De azimut-afhankelijke intensiteitsprofielen verkregen door analyse met 2-dimensionale Röntgendiffractie konden worden voorspeld door het Maier-Saupe model en door het affiene deformatiemodel waarbij de laatste de meest betrouwbare bleek om de <P2>-ordeparameterwaarden voor de vulmiddel plaatjes te verkrijgen. De grootste <P2>-waarde van 0.8 werd gevonden voor 25 gewichtsprocent grafeenoxide in een natriumalginaat-matrix terwijl de maximum waarde voor gereduceerde grafeenoxide plaatjes in calciumalginaat lager is. Ordening van gereduceerde grafeenoxide plaatjes in bariumalginaat is niet waargenomen. De vorming van een sterk gerichte natriumalginaat/grafeenoxide composietstructuur wordt beschreven door het affiene deformatiemodel, waarbij de met door droging ontwikkelde spanning de plaatjes richt in het vlak van de polymeermatrix. De verminderde oriëntatie van gereduceerde grafeenoxide plaatjes in de calciumalginaat-matrix en de afwezigheid van oriëntatie in de bariumalginaat-matrix wordt verklaard door de ontwikkeling van een structuur in de polymeermatrix zelf ten gevolge van de door metaalionen veroorzaakte verknoping.

Wateropname en diffusie in (gereduceerde) grafeenoxide/alginaat composieten van allerlei samenstelling worden besproken in hoofdstuk 4. De wateropname-capaciteit van natriumalginaat kan significant worden gereduceerd door de toevoeging van grafeenoxide plaatjes door de vorming van een uitgebreid waterstofbandnetwerk tussen de zuurstofrijke groepen. Verknoping van alginaat met calcium- of bariumionen en de aanwezigheid van gereduceerd grafeenoxide kan de weerstand tegen zwelling verder verbeteren ten gevolge van de sterke interacties tussen metaalionen, alginaat en vulmiddelplaatjes.

De kinetiek van wateropname in alle alginaat-composieten laat een niet-Fick's diffusieproces zien dat nauwkeurig kan worden beschreven door het variabele oppervlakteconcentratiemodel. Afhankelijk van de samenstelling en de temperatuur kan de watermobiliteit af- of toenemen maar de globale water barrière eigenschappen van alginaat-composieten verbeteren door de toevoeging van (gereduceerd) grafeenoxide. Tenslotte kunnen de water barrière eigenschappen van natriumalginaat/grafeenoxide composieten adequaat beschreven worden met een eenvoudig model dat rekening houdt met de mate van oriëntatie van de vullerplaatjes en hun effectieve aspect ratio.

In hoofdstuk 5 worden de thermische, elektrische en mechanische eigenschappen van (gereduceerd) grafeenoxide/alginaat biopolymeerfilms besproken. De thermische stabiliteit van natriumalginaat/grafeenoxide composieten wordt weinig beïnvloedt door de gewichtsfractie vulmiddel. Aan de andere kant wordt die verbeterd door verknoping met divalente metaalionen hoewel de hoeveelheid gereduceerd grafeenoxide weinig effect heeft voor de door calcium- of bariumionen verknoopte alginaat/gereduceerde grafeenoxide composieten. De elektrische geleiding van de divalente metaalalginaat/gereduceerde grafeenoxide composieten verbeterd met ongeveer 10 ordes van grootte met toenemende gewichtsfractie vulmiddel ondanks dat de interacties tussen divalente metaalionen, polymeer en vulmiddelplaatjes de vorming van een effectief netwerk van elektrisch geleidende gereduceerd grafeenoxide plaatjes verhindert. Toevoeging van isolerend grafeenoxide reduceert de elektrische geleidbaarheid van natriumalginaat/grafeenoxide composieten verder.

Opslagmodulus, glas naar rubber overgangstemperatuur en kruipstudies laten een sterke afhankelijkheid van de samenstelling van de films zien als gevolg van de ongelijkwaardige en complexe interacties van de ionen met het polymeer en het vulmiddel zowel als de complexe aard van de vele spanningsrelaxatiemechanismen. Niettemin beschrijft een Burgers model met gerekt exponentiele relaxatie de korte-tijd kruip-compliantie van de (gereduceerde) grafeenoxide/alginaat biopolymeercomposiet films. Bovendien kan een eenvoudig mechanisch model, dat de oriëntatie

van de vullerplaatjes in rekening neemt, de versterking door grafeenoxide in natriumalginaat/grafeenoxide composieten nauwkeurig beschrijven.

ACKNOWLEDGEMENTS

Research described in this dissertation could not have been carried out without help of many people.

First and foremost, I owe a debt of gratitude to my supervisors – Ger, Fokko and Stephen – for offering me the opportunity to pursue a doctorate degree under their guidance, help and advice during the course of the studies, and for their wholehearted support all this time. I could have not asked for better supervision and more successful collaboration, we have really and truly been a good team. I sincerely thank Prof. dr. J.H. van Esch for giving me the opportunity to join the Advanced Soft Matter group, and providing feedback that helped to improve research. I particularly thank Prof.dr. ir. K.M.B.Jansen for his active interest in my PhD project and significant contribution to this work. I also acknowledge Dr.hab. E.Mendes and Prof.dr. F.Kapteijn for their keen interest in this research, and valuable suggestions for improving it. I am grateful too to the committee members for accepting the invitation and their effort to review this work.

I must also thank Ben, Marcel, Kees, Arjan, Piet, Lars and Duco for the assistance with measurements and helpful suggestions for improving the outcome of them. I also acknowledge Marcel, Ben, Lars, Louw, Mieke and Wil for helping to organize work in the lab and office.

I am grateful to all the ex- and current members of the Advanced Soft Matter group as well as people from other sections in Chemical Engineering Department who have created pleasant ambience inside and outside of work, each of you has been an excellent colleague and aid. I also express my appreciation to a number of people I have been blessed to meet outside the university. To unnamed others who I have encounter along the way, my gratitude is equal.

Above all, I thank my family for their infinite love, overwhelming support as well as bearing with my physical absence and mental abstraction during this time.

ABOUT THE AUTHOR

Karolis Vilcinskas was born on 2nd of April 1986 in Siauliai (Lithuania). He received a bachelor degree in Chemical Engineering from Kaunas University of Technology (Lithuania) in 2009. He then continued graduate studies at the same university and attained a master degree in Chemical Engineering in 2011. In March 2012, after a short stint in industry, he undertook doctoral studies at Delft University of Technology (The Netherlands) under the supervision of Prof.dr. S.J.Picken, Prof.dr. F.M.Mulder and Dr.ing. G.J.M.Koper. In his PhD project, Karolis has investigated properties of alginate bionanocomposite films. He has presented his work at a few national and international conferences, and published the results of his research in a couple of peer-review scientific journals.

List of publications:

- Koper, G. J. M., Vilcinskas, K. Anomalous Thickness Dependence of Nanocomposite Layer-By-Layer Membranes. *Colloid Surface A* 2014; 442, 2-5.
- Vilcinskas, K., Norder, B., Goubitz, K., Mulder, F.M., Koper, G.J.M., Picken, S.J.Tunable Order in Alginate/Graphene Biopolymer Nanocomposites. *Macromolecules*, 2015; 48(22): p. 8323-8330.
- Vilcinskas, K., Zlopasa, J., Jansen, K. M. B., Mulder, F. M., Picken, S. J., Koper, G. J. M. Water sorption and diffusion in graphene (oxide)-alginate biopolymer nanocomposites. *Macromolecular Materials and Engineering*, 2016; 301: p.1049−1063.
- Vilcinskas, K., Jansen, K. M. B., Mulder, F. M., Picken, S. J., Koper, G. J. M. Composition dependent properties of graphene (oxide)-alginate biopolymer nanocomposites. Submitted to *Polymer Composites*, 2016.
- Vilcinskas, K., Mulder, F. M., Picken, S. J., Koper, G. J. M. In situ X-ray diffraction of the graphite oxidation reaction indicating different exfoliation mechanism than ex situ studies. Submitted to *Nanoscale*, 2016.